Wayne State University

Wayne State University Dissertations

January 2019

Development Of A Novel Ultrasound/photoacoustic Tomography System For Breast Cancer Imaging Using Full-Ring Illumination Mode

Suhail Salem Alshahrani
Wayne State University

Follow this and additional works at: https://digitalcommons.wayne.edu/oa_dissertations

Part of the Biomedical Engineering and Bioengineering Commons

Recommended Citation

Alshahrani, Suhail Salem, "Development Of A Novel Ultrasound/photoacoustic Tomography System For Breast Cancer Imaging Using Full-Ring Illumination Mode" (2019). *Wayne State University Dissertations*. 2316.
https://digitalcommons.wayne.edu/oa_dissertations/2316

This Open Access Dissertation is brought to you for free and open access by DigitalCommons@WayneState. It has been accepted for inclusion in Wayne State University Dissertations by an authorized administrator of DigitalCommons@WayneState.

DEVELOPMENT OF A NOVEL ULTRASOUND/PHOTOACOUSTIC TOMOGRAPHY SYSTEM FOR BREAST CANCER IMAGING USING FULL-RING ILLUMINATION MODE

by

SUHAIL SALEM ALSHAHRANI

DISSERTATION

Submitted to the Graduate School

of Wayne State University

Detroit, Michigan

in partial fulfillment of the requirements

for the degree of

DOCTOR OF PHILOSOPHY

2019

MAJOR: BIOMEDICAL ENGINEERING

Approved By:

Advisor Date

© COPYRIGHT BY

SUHAIL SALEM ALSHAHRANI

2019

All Rights Reserved

DEDICATION

I dedicate this work to my father, Salem Alshahrani, my mother Shikah Alshahrani, and to all my family who have supported and encouraged me my whole life. I also dedicate my work to my wife, Wejdan Alshahrani who has been my strongest supporter during my PhD journey. In addition, I dedicate this work to my brother Dr. Naif Alshahrani who always supported me during hard times. Finally, I dedicate my work to my lovely son Naif who has filled my life with love and happiness.

ACKNOWLEDGMENTS

I would like to express my sincere gratitude to my advisor Professor Mohammad Mehrmohammadi, for the continuous support of my PhD study and related research, and for his motivation, and knowledge. His guidance helped me all the time in the research and writing of this thesis. I am thankful and proud to be one of his PhD students and to know him as a person.

Besides my advisor, I would also like to thank Professor Neb Duric for his guidance and assistance in addition to allowing me access to his laboratory and equipment. Also, I would like to thank the other members of my thesis committee: Professor Ivan Avrutsky, Professor Juri Gelovani, and Professor Zhifeng Kou, for their insightful comments, advice, and encouragement.

Besides my committee, I would like to thank Dr. Eugene Malyarenko and Dr. Di Chen for taking the time to explain the inner workings of different laboratory equipment to me.

Many thanks to all my colleagues in the lab, especially Dr. Naser Alijabbari, Yan Yan, Alexander Pattyn, Maryam Basij, and John Samuel for a great time, cooperation, motivation, and support.

My sincere thanks also go to King Saud University (Riyadh, Saudi Arabia) for financial support and supervision during my academic journey in the USA.

Finally, many thanks go to my family and friends who called to support and motivate me during my studies.

Thank you all !

TABLE OF CONTENTS

LIST OF TABLES

LIST OF FIGURES

CHAPTER 1 - INTRODUCTION

1.1 Breast Cancer

Breast cancer is the most common type of cancer and accounts for 30% of all new cancer cases in women in the United States (U.S.) [1]. According to the World Health Organization (WHO), breast cancer in women has an estimated annual incidence of 2.1 million and is responsible for about 15% of all cancer deaths in women around the world [2]. In 2019, the expected incidence of invasive breast cancer among U.S. women is 268,600 [1]. For instance, it is estimated that 41,760 women will die from breast cancer, with mortality rates being higher in advanced ages [1, 3]. Women with highly dense breast tissue are more likely to be diagnosed with breast cancer than women with low-density breast tissue [4, 5]. However, the mortality rate has rapidly declined since 1989 due to developments in the medical field, and specifically medical imaging [6, 7].

Each female breast tissue is lying on the pectoral muscle of the chest. The female breast extends over a large area from below the clavicle to the axilla, better known as the armpit, and eventually across to the sternum. In the female breast, there are two types of tissue; fatty and glandular **(Figure 1)**. In addition, there are blood vessels as well as sensory nerves in the breast and skin areas. The primary function of the glandular tissue (mammary glands) is milk production. The milk travels to the nipple by lactiferous ducts which connect glandular tissue and the nipple. The alveoli link to the lactiferous tubules, which then join the lactiferous duct, a channel lined with epithelial cells. The suspensory ligaments (Cooper’s ligaments) preserve the breast shape and help to hold it to the chest. The fatty and connective tissues that surround the lobules and ducts help in protecting them while shaping the breast [8, 9].

The breast is also served by the lymphatic system, with the main drainage being to the axilla. The breast’s lymphatic system originates at the duct walls with the fibrous tissue that connects the lobes. The lymphatic channels in the subareolar plexus then drain primarily into the axillary lymph nodes, a core reason why metastasis of breast cancer first happens in the axillary. The lymphatic system in the breast is one of the features used for the staging of breast cancer since the absence of cancer in the sentinel lymph nodes following histopathology indicates that cancer cells have not spread to the axillary lymph nodes [10].

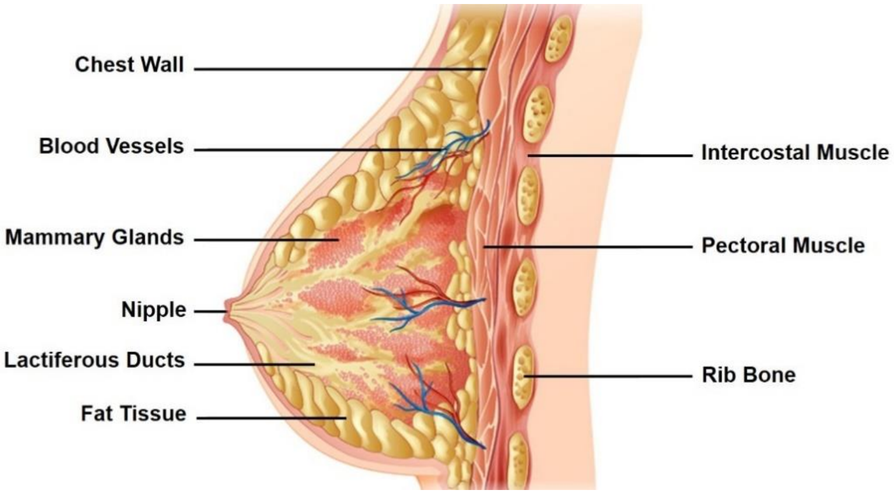

Figure 1: Graph shows the main parts of the female breast. [1]

Cancer is the abnormal growth (uncontrolled) of cells to form a tumor which can occur in any organ or tissue of the human body. Further, this tumor can either be benign or malignant. A benign tumor is not cancer, hence, harmless to a person's health and can be safely removed. Benign breast tumors are a heterogeneous group of a non-malignant condition occurring in the fatty, supportive parenchymal, and the epithelial components of the breast [11]. The benign conditions account for a significant proportion of referrals for breast cancer screening. The benign

---

[1] The graph was modified from https://breast360.org/topics/2017/01/01/breast-anatomy/

breast lumps are mainly fibroadenomas that usually occur in the form of a single, ovoid, discrete, and mobile lump in women aged below 25 years. In other cases, these lumps may occur in multiple and tender forms. For small lumps (<1 cm in diameter) conservative management, without excision, is recommended since most remain static; however, larger fibroadenomas (>2 cm in diameter) which show signs of continued enlargement may require excision. Such enlarging fibroadenomas may lead to phyllode tumors, which are more advanced lumps, at times reaching 5 cm in diameter, and could lead to malignancy. Absence of malignancy in most of these benign tumors implies that staging using lymph nodes is not applicable, and treatment usually involves excision [11, 12]. Malignant tumors, on the other hand, are cancer that is capable of destroying the tissue around it or even breaking away to other parts of the body to form new tumors. Malignant tumors require careful management with a combination of chemotherapy, radiotherapy, surgery, and targeted therapy, depending on the present biomarkers [13].

1.2 Types of Breast Cancer

Breast cancer is a complex disease, and as such, consists of several types. A woman can be affected by more than one type at any given time, and it should be noted that most breast cancers are the adenocarcinoma type of carcinomas. Carcinoma means cancer had its initialization in the epithelial cells – the cells that form the lining of tissues and organs, while adenocarcinoma means cancer started in the glandular tissue. In this regard, ductal and lobular carcinomas are the major types of breast cancer. Similarly, the two can be noninvasive or invasive [14].

1.2.1 Ductal carcinoma

According to the name, this type of cancer has its start within the cell lining the breast's ducts, specifically beneath the nipple and areola [14]. Usually, the ducts are responsible for the supply of milk to the nipple. Overall, this cancer accounts for 85-90% of breast cancers [15]. Ductal carcinoma is divided into:

- ***Ductal carcinoma in situ (DCIS):*** Also seen as the precancer condition, this is ductal carcinoma that is noninvasive. In this case, the abnormal cells are well contained within the milk ducts. Ultimately this makes it treatable through a lumpectomy [14, 16].
- ***Invasive ductal carcinoma (IDC):*** This is ductal carcinoma capable of spreading outside the milk duct to other tissues. Consequently, mastectomy is required for treatment. In addition, the occurrence of IDC may result in dimpling of the skin as well as retraction of the nipple. It is the most occurring invasive breast cancer accounting for most lumps that are felt [14, 16].

1.2.2 Lobular carcinoma

As per the name, lobular carcinoma starts in the lobes or glands that produce milk inside the breast. The lobes are found deep in the breast and are under the ducts. Further, lobular carcinoma accounts for 8% of all breast cancers [17]. The lobular carcinoma is divided into:

- ***Lobular carcinoma in situ (LCIS):*** Similarly, this is seen as a pre-cancer condition. It is the noninvasive version of lobular carcinoma, and the cells remain within the lobes. As opposed to DCIS, it is rarely observed in a mammogram, and its discovery is normally made while checking for other lumps in the breast. The removal of the tumor can be done through a lumpectomy [18].
- ***Invasive lobular cancer (ILC):*** This occurs in a case where lobular cancer has spread out of the lobes. Consequently, this requires a mastectomy. Overall it accounts for a small percentage of invasive cancers and is only discovered once another breast tissue has been removed [19].

1.3 Imaging Modalities for Screening and Diagnosis of Breast Cancer

Medical imaging is one of the reliable and helpful diagnostic techniques that has been used to diagnose patients. For breast cancer, breast mammogram, B-mode ultrasound (US), and magnetic resonance imaging (MRI) play leading roles in the detection, staging, and diagnosis of this disease [20, 21]. Other technologies, such as positron emission tomography (PET) and single-photon emission computed tomography (SPECT), have also been used in detecting breast cancer [22, 23].

X-ray mammograms offer clinicians the ability to scan and highlight the breast from multiple points [24]. Mammography is a breast X-ray examination that can visualize very small, non-palpable tumors. Changes in the breast can be detected before they are intense as a knot or hardening [25]. Due to the physical nature of the x-ray, the healthy tissues such as the fatty tissue that have a lower density, have a color similar to the background of the created image. Meanwhile, tumors appear brighter “whiter” on the picture. The ability of mammography to detect breast cancers differs across the female population according to several factors. The most important of these is the fact that the sensitivity of mammography is lower in women with dense breasts who are considered at a higher risk of developing breast cancer [4, 5, 20, 26]. Women are classified based on the breast density to four categories which are; almost entirely fat, scattered fibroglandular, heterogeneously dense, and extremely dense [27]. Mammogram sensitivity decreased at heterogeneously dense and extremely dense categories, which represent 43.3 % of United States women aged between 40 to 74 years old [28]. For this reason, imaging methods supplementation to screen and evaluation of dense breasts have been investigated and mainly include ultrasonography and MRI [29, 30]. Breast MRI has a higher sensitivity than the mammogram for dense breast tissue [31, 32]. Due to the often different hydrogen content, a differentiation between altered and healthy tissue is possible [33]. For further distinction of whether a malignant change is present, a contrast medium is present, which represents the different blood flow in the tissues [33]. However, MRI is an expensive modality, so the cost and availability of MRI are issues with this reliable modality. In addition, it is not possible to perform MRI to a patient with implanted object such as pacemaker and some metals.

Conventional B-mode ultrasound is one of the most widely used medical imaging technique for screening various types of human tissues, such as those in the breast [34, 35]. With the help of high-frequency sound waves, a clear image of dense areas can be formed, which is known as a sonogram [36, 37]. The sound waves which are used pass through the patient's breast and bounce back after interacting with various tissues of the body. These waves help to create a 2-D image of internal structure on the real-time monitor [20, 38]. Different techniques are used to filter the original signal and reduce the artifacts so that only the higher frequencies produce the image. As a result, the contrast between glandular tissue, adipose tissue, and lesions improves in addition to resolution [39]. Linear array ultrasound can emphasize the location of a cyst or mass as well as distinguish between a solid mass and fluid-filled cyst [38, 40]. Unfortunately, although the conventional B-mode US is a high-sensitivity imaging tool, risk-free (non-ionizing), low-cost, and can produce images in real-time, it provides low specificity, which leads to unnecessary biopsies [41, 42].

With the risk presented by the rise in new breast cancer cases and the demonstrated limitations of existing screening equipment, the need for more effective breast cancer screening tools and technology is a high priority. For example, various types of ultrasound elastography modalities have been developed and implemented in clinical settings. These serve as a complement to B-mode US, enhancing its specificity [40, 43, 44]. On the other hand, promising results for breast cancer screening have been demonstrated using ultrasound tomography (UST) equipped with a ring US transducer, which provides high-quality, multi-parametric images of breast lesions [45-47]. The positive predictive value of UST has proven to be comparable to MRI [48]. The reliability of diagnosis of breast tissue, when using UST equipped with a ring US transducer, offers the capability of providing enhanced breast tissue data for composition and density [45, 46, 48-50]. In addition to providing tomographic pulse-echo US images, UST is also capable of measuring relevant diagnostic data such as acoustic attenuation (AA) and speed of sound (SOS) [51, 52]. In particular, AA and SOS data can be used to characterize stiffness which considered as a marker to differentiate between benign and malignant [53].

1.4 Photoacoustic (PA) for Breast Cancer Imaging and Staging

Among various imaging technologies, photoacoustic (PA) imaging is a novel imaging technology that has been demonstrated to be useful for a variety of medical and biological diagnostic applications, including those for the detection and diagnosis of cancer. In this imaging modality, laser pulses (which are non-ionized) are allowed to pass through biological molecules for imaging [54]. The light energy is converted into heat after absorption by the targeted tissue, causes rapid thermoelastic expansion of the tissue, and this leads to acoustic emission (**Figure 2**). PA imaging shows notable promise as a diagnostic tool in the early detection of cancer cells because it can distinguish a tumor from the healthy tissue through optical absorption [55, 56]. In fact, because of its ability to classify, compare and precisely describe breast cancer characteristics, PA imaging has recently been the subject of interest in studies that explored potential applications within various settings [57, 58]. The great advantage of PA imaging is its suitability as a diagnostic modality for clinical applications because of the ability to produce real-time molecular and functional information with high-resolution at relevant depths [59, 60]. Another positive factor is the capability of PA to be combined with US imaging for a wide variety of medical and clinical applications because both imaging modalities possess shared hardware components and a common signal detection equipment [61-64].

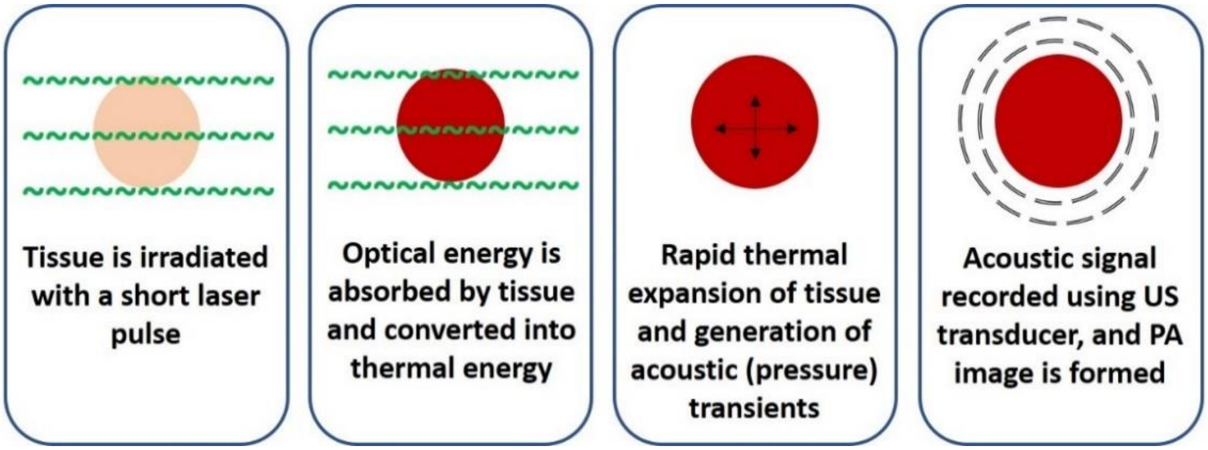

Figure 2: Photoacoustic imaging principle starting from tissue irradiation (left) and ending with the generation of acoustical signal (right).

PA imaging has applications in many medical and biological areas, such as an assessment of dermatological conditions, skin, breast, and colon cancer [65, 66]. Each molecule inside the human body has a specific absorption coefficient that can be used in PA imaging by changing the applied wavelength of the laser source (**Figure 3**) [67]. The endogenous contrast agents have higher absorption coefficients than elements in the surrounding tissues and are observed when a particular wavelength is applied [56]. Biological tissues in the body contain many endogenous contrast agents that can be used in PA imaging [56, 68]. Melanin, hemoglobin, water, and lipids are reported as sources of endogenous contrast in PA imaging [54, 56, 68-70]. The use of endogenous contrast agent in PA imaging has two advantages. First, though exogenous contrast agents provide the ability to target specific molecules, endogenous contrast agents are biologically unlike the former. The other advantage offered by endogenous contrast agents is that these agents produce physiological changes, like tissue vascularity (density of vasculature per volume of tissue), and oxygen saturation [56, 71, 72]. Lipids, also, is a known marker of breast cancer and could be detected by PA imaging after applying appropriate wavelength [73]. Besides, angiogenesis and hypoxia are common markers in breast cancer and can be monitored by PA imaging focused on hemoglobion and oxygen saturation (SO_2) [72, 74]. A tumor will be developed if it is continuously supplied with rich nutrients and oxygen. New vascularization is required for the development and progression of the tumor. Alternatively, tumor cells overgrow and the demand of the oxygen exceeds the normal oxygen supply for health tissue creating an area where the oxygen concentration of the carcinogenic tissue is significantly lower than the surrounded healthy tissue [74]. To measure the hypoxia by using PA imaging, the ratio of the deoxyhemoglobin to total hemoglobin is calculated by:

$$SO2 = \frac{[dHb]}{[HbO2] + [dHb]} \tag{1.1}$$

where the dHb refers to deoxyhemoglobin measured at 750 nm wavelength (high absorption coefficient for dHb), while HbO_2 refers to the oxyhemoglobin measured at 850 nm wavelength(high absorption of the HbO_2) [73, 75].

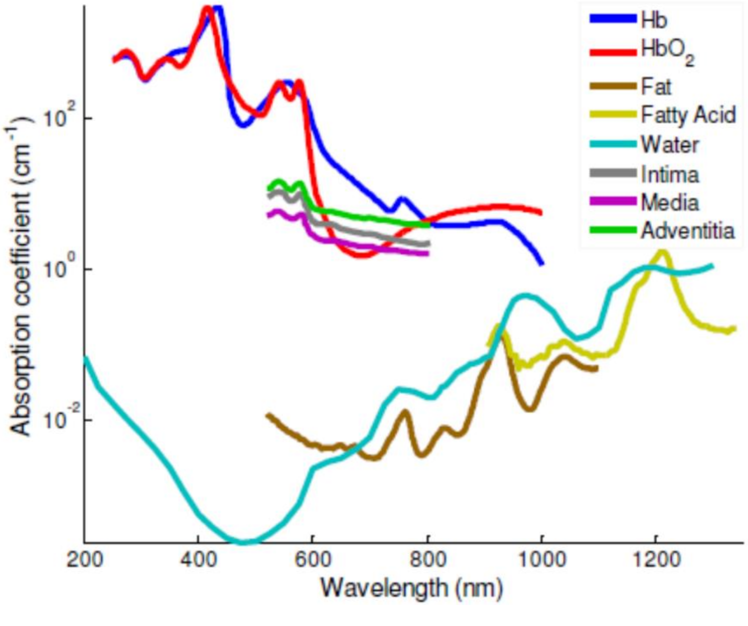

Figure 3: Graph of optical absorption spectra for different tissues inside the human body. Graph adapted from [67]

In conclusion, PA imaging is a beneficial imaging modality that could be combined with US modality to perform breast imaging. The tumor's malignancy and its stage can be detected and characterized based on oxygen saturation, microvascular density, and structures [76] by using the PA imaging. For this reason, the addition of the PA to the US will provide valuable functional and molecular information which will improve the diagnostic capability of breast tissue for physicians [77, 78].

1.5 Breast Photoacoustic Tomography (PAT) – An Overview

The photoacoustic tomography (PAT) is a medical imaging technology which is used to investigate the essential aspect of the high optical scattering [69, 79]. The PAT applications are the fundamentals as they are meant for the future implication of the medical screening [80]. In addition, PAT offers to measure in situ and to analyze processes in a time-resolved manner [60]. For clinical practices, the accuracy in the assessment of metastasis is critical, and there exists a deficiency of medical imaging methods in this regard. Real-time and non-invasive imaging of significant physiological and anatomical changes can be brought by the PAT imaging which indicates the progress of cancer invasion along with metastasis [81]. The applicability of PAT in the area of breast cancer detection is the following. Firstly, it investigates the molecular levels of the disease that promotes the idea of substantive usage of medical technology [82]. Secondly, its complementary diagnostics advance the exploration of the core cells that eliminate the health of the individual. The use of US/PA tomographic system instead of handheld US/PA system has many advantages. Firstly, the tomographic screening is an independent operator modality, which will minimize possible shortage that could occur from the operator [46]. Secondly, the tomographic method is a 3-D volumetric imaging modality that can cover whole breast tissue, which will increase the accuracy of the screening [46].

Four different breast PAT systems, with a reported human application, are reviewed. The breast PAT systems are:

1. Twente Photoacoustic Mammoscope (Twente PAM)
2. Laser Optoacoustic Imaging System (LOIS-64)

3. 512-detector OptoSonics photoacoustic mammography system
4. Single-breath-hold photoacoustic computed tomography (SBH-PACT) system

The specification of the four PAT systems is provided in the following, while **Table 1** provides a summary of the specification and observed limitations.

1.5.1 Twente Photoacoustic Mammoscope (Twente PAM)

In this system, a patient would lie in the prone position, and one breast would be gently compressed into the mammographic geometry. The Twente PAM uses implements NIR pulsed laser light that is 1064 nm wavelength, producing between 5 and 10 nanosecond pulses based at 10 Hz with a laser output of 60 mJ. The illumination occurs on an estimated 2.5 cm^2 of the patient's skin, which during transmission mode is roughly at 25 mJ/cm^2. The system has a 590-element ultrasound detector array with 2 × 2 mm sized element and 3.2 mm distance between elements. Since only one channel receiver is available, a sequential reading of the elements occurs. The axial resolution provided at different depths is between 3.2 and 3.9 mm, while the lateral resolution is between 3.1 and 4.4 mm [58, 83-86].

1.5.2 Laser Optoacoustic Imaging System (LOIS-64)

The patient is placed in a prone position, and one uncompressed breast is inserted into the system's semi-cylindrical cup. The ultrasound detector array is arc-shaped, has a central frequency of 1.25 MHz, and is capable of rotating around the cup. The ultrasound detector is 19 cm long with a 2 cm width and entails 64 anisotropic rectangular elements with each at 3 × 20 mm. A 757 nm pulsed Q-switched Alexandrite laser source illuminates each breast perpendicularly to the arc. It has an output of ≤ 750 mJ. It illuminates large breast areas leading maximum skin illumination of 10 mJ/cm^2 per pulse. The outcome is a two-dimensional 20 mm thick image with an estimated 0.5 mm resolution. The arc rotation ensures breast coverage occurs in three dimensions [87].

1.5.3 The 512-detector Optosonics Photoacoustic Mammography System

The Optosonics 512 PAM system is an upgrade of the Optosonics 128 PAM system. The patient is placed in a prone position and one breast is placed in an acoustically and optically transparent plastic cup. The cup is surrounded by an imaging bowl filled with water and has a radius of 100 mm. A tunable 10 Hz optical parametric oscillator laser system ranging between 680 and 950 nm with a maximum output of 300 mJ illuminates the bowl from the bottom. It has 512 detector elements, which ensures larger breasts can be imaged, and the central detector frequency is 2 MHz. The elements are placed around the bowl, and each has a size of 3 × 3 mm. The detector array is rotated around the vertical axis, which leads to the increased sampling projections that have spiral scan patterns. The system implements a single wavelength Alexandrite laser source with 756 nm, which has ensured the skin illumination is at 10 mJ/cm^2 per pulse. The system has an image resolution of 0.42 mm and an imaging depth of 5 cm. Greater depths that go up to 5.3 cm lead to a degradation of the contrast to noise ratio (CNR) by the electronic noise from the system. A 3.2 minute spiral of 240 mm in diameter is required to cover an entire breast [57, 88].

1.5.4 Single-Breath-Hold Photoacoustic Computed Tomography (SBH-PACT)

The patient is placed in a prone position, and one breast is placed through an aperture in the bed. An Agar pillow is placed below the breast which presses it against the chest wall lightly. A 1064-nm laser is placed under the bed, which is directed upwards in a donut shape to illuminate the patient’s breast. The SBH-PACT scans a patient’s entire breast in one single breath-hold that lasts for an approximated 15 seconds. This yields a volumetric breast image that has detailed angiographic structures with negligible motion artifacts, which are often induced by the patient’s breathing. 2-D panoramic acoustic detection is achieved using a 512 full ring element ultrasonic transducer array, which assists in the detection of PA waves around a patient’s breast. A linear stage is used when motorizing the transducer array to scan the breast in an elevated form. Four 128 channel preamplifier sets and acquisition systems are directly connected to the array. The PA signals are recorded by the data acquisition systems within 100 µs of each laser pulse activation. The system also includes an estimated 4 cm and over in vivo deep penetration depth. The features also include high temporal and spatial resolutions where the frame rate is 2-D 10 Hz and a plane resolution of 255 µm [89, 90].

Table 1: Four different breast photoacoustic mammography (PAM) systems that have been reported with the human examination (In vivo)

PAT system	Illumination Method	Fluence	PA Acquisition	Max Depth	Spatial Resolution	Limitation
The Twente PA Mammoscope	Single-beam illumination (opposite to the US transducer) 16 mm diameter beam. (1064 nm – 10 ns at 10 Hz)	25 mJ/cm^2	Array-based US detector 90 mm field of view 590 elements (1 MHz Central Frequency)	15 mm	3.2 – 3.9 mm	Breast compression will push the blood out of the tissue. Long duration test. Spatial resolution is poor relative to MRI and CT.
LOIS-64 PAM	Single point 70 mm diameter (custom-made optical fiber bundle and expanded with the lens system) 757 nm	10 mJ/cm^2	19 cm Arc-shaped US detector 345 elements (1.25 MHz Central Frequency)	26 mm	0.5 mm	Arc rotation may change breast geometry. Limited breast size (based on the radius of the Arc-shaped transducer 70mm radios and 90 mm width)
OptoSonics-512 PAM	Bottom illumination (diffused beam) (756 nm experiment) The laser is 680 to 950 nm.	10 mJ/cm^2.	512 US elements organized in cup-shaped bowl Can cover from 24 to 96 mm radius (2 MHz Central Frequency) Enhanced spatial resolution.	53 mm	0.42 mm	They used a cup made of polyethylene terephthalate (PETG) to change the shape of the breast (compressed). Penetration depth was 53 mm. Beam illumination is a single diffused beam that came from the bottom and could miss any masses close to the chest wall.
Single-Breath-Hold Photoacoustic Computed Tomography (SBH-PACT)	Bottom illumination (using diffuser and lens to make donut-shaped beam) 1064 nm	20 mJ/cm^2	Full-ring US transducer with 512 elements 2.25 MHz Central Frequency.	~32 mm	255 µm	Compression pillow could change the geometry of the breast and push the blood out of the tissue. It might be hard to reach the regions closer to the chest wall due to the limitations in vertical diffusion of the light into the breast tissue.

1.6 Problem Statement

Modification of existing UST screening by adding an adjunct practical PAT modality to acquire additional diagnostic data (molecular and functional) will help to improve specificity in the classification and characterization of breast masses. Developing new breast imaging techniques based on US and PA tomography principles will help to reduce the number of unnecessary benign biopsies. In addition, this approach may help to increase early detection of breast cancer, which will help reduce the breast cancer mortality rate. However, the developed system should avoid any limitations that could be caused by the illumination and acquisition methods. After reviewing existing breast PAT modalities that have been used in human studies, which are summarized earlier in **Table 1**, it is found that:

- There is an issue with changing the breast morphology by either squeezing the breast between the US elements and the optical window or by compressing the breast toward the chest wall using pre-sized cups. Breast squeezing will change the morphology of the breast and may push the blood, which is an important component for PAT imaging, out of its original location.
- There are limitations in using the point illumination (single-beam illumination) method that has been used to direct the laser beam to a small area of the breast tissue. When the laser energy increases in the point illumination mode, to increase the penetration depth, there is a high PA signal reflected from the outer surface. Besides, there is a limited range of laser energy that, for safety, cannot be exceeded to keep the laser energy below the ANSI limit [91].
- Using optical lenses to direct the laser beam over a large area of the breast reduces the range of wavelengths available for spectroscopic imaging due to possible chromatic aberrations.

- Arc-shaped or plane-shaped transducer of the acoustical signals are not practical with breast tissue PA screening; therefore, there is a need for more US elements which should surround the targeted cross-sectional area (enclosed the breast tissue).

1.7 Proposed Solution

As mentioned earlier, among UST strategies, ring-acquisition (utilizing a ring-shaped US transducer) has been clinically shown to be capable of robust and accurate acoustic imaging for breast tissue characterization. This UST system could be easily combined with a novel omnidirectional full-ring optical system to become a complete breast US/PA tomography system. The main advantage of full-ring illumination is to direct the laser beam to the targeted area located in front of the ring US elements, which help to increase the penetration depth in the targeted scanned slice of the breast. For this reason, the full-ring illumination method will enhance the penetration depth and direct the laser beam to the targeted scanned area. The full-ring illumination method has been used in other applications by deploying either a conical lens or cone mirror combined with an acoustically penetrable optical reflector (APOR) [92, 93]. However, the APOR's is an impractical solution for breast PAT application because it has a low power threshold and acoustical transparency which make it impractical solution for full-ring illuminated systems. At the same time, the APOR transmission coefficient is affected by the incidence angle of the acoustical signal [92], so in case of using a 45-degree APOR in the breast PAT, there will be about 65% transmittance of the US signal. Conversely, possible chromatic aberrations could be observed at any design using lenses to create a ring beam [94, 95] which reduces the wavelengths available for spectroscopic imaging. To overcome earlier limitations, the full-ring US/PA tomography system using mirror-based omnidirectional optical reflectors was designed.

To practically create a ring beam for breast PAT imaging, the novel omnidirectional, full-ring illumination optical system consists of a cone-shaped reflector and two large conical reflectors. All three optical reflectors are designed to create a ring-shaped laser beam from a collimated laser beam. The full-ring beam is directed to the targeted cross-sectional slice of the scanned object that is located in front of the US elements of the ring US transducer (**Figure 4**). The design and principle of work of this option are explained more fully in the next section (**1.8**). Developing the novel omnidirectional optical system and combining and synchronizing it with UST will make it innovative and fundamentally different from other PAT systems. This will create several advantages regarding tissue illumination and data acquisition, such as:

- Positioning the ring beam to the scanned region only, which is located in front of the US elements of the ring beam, will increase the penetration depth in the targted region.
- Distribution of the laser beam on a large, ring-shaped area, instead of small point area, will increase the range of the applied fluence without compromising standards of the American National Standards Institute (ANSI) for the safe use of lasers maximum permissible exposure (MPE) [91].
- Equal distribution of the laser beam on one slice will create a uniform fluence in the targeted cross-sectional slice, which will result in uniform PA signals.
- Using optical reflectors (mirrors) instead of optical lenses will give an unlimited range of laser wavelength in spectroscopic applications (No chromatic aberrations).
- Reduce the beam reflectance that could be created by applying higher energy at a small spot of the breast skin (point illumination).
- Using a ring US transducer will increase the efficiency to detect the PA signals from multiple points around the scanned slice of the object.
- The principle of PA imaging, which is based on the light absorption at different wavelengths, will give broad breast imaging applications by use angiogenic biomarkers and molecular contrast agents.

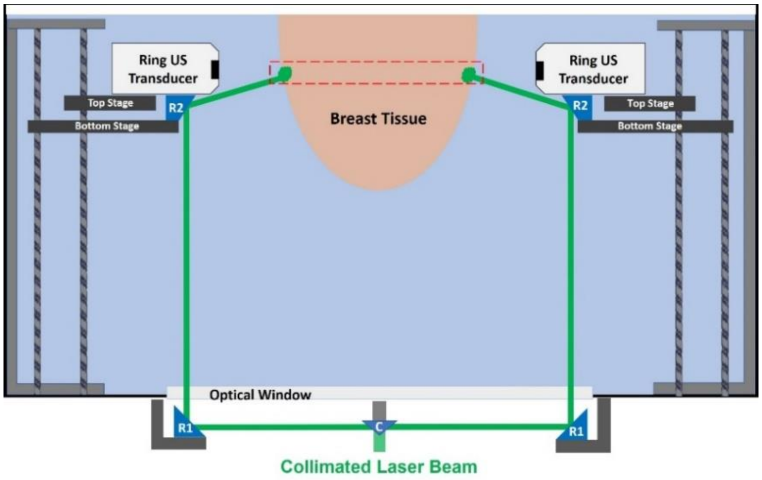

Figure 4: Path of the collimated laser beam in the system to create a ring-shaped laser beam that can be directed to the specified cross-sectional slice of the breast tissue. The ring-shaped beam is generated by using one cone-shaped reflector ”c” and two conical reflectors (R1 and R2).

In addition, extra advantages can be achieved by using the full-ring illumination US/PA tomography system in clinical application, such as:

- Maintenance of the breast shape by not applying any force will help to keep the morphology of the breast tissue.
- Comfort (no breast compression), point of care, and non-ionized breast US/PA tomography screening.
- Because the linked UST can cover about 90% of the breast tissue, the PA imaging will be able to get PA data from the horizontal cross-sectional slices that are located close to the chest wall.
- Using the valuable imaging data provided by the UST system equipped with the ring US transducer, such as SOS and AA, will help to create a complete, entirely compensated, quantitative PAT tomography system (**Figure 5**).

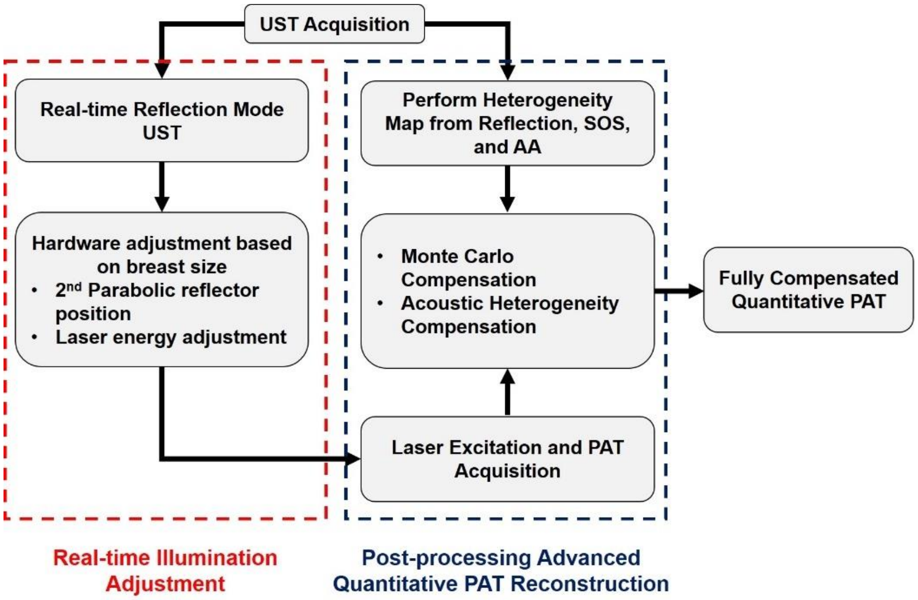

Figure 5: Block diagram illustrates the steps required to achieve the final fully compensated quantitative PAT system.

1.8 Design and Development of an All-reflective Omnidirectional Ring Illumination Optical System

1.8.1 Optical components needed to achieve omnidirectional full-ring illumination

The main aim for the optical system is to create an omnidirectional full-ring beam that can practically direct the ring beam to the targeted cross-sectional slice of the breast and can be easily adjusted based on the diameter of the slice to be scanned. Using conical reflectors with a cone-shaped reflector will help for this purpose. The omnidirectional optical part with full-ring illumination consists of one cone-shaped reflector and two conical ring-shaped reflectors, as shown in **Figure 6**. The 45-degree cone-shaped reflector will be placed at the center point of the first stationary conical reflector, both of which will be located outside the imaging tank. When the collimated laser beam enters the system from the bottom, it will hit the 45-degree cone reflector, resulting in a flat, horizontal, disk-shaped beam pattern. The next sequence occurs when the flat-disk beam pattern is directed to the first conical reflector (R1) and subsequently is reflected in the form of a hollow cylindrical beam pattern entering the imaging water tank through the optical window and moving towards the second conical reflector (R2). The second conical reflector converges the beam towards the center vertical line of the ring US transducer. It is important to mention that the second conical reflector is custom-designed for a specific ring US transducer and object geometry to generate a ring-shaped beam on the object being scanned (breast tissue). In addition, the cone-shaped and first conical reflectors are stationary, while the second conical reflector moves along with the ring US transducer during US/PA tomography scanning inside the water tank.

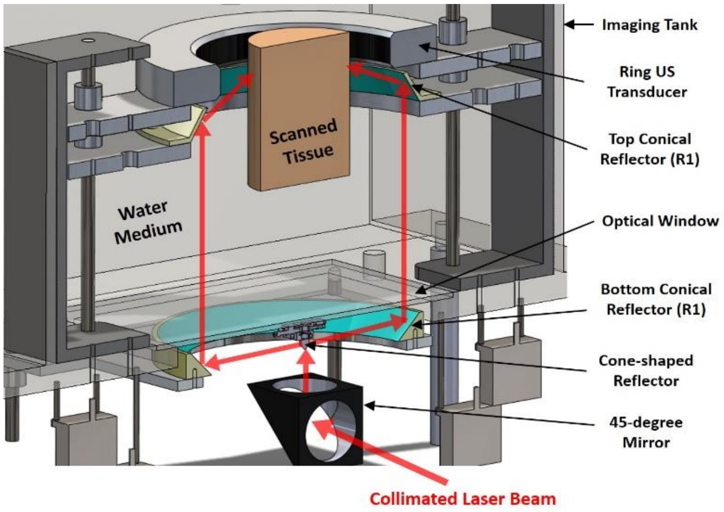

Figure 6: 3-D diagram of the proposed full-ring US/PA tomography system shows the 45-degree mirror, cone-shaped reflector, two ring-shaped conical reflectors, optical window, and ring US transducer.

Ideal illumination that causes higher fluence inside human tissue occurs when the ring laser beam falls vertically on the targeted surface (90-degree beam angle to the scanned surface). This illumination could be achieved by using a 45-degree conical reflector aligned with the targeted cross-sectional slice. However, it is not possible to implement this condition in the US/PA tomography prototype because the ring US transducer elements will create a barrier in front of the laser beam. For this reason, it is essential to optimize the angle of the conical reflector to get the best illumination incident angle (closer to 90 degrees) and also get a maximum ring beam diameter that can cover an average breast size. Based on the current geometry of the ring transducer, the reflection angle of the second conical reflector is initially set at 57 degrees, which makes the beam fall at a 66-degree angle to the targeted surface of the scanned object (**Figure 7**). The conical reflector was tested geometrically and with ray-tracing, and it was proved that it could cover a maximum of a 140 mm breast diameter.

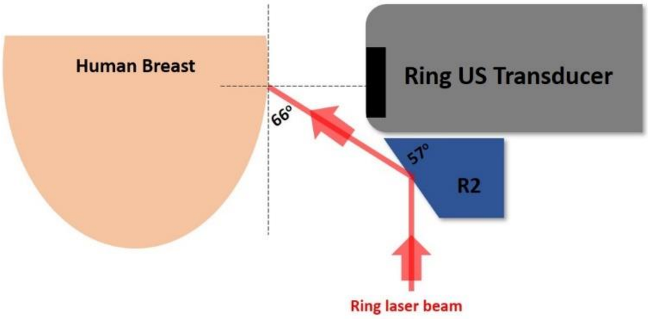

Figure 7: 2-D graph shows the part of the ring US transducer, the second conical reflector (R2), and the incident angle of the ring beam on the human breast.

1.8.2 Efficiency of the optical path and optical components for omnidirectional light delivery

There are two main parameters in PA and optical applications that are related to each other and should be calculated before designing the reflectors. These are fluence (energy density - J/area) and intensity (laser power - W/area). The two parameters should also be maintained during operation to protect the breast tissue as well as the optical components and to achieve optimal performance. The whole data should be calculated and summarized in multiple tables to ensure optimum reflectivity under maximum permissible exposure (MPE) of the human skin at each wavelength. For example, according to the ANSI standard, the MPE of human skin at a 532 nm wavelength is about 20 mJ/cm^2 [91].

There are several factors that could affect the efficiency of the optical components' reflectivity. These include coating material, surface flatness, and surface quality. To achieve optimum illumination, all reflectors should be made with coated material that gives a high reflection percentage in the targeted wavelength spectrum and is compatible with a water medium. In addition, it should have a high damage threshold (J/area) with applied laser pulses at wavelength spectrum. The bottom optical glass window, which passes the hollow-shaped cylindrical beam, should be made with a material that is able to resist the high force that will be created from the water volume and that can pass a high percentage of the laser energy (high transmittance). For the preliminary option, the optical mirrors will be made from a Polymethyl Methacrylate (PMMA) material and coated with protected silver, which has a high reflectivity percentage in the targeted wavelength spectrum, as compared with other coating materials **(Figure 8a)**. Protected silver was chosen because of its high reflectivity (about 95%) in various near-infrared (NIR) wavelength ranges. In addition, the damage threshold is higher than other comparable materials such as protected aluminum. For the optical window, 5 mm thickness H-K9L glass is used, which has the same specifications as BK7 glass material and can transmit about 93% of the laser energy at NIR wavelength **(Figure 8b)**.

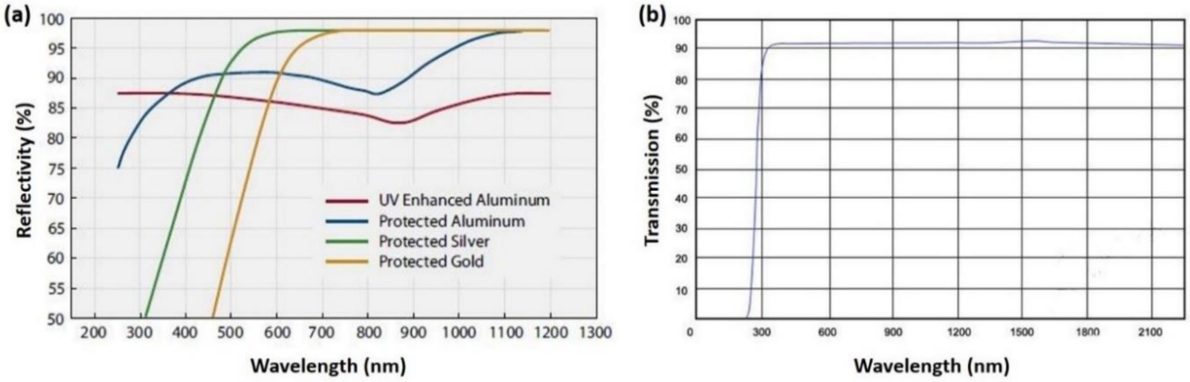

Figure 8: (a) Percentage of reflectivity at different ranges of wavelengths (200 nm – 1300 nm) of some protected coating materials. Protected silver (green) shows high reflectance in the NIR wavelength [2]. (b) Transmittance percentage of the laser energy for H-K9L glass in the wavelength range between 200 nm and 2100 nm [3].

---

[2] The graph was adapted and modified from http://www.standaphotonics.com/metallic-coated-optics/

[3] The graph was adapted and modified fromhttp://www.nthsgx.com/en/pro_show.asp?cat_id=188&i_id=36&b_tb=user_pro

In front of the laser and below the imaging tank, there is a 45-degree reflecting mirror that directs the collimated laser beam to the cone-shaped mirror. This 45-degree reflector and the cone-shaped mirror will receive the highest laser beam energy that will be converted to a ring-shaped beam, so those reflectors should be coated with a material that can resist and reflect maximum laser energy, such as a protected silver coating. The transmitted energy was calculated of the four protected silver mirrors (45-degree, cone-shaped reflector, and two conical reflectors) and the H-K9L glass optical window and found that it will be a minimum of 76 % at 740 nm **(Figure 9).**

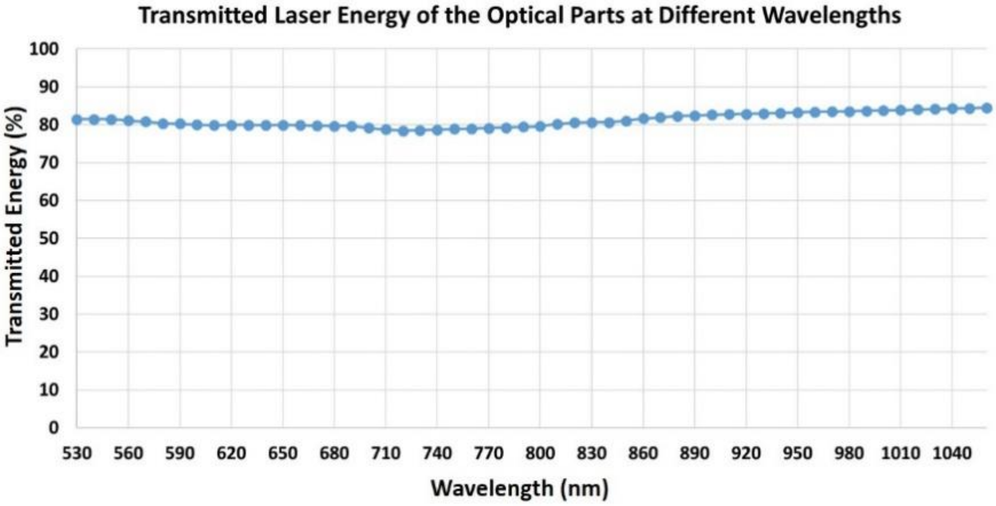

Figure 9: Transmitted laser energy in the proposed omnidirectional full-ring illumination system.

Providing sufficient fluence for the targeted cross-section while avoiding the MPE limit for the tissue is a significant challenge for PAT breast imaging. As mentioned earlier, one of the key advantages of the proposed full-ring illumination system is its ability to disperse the laser energy over a larger area to keep the fluence below the ANSI limits. For example, a 10 mm diameter laser beam, with 150 mJ/pulse energy will result in fluence of 191 mJ/cm^2 (at 532 nm). However, using the proposed all-reflective optical system to create the omnidirectional ring illumination pattern, with a 5 mm thickness and a 100 mm diameter cross-sectional area, will result in fluence of 9.55 mJ/cm^2, which falls within the safe fluence range for imaging human tissue. In this example, it was assumed there was no energy loss due to the use of four protected silver mirrors and optical window. Comparing the full-ring to the point illumination, the fluence of the proposed illumination system is about 20 times smaller than point illumination; also it is below the MPE limit which is 20 mJ/cm^2 for 532 nm.

CHAPTER 2 - DESIGN AND DEVELOPMENT OF THE OMNIDIRECTIONAL US/PA TOMOGRAPHY SYSTEM

At the beginning phase of this research, it was essential to study the concept of US/PA tomography with available resources. The main principle of full-ring tomography is to illuminate the whole cross-sectional slice with a full-ring beam and acquire a full set of data with ring acoustical elements that surround the scanned object. The array-based US/PA tomography was built and optimized to initially evaluate tissue-mimicking phantoms as well as murine models to provide preliminary knowledge about US/PA tomography, illumination methods, integration of the system, and breast mimicking phantoms.

2.1 Array-based US/PA Tomography System – Technical Features

For the array-based US/PA tomography system, it was decided to rotate the scanned object 360 degrees and keep the transducer as well as a laser source in a fixed position. The array-based US/PA tomography system consists of three main units. The first unit is the fully digital, programmable US engine (Verasonics Vantage 128, equipped with L11-4v transducer [4]) which can be used to scan the sample and detect acoustical signals. The second unit in the system is the pulsed laser source (Spectra-Physics Quanta-Ray PRO 270 / GW Versascan OPO) that can be used to illuminate the scanned sample with high energy at various ranges of wavelengths. The third unit is the scanning unit, where the sample is placed for imaging. The scanning unit consists of a cylindrical water tank that has a translational/rotational stage that is operated by two stepping motors. In addition, there is a mechanical gas chamber that can pass

---

[4] http://verasonics.com/verasonics-transducers/

anesthesia gas to and from a live animal as it is rotated on the stage. Because the system was developed to operate backward, orthogonal, and combined backward and orthogonal PA modes, the scanning unit has two adjustable optical windows placed at zero and 90-degree positions (**Figure 10a**). In addition, there are two acoustical windows located at 180 and 270 degrees, where the linear array US transducer is placed (**Figure 10b**).

The motorized scanning system is controlled by a custom-built lab-view (NI-DAQ) control program that can rotate the sample with pre-set angles (as small as 1.8 degrees) and translational motion with a resolution of 100 µm. The automated working principle in this system was designed based on a trigger-out signal that comes from the NI-DAQ. In US/PA applications, the NI-DAQ sends a trigger-out signal to the US engine once the sample rotates to the new scanning position. This signal makes the US engine acquire US data and then the PA acoustical data after getting a trigger-pulse from the laser engine (**Figure 10c**).

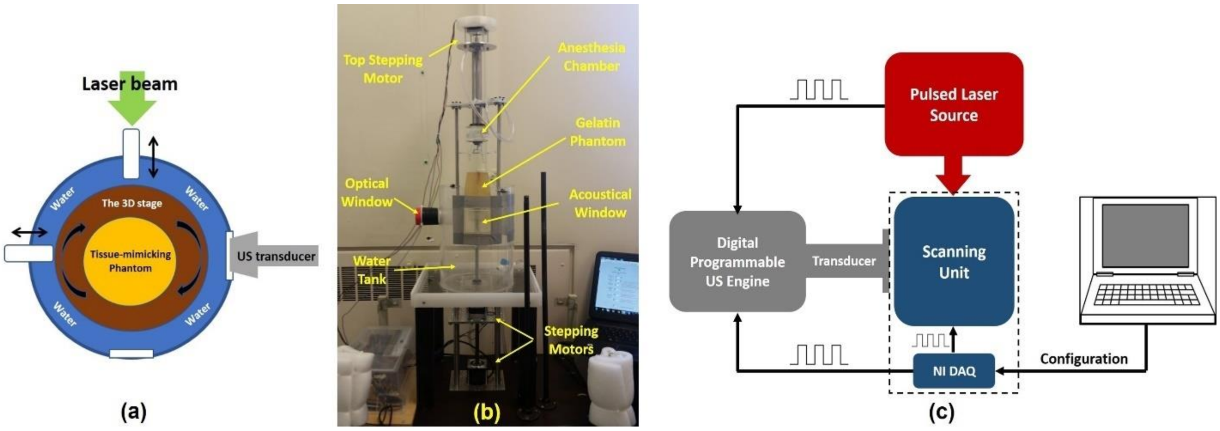

Figure 10: (a) Top-view of the scanning unit of the array-based US/PA tomography system (b) Photograph of the array-based US/PA tomography system showing main parts of the scanning unit of the developed array-based US/PA tomography system (c) Block diagram of the array-based US/PA tomography system showing the principle of system integration.

2.2 Preliminary Studies Using the Array-based US/PA Tomography System

In several experiments, the array-based US/PA tomography system has been used to study different types of samples to evaluate the efficiency and observe possible challenges in using US/PA tomography imaging system.

2.2.1 Resolution of the array-based US/PA tomography system

The theoretical resolution (axial and lateral) [96, 97] of the linear-array US transducer was calculated by using three equations:

$$\lambda = 2 * \frac{c}{f} \tag{2.1}$$

$$Axial\ Resolution = \frac{1}{2} * \lambda \tag{2.1}$$

$$Lateral\ Resoultion = \frac{F * \lambda}{D} \tag{2.3}$$

where λ refers to the wavelength of the ultrasound, c is the speed of sound in water at 25° C (1479 m/s), f is the central frequency of the US transducer (6.25 MHz), F is the focus number (35 mm), and D is the transducer transmit surface width (39 mm). It was founded that the system has 239.5 µm axial resolution and 430 µm lateral resolution at 1 cm imaging depth.

The imaging resolution of the tomography system was tested by using a calibration phantom consisting of ultra-thin wires. Three ultra-thin wires with 120 µm thickness were mounted on the scanning stage inside a diffused medium. The distance between each wire and the center point of the stage was 12.5 mm (**Figure 11a**). The water medium was diffused by adding 0.02% milk. The phantom was illuminated with 20 mJ/pulse at a 532 nm wavelength (due to the availability of Nd:YAG pump laser), and twenty US and PA frames were acquired. To get the final US and PA tomography images, a high-intensity filtered back projection (FBP) was applied using MATLAB software to restore the combined volumetric US and PA images. After completing the image reconstruction and calculating the pixel resolution, which was 9.6 µm, it was concluded that the system could achieve a planar resolution of less than 150 µm (**Figure 11b**).

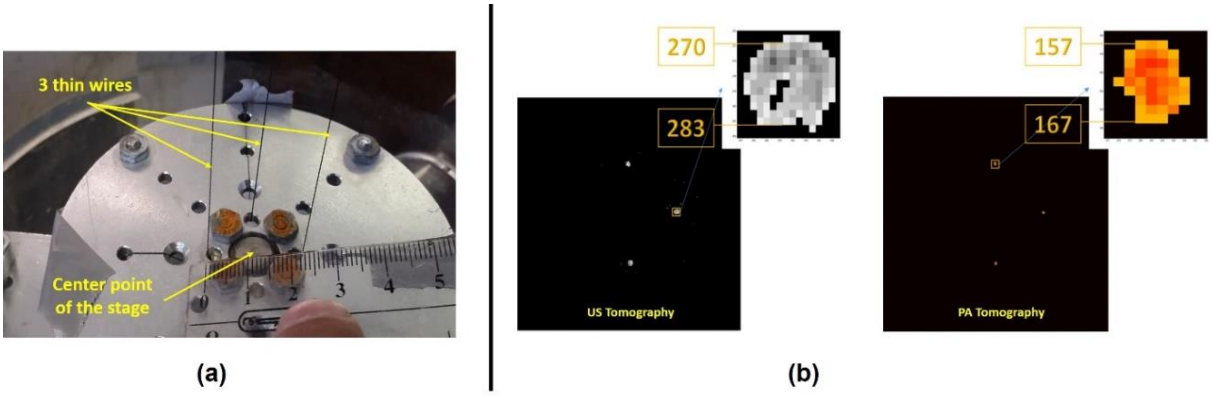

Figure 11: (a) Photograph shows the position of the wire in the rotational stage of the array-based US/PA tomography (b) US and PA tomography results from the resolution test.

2.2.2 Imaging blood using array-based US/PA tomography system

The primary aim of this experiment was to show the benefits of having the PA data as a complement to the US data. In this experiment, the phantom consisted of five thin glass tubes; each tube diameter was 3 mm. Three tubes were filled with water, while the other two were filled with light-absorbing material (bovine blood). The distance between each tube was set at 10 mm, and the phantom was placed at the center of the scanning stage (**Figure 12a**). The scanning unit was filled with 10 L of water mixed with 20 ml of milk to make the medium diffusive. The linear-array transducer (L11-4v) was placed on the scanning window located 90 mm from the center of the scanning stage (**Figure 12b**). The optical window was adjusted to a distance of 35 mm between the edge of the optical window and the phantom’s center, so the farthest tube was at a 45 mm distance from the optical window. The laser energy was measured in front of the optical window, and it was approximately 47 mJ/pulse (**Figure 12c**). Twenty US and backward PA frames (18-degree rotation angle) were acquired for one cross-section of the phantom. A variety of methods were used to perform tomography image reconstruction, such as FBP with PLS-TV denoising and a geometry-conversion reconstruction technique.

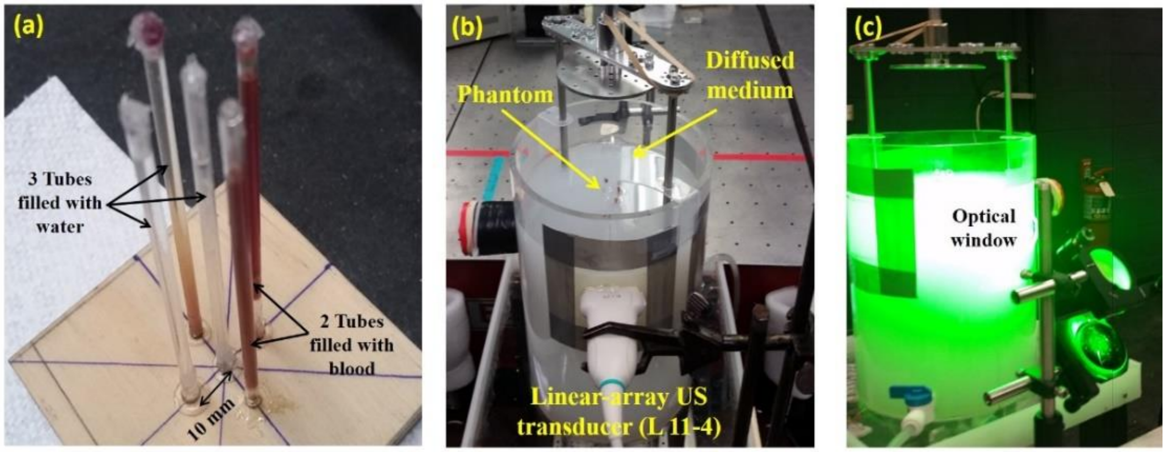

Figure 12: (a) Photograph of the test phantom (b) Front view of the array-based US/PA tomography system showing the experimental setup (c) Back view of the system displaying the optical window and the green laser beam (532 nm) diffused inside the tank filled with diffusive medium.

The co-registered US and PA images of the glass-tube phantom revealed the tube structures in the US tomography image while the presence of the light-absorbing material was shown in the PA tomography image (**Figure 13**). From this experiment, it was concluded that the presence of the PA tomography image helps to distinguish between objects that have high concentrations of blood (which are considered to be a sign of cancer cells) and the objects that are blood-free. The co-registered US/PA tomography images provide proof of the PA tomography benefits as a complementary tool to the US data.

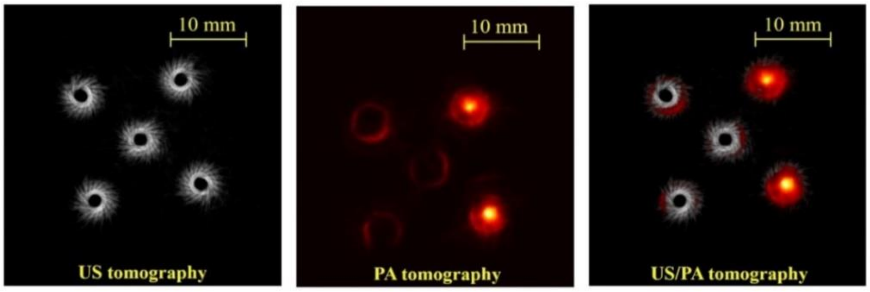

Figure 13: (left) Reconstructed US tomography, (middle) reconstructed PA tomography, and (right) overlaid USPA images of the test tube phantom, indicating the tube structures and the presence of light-absorbing material (blood).

2.2.3 Ex vivo whole-body mouse imaging

A fresh, euthanized athymic nude male mouse was used in this experiment to test the ability of the system to scan different organs inside the animal body. A dead mouse with shaved skin was mounted on the scanning stage to acquire US and PA frames of three different cross-sectional slices. The specific area under the thoracic cavity, which was expected to contain the abdominal organs, was chosen as the starting point. To make the medium diffusive, the scanning unit was filled with 10 L of water mixed with 20 ml of milk. The laser energy was approximately 73 mJ/pulse at a wavelength of 532 nm, and it was aimed in front of the tank's optical window. Twenty US and PA frames were acquired per cross-sectional slice, so there was a total of 60 US and 60 PA frames for three cross-sectional slices. Image reconstruction was performed by using various methods, such as a geometry-conversion reconstruction technique and FBP, to build the tomography images.

Final UST, PAT, and co-registered US/PA tomography images are shown in **Figure 14**. The reconstructed images have been examined by a specialist to define the unknown organs in the US tomography. The UST images were able to define the structure of all organs in the targeted slices, while the PAT images helps to define organs that have high blood concentration. The observed penetration depth in PAT images is about 10 mm. From the experiment it was conclude that strong PA signals are produced from all organs that have high blood concentration. Moreover, the PA imaging is a useful and complementary modality to the US imaging.

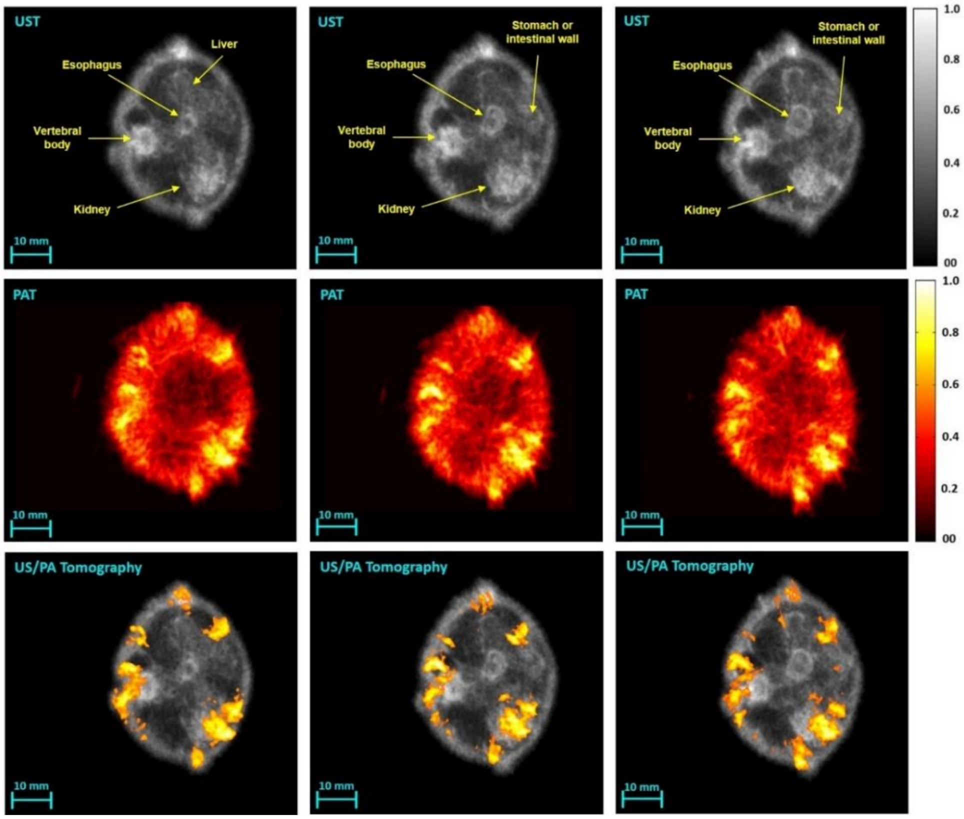

Figure 14: Reconstructed US tomography, PA tomography, and overlaid USPA tomography images of the dead mouse.

2.2.4 Conclusion and Discussion About Using Array-based US/PA Tomography

In the first section of the preliminary studies, successful experiments that have been performed with the array-based US/PA tomography system were presented. Initial results demonstrated the ability to combine US and PA modalities in one system to acquire US and PA tomographic images that contain both acoustical and optical contrast, and thus provide both anatomical and functional information of the tissue. In addition, these experiments showed the benefits of having US and PA techniques in one imaging system to distinguish the objects with high blood concentration.

However, the array-based US/PA tomography system has several limitations that could affect the quality and accuracy of the final results. The first limitation is related to the scanning procedure in the system, which depends on the rotation and translation of the scanning stage that holds the object. The results from this method could be affected by the length of time necessary for the scanning operation, which may increase the possibility of changing physical or molecular characteristics of the scanned object. The second limitation is the possible deviation that could happen in the scanning stage when it rotates around the vertical axis, which could affect the resolution of each cross-sectional slice. The illumination methods (point illumination and diffused beam illumination) were an additional limitation that was discovered after doing several studies because this method was sensitive to the high laser energy, especially with the dead animal skin. Once the laser energy was increased to increase the penetration depth, there was a high PA signal created from the light that reflected from the animal's skin. From earlier limitations, we can conclude that the future breast US/PA tomography system should have a practical illumination method compatible with the breast shape. In addition, it should be capable of performing fast scanning as a result of using a high-performance acquisition unit. These targets could be achieved by using a US/PA tomography system equipped with a ring US transducer and full-ring illumination method, which will be explained in the next sections.

2.3 Utilizing a Ring-shaped US Transducer for Photoacoustic Tomography Imaging - Preliminary Studies

2.3.1 Perform UST/PAT imaging by using different phantoms

To test the capability of synchronizing the current UST system with a pulsed laser to perform PAT imaging, two preliminary experiments were performed using a calibration phantom and a tissue-mimicking phantom. The first phantom consisted of eight pieces of a light-absorbing material (700 μm thickness graphite rods), aligned in a spiral order with known geometry, and then placed in the middle of the ring transducer (**Figure 15a**). The second phantom had a cylindrical shape and was made of 10% porcine gelatin (G2500, SIGMA-ALDRICH, Missouri, USA) and 0.2% cellulose (S5504, SIGMA-ALDRICH, Missouri, USA), which helped to create light scattering and an acoustic backscattered medium. A 6-mm diagonal hole was drilled inside the gelatin background, which was then filled with sterilized sheep's blood mixed with gelatin as an endogenous light-absorbing material (**Figure 15b**). The phantoms were illuminated by a 532 nm laser beam (Q-smart 450, Quantel Inc.) source with approximately 120 mJ/pulse of energy. The laser beam entered the water tank from the bottom to illuminate the spiral-shaped phantom from the center. A light diffuser made of gelatine and cellulose was placed in the laser beam path to distribute the laser energy into the entire phantom (**Figure 15c**). A field-programmable gate array (FPGA) was used as a master controller to synchronize the UST system with the laser source. Both US and PA signals were acquired, and PA images were reconstructed using an advanced iterative image reconstruction method that employed total variation-based regularization [98, 99].

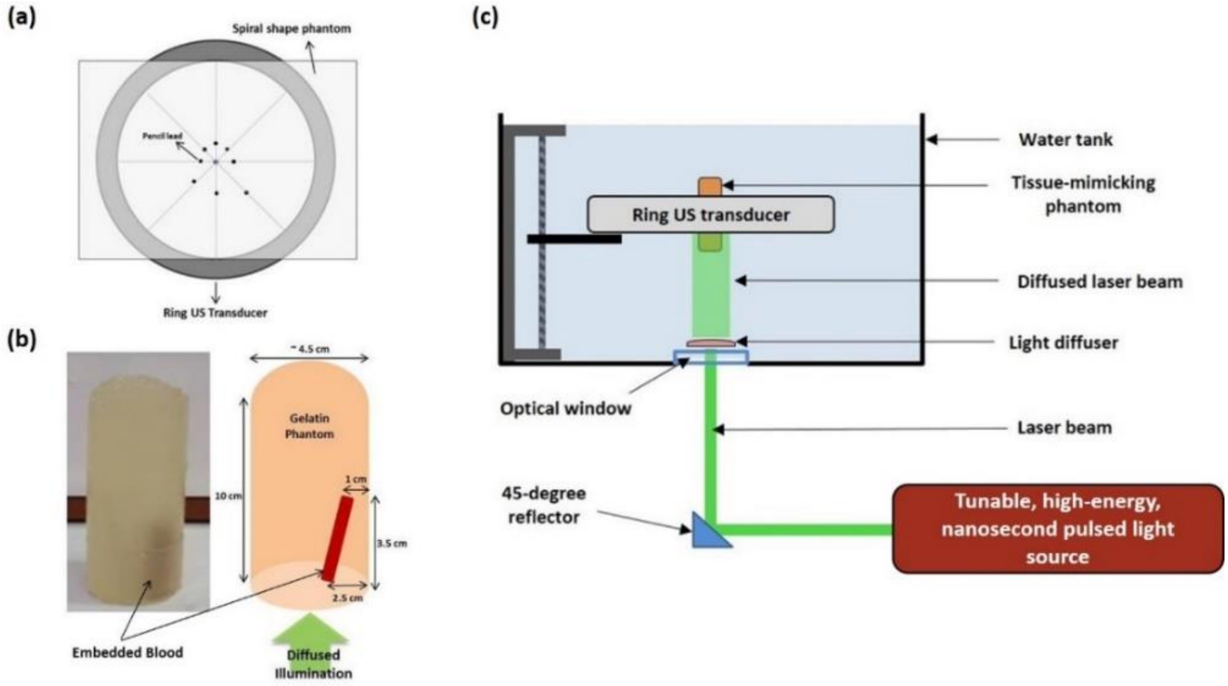

Figure 15: (a) Graph shows the top view of the spiral-shaped phantom made of eight (700µm thickness) pencil leads (b) Photograph and diagram of the tissue-mimicking phantom made of porcine gelatin and filled with sheep's blood (c) Figure showing the experimental setup for the cylindrical phantom with heparinized sheep's blood in the ring US transducer.

Figure 16 a and **b** present the reconstructed UST and PAT images of the spiral-shaped phantom within the ring US transducer. The spiral formation is easily identifiable in both images. The UST image shows an approximate 1 mm diameter of the pencil lead while the PAT image shows 0.77 mm. The objects furthest from the central source of illumination are not clearly discernable and that could be due to the lower fluence at that area. Nevertheless, the results indicate that the tomography system is capable of providing co-registered US and PA tomographic images.

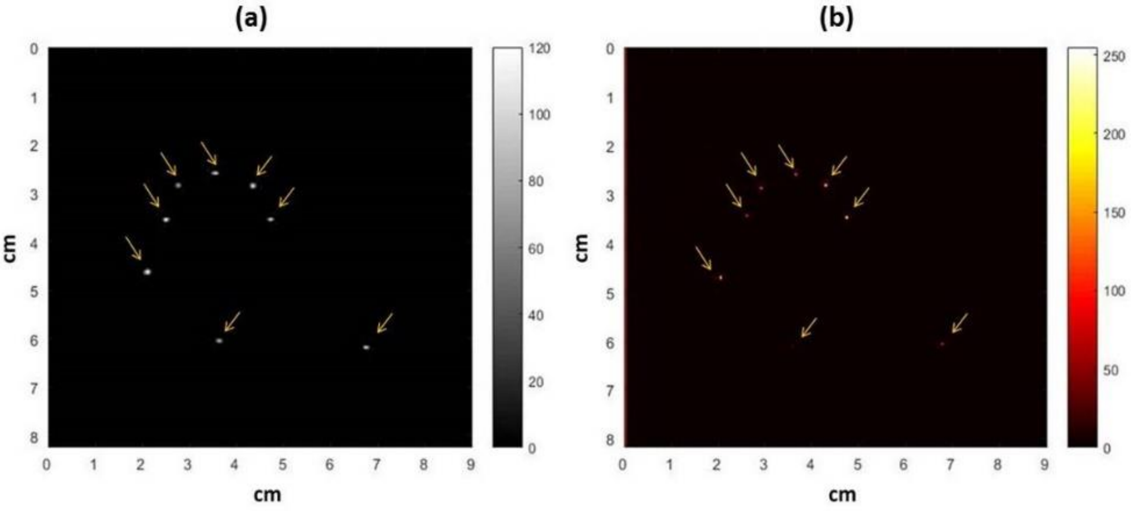

Figure 16: (a) UST and (b) PAT images of 700-micrometer graphite rods spiral phantom, as marked by arrows.

For the second experiment, **Figure 17** displays the UST and PAT reconstructed images and the co-registered results. The results indicate the reliability of the US/PA tomography system to detect a light-absorbing target (blood in this case) within a close-to-real acoustic medium and to provide combined images containing both acoustic and optical properties of the object. The US/PA image demonstrates the utility of using PA tomography in providing functional data, such as the presence of blood when co-registered with US anatomical data.

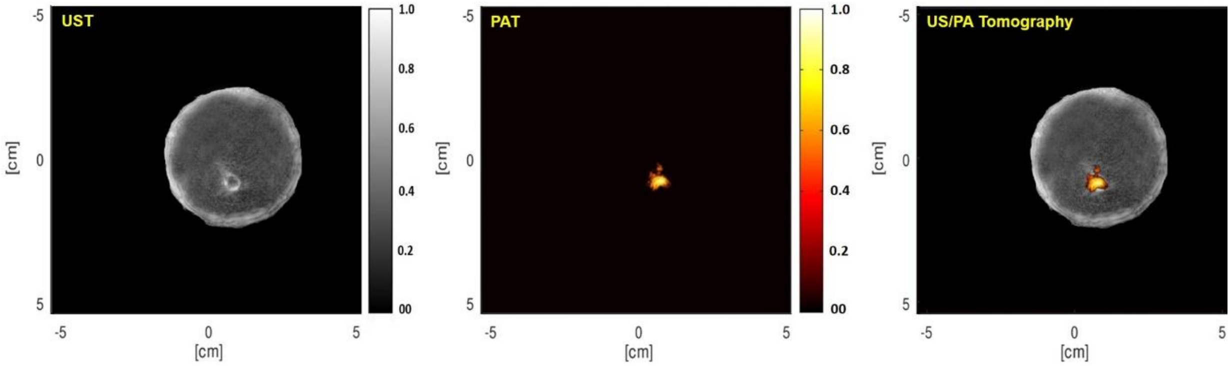

Figure 17: (left) UST, (middle) PAT, and (right) coregistered US/PA tomographical images a gelatin/cellulose cylinder with an internal cavity filled with heparinized sheep's blood. The UST image defines the structure of the scanned object while the PAT image determines the presence of blood.

2.3.2 Conclusion and discussion of the preliminary US/PA tomography studies

The combination of the UST and laser source to create US/PA tomography images is technically possible and can be useful for getting functional and molecular data of a scanned object. Future experiments should include multiple slices scan by full-ring illumination method to observe the efficiency of the proposed method on different cross-sectional slices. The proposed full-ring optical system will be added to the UST system to conduct several experiments. The results will show a complete US/PA tomography that will be acoustically acquired by the ring US transducer and illuminated by the ring laser beam.

2.4 Omnidirectional Full-ring US/PA Tomography System Using a Single Parabolic Reflector (First Prototype)

After completing previous experiments and defining the benefits of having a reliable illumination method, it was mandatory to build a US/PA tomography system capable of performing a full-ring illumination. In this section, the main parts of the US/PA tomography system and how it works will be discussed. The system explained in this section is considered as the first prototype, and it will be used in all experiments in this thesis (**Figure 18**).

The first unit is the digital UST engine equipped with a ring US transducer that enfolds the scanned object to detect the acoustic signals from multiple horizontal cross-sectional slices. The second unit in the system is the pulsed laser source that is able to illuminate the scanned sample with high energy at multiple wavelengths. The third "main" unit in the system is the scanning unit that has all parts required to perform full-ring illumination inside a water medium.

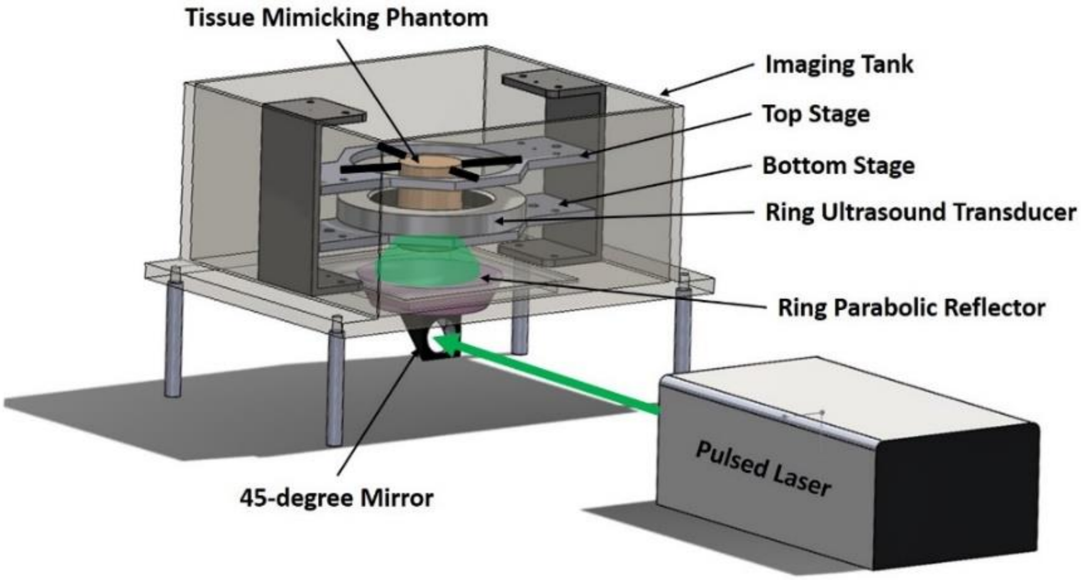

Figure 18: Graph illustrates the main parts of the omnidirectional US/PA tomography system using a single parabolic reflector to create a ring beam.

2.4.1 Pulsed laser source

The laser source used in this prototype is a High Energy (HE) Nd:YAG / OPO laser (PhocusCore, Optotek, California, USA). The 10-Hz pulsed laser can create a 532 nm wavelength beam. In addition, the wavelength can be tuned to any value within 650 - 1064 and 1200 - 2400 nm at every pulse. The peak pulsed energy that could be achieved in the NIR region was 180 mJ (**Figure 19**). In the path of the laser beam, there is a protected silver 45-degree mirror, located below the imaging tank, used to change the laser direction which allowed it to enter the imaging tank.

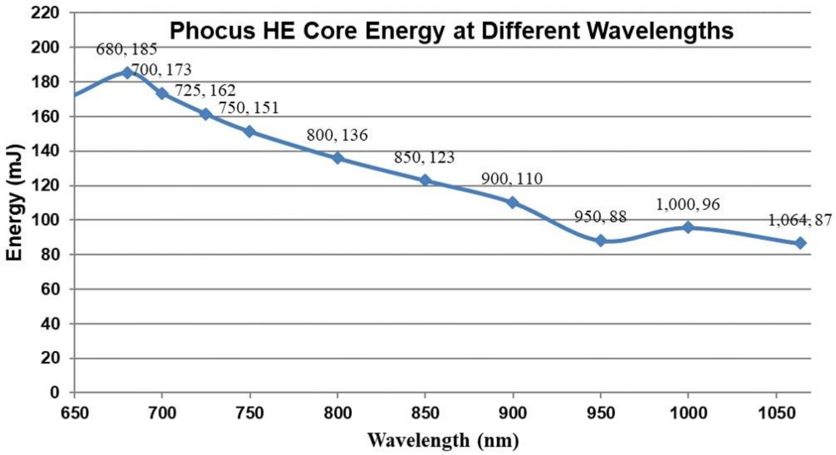

Figure 19: Graph showing the change in the high energy (HE) laser pulse (mJ) at a different wavelength.

2.4.2 Digital UST engine equipped with ring US transducer

The prototype UST employs a 200-mm inner diameter and is comprised of 256 elements, with an element pitch of 2.45 mm and a height of 9 mm. The system can create a 3-D image of the breast by translating the ring US transducer, which enfolds the breast tissue, to collect a 2-D data set of multiple cross-sectional slices. The scattered (transmission) and backscattered (reflection) ultrasound signals are subsequently recorded by all 256 elements at a sampling rate of 8.33 MHz, and the receiver can produce a single UST slice in approximately 30 ms. The signal scattering is small with the ring UST transducer operating at a central frequency of 2 MHz dependably penetrating the entire breast. UST images are created by applying a waveform algorithm to data from the UST scans. The system can get (5 × 0.5 × 0.5) mm^3 volume image resolution.

To perform UST/PAT experiments, the system has a separate configuration to control the parameters in each imaging. For UST, the transmit output voltage should set to 150 V_{pp}, and the system should be adjusted to the transmit function. In the UST imaging, the time gain was to 20 dB, which is appropriate with the preset reconstruction codes to create reflection, SOS, and AA images. On the other hand, the PAT configuration uses 20 dB time gain, 2 V_{pp} output voltage, and shut down the transmit function. In both UST and PAT configurations, the received sample rate is set to be 8.33 MHz. The other configuration under Slice Definition Parameters (**Figure 20**) is adjusted in PAT imaging based on the specification of the pulsed laser.

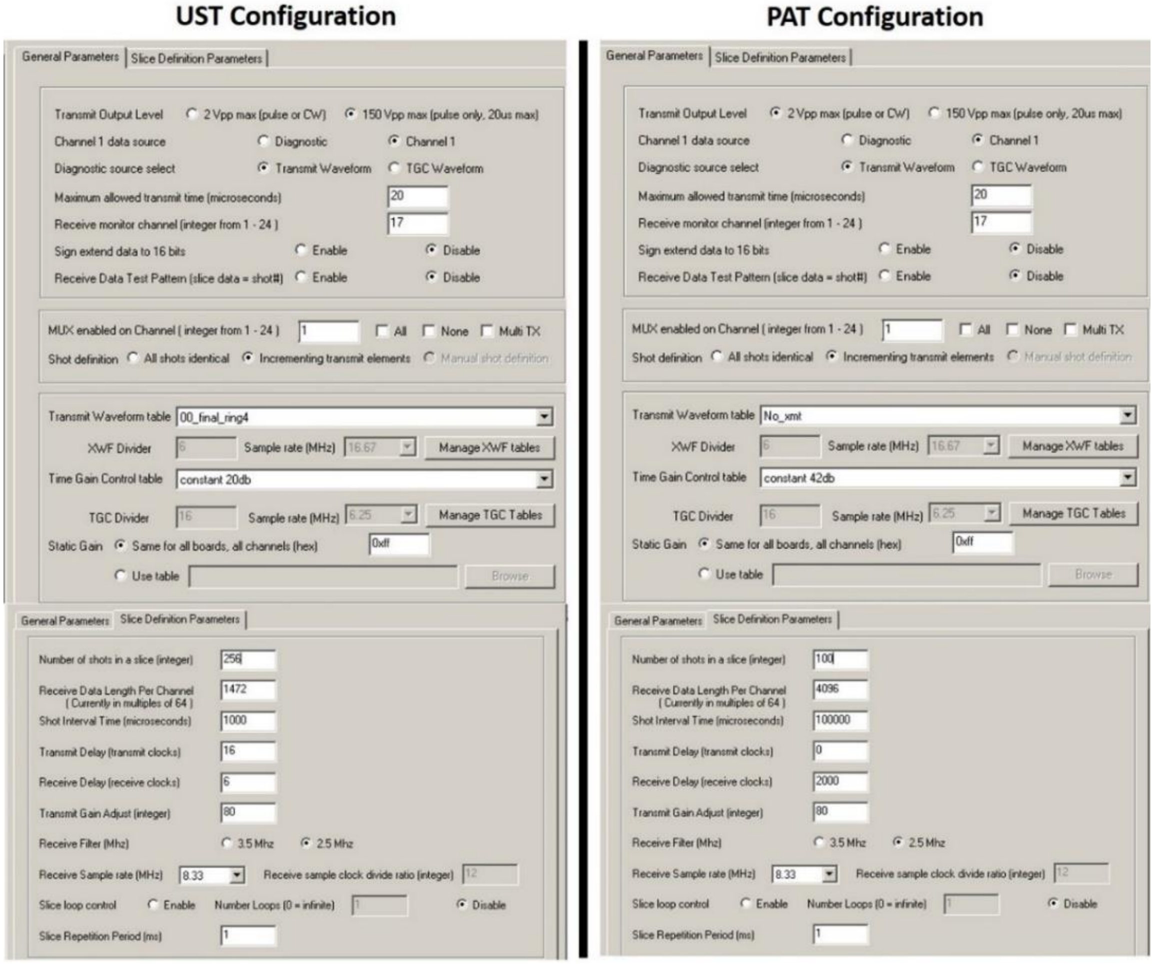

UST Configuration

Transmit Output Level ○ 2 Vpp max (pulse or CW) ● 150 Vpp max (pulse only, 20us max)
Channel 1 data source ○ Diagnostic ● Channel 1
Diagnostic source select ● Transmit Waveform ○ TGC Waveform
Maximum allowed transmit time (microseconds) 20
Receive monitor channel (integer from 1 - 24) 17
Sign extend data to 16 bits ○ Enable ● Disable
Receive Data Test Pattern (slice data = shot#) ○ Enable ● Disable
MUX enabled on Channel (integer from 1 - 24) 1 ☐ All ☐ None ☐ Multi TX
Shot definition ○ All shots identical ● Incrementing transmit elements ○ Manual shot definition
Transmit Waveform table 00_final_ring4
XWF Divider 6 Sample rate (MHz) 16.67
Time Gain Control table constant 20db
TGC Divider 16 Sample rate (MHz) 6.25
Static Gain ● Same for all boards, all channels (hex) 0xff
○ Use table
Number of shots in a slice (integer) 256
Receive Data Length Per Channel (Currently in multiples of 64) 1472
Shot Interval Time (microseconds) 1000
Transmit Delay (transmit clocks) 16
Receive Delay (receive clocks) 6
Transmit Gain Adjust (integer) 80
Receive Filter (Mhz) ○ 3.5 Mhz ● 2.5 Mhz
Receive Sample rate (MHz) 8.33 Receive sample clock divide ratio (integer) 12
Slice loop control ○ Enable Number Loops (0 = infinite) 1 ● Disable
Slice Repetition Period (ms) 1

PAT Configuration

Transmit Output Level ● 2 Vpp max (pulse or CW) ○ 150 Vpp max (pulse only, 20us max)
Channel 1 data source ○ Diagnostic ● Channel 1
Diagnostic source select ● Transmit Waveform ○ TGC Waveform
Maximum allowed transmit time (microseconds) 20
Receive monitor channel (integer from 1 - 24) 17
Sign extend data to 16 bits ○ Enable ● Disable
Receive Data Test Pattern (slice data = shot#) ○ Enable ● Disable
MUX enabled on Channel (integer from 1 - 24) 1 ☐ All ☐ None ☐ Multi TX
Shot definition ○ All shots identical ● Incrementing transmit elements ○ Manual shot definition
Transmit Waveform table No_xmt
XWF Divider 6 Sample rate (MHz) 16.67
Time Gain Control table constant 42db
TGC Divider 16 Sample rate (MHz) 6.25
Static Gain ● Same for all boards, all channels (hex) 0xff
○ Use table
Number of shots in a slice (integer) 100
Receive Data Length Per Channel (Currently in multiples of 64) 4096
Shot Interval Time (microseconds) 100000
Transmit Delay (transmit clocks) 0
Receive Delay (receive clocks) 2000
Transmit Gain Adjust (integer) 80
Receive Filter (Mhz) ○ 3.5 Mhz ● 2.5 Mhz
Receive Sample rate (MHz) 8.33 Receive sample clock divide ratio (integer) 12
Slice loop control ○ Enable Number Loops (0 = infinite) 1 ● Disable
Slice Repetition Period (ms) 1

Figure 20: Screenshot shows the important parameters that should be adjusted during UST (left) and PAT (right) imaging.

In **Table 2**, the parameters for the UST and PAT imaging are explained. With the current prototype, UST and PAT imaging tests cannot perform a multiple slices PAT scan due to a limitation in timing and synchronization between the UST engine and the pulsed laser. For this reason, in each experiment, the UST data of a targeted cross-section is acquired first after then PAT data. So, it is required to change the configuration in each test.

Table 2: The definition of the applied UST and PAT parameters.

Parameter	Definition	UST	PAT
Transmit Output Level	Applied voltage to the US elements	150 V	2 V
Transmit Waveforms table	Activate the transmit function in UST mode, and deactivate it in PAT mode	Final ring 4	No-xmt
Time Gain Control Table (TGC)	The gain for the transducer elements	20 dB	42 dB , 20 dB , 10 dB
Number of Shots in a Slice	Number of acquired data sets in the total acquisition time	256	Maximum 100
Receive data length per channel	The number of samples RF acquisition	1472	> 2000
Shot interval time	Total acquisition time per shot	1000 microseconds	100000 microseconds
Transmit Delay (Transmit clocks)	The delay required for the optimal UST signal transmission	16	Zero
Received Delay (Receive clocks)	The delay before recording data in UST and PAT	6	2000
Receive Filter (Mhz)	Low-pass filter for the data acquisition	2.5 MHz	2.5 MHz
Receive Sample Rate	Number of samples per second	8.33 MHz	8.33 MHz

2.4.3 The scanning unit

The scanning unit was developed in the lab and consists of three main parts: imaging tank, optical parts, and electromechanical components.

2.4.3.1 Imaging Tank

The (24” × 20”) clear acrylic water tank consists of items that are essential to complete the full-ring US/PA tomography test accurately. The imaging tank has two main parallel stages, which are placed in a horizontal position inside the tank, and the stages are controlled by four stepping motors located in the bottom of the tank. In this prototype, the top stage is responsible for positioning the scanned object (tissue-mimicking phantom) while the bottom stage is used to translate the ring US transducer. The motorized scanning system is controlled by using a custom-built program that allows for 1 mm minimum movement of each stage. To get proper illumination of the targeted cross-sectional slice, both stages must remain in a parallel position without any bending during tomographic scanning. To achieve precise illumination, each stage will be controlled by two vertically-oriented linear bearings that will be driven up and down by a screw mechanism from the two-stepping motors placed under the tank. It is important to mention that all components inside the water tank are made from materials that can resist the effects of the water environment (no corrosion).

Air bubbles in water medium have a negative effect on UST and PAT experiments because air bubbles create noise. For this reason, a separate water degassing system was made for the purpose of US/PA tomography imaging. The water fill, degassing, filtration, and drainage are controlled by using an associated pump and degas control method. The main principle of degassing is to pump the water inside a membrane contactor (SP-4x13 Series, 3M Liqui-Cel, USA) from one side and use a vacuum to suck the air bubbles from the other side. So, the flow of water, which is 10 L/min, is opposite the flow of air suction. There are 4 solenoid valves (SV) used to control the path of the water in all three scenarios, which are filling, more degassing, and draining (**Figure 21a**). In the filling operation, a distilled water enters the system from SV1 to the SV2 and then passes the water filter and degassing membrane to the tank. In this operation, the SV3 and SV4 are closed. To perform more degassing and filtration, the SV3 and SV2 are open, and then the water circulates from the scanning tank to the filter and degassing membrane. In the draining operation, the SV3 and SV4 are open, and then the water drains from the tank. It is important to mention that the water pump works in all three procedures while the vacuum works only at filling and more degassing procedures. **Figure 21b** shows a photograph of the degassing system; **Figure 21c** illustrates the control panel of the developed system. The water temperature is controlled by using heating elements with a thermostat to keep the temperature in the range between 25 to 37 ° C. In addition, there is a safety sensor to shut down water pumping to prevent water flood.

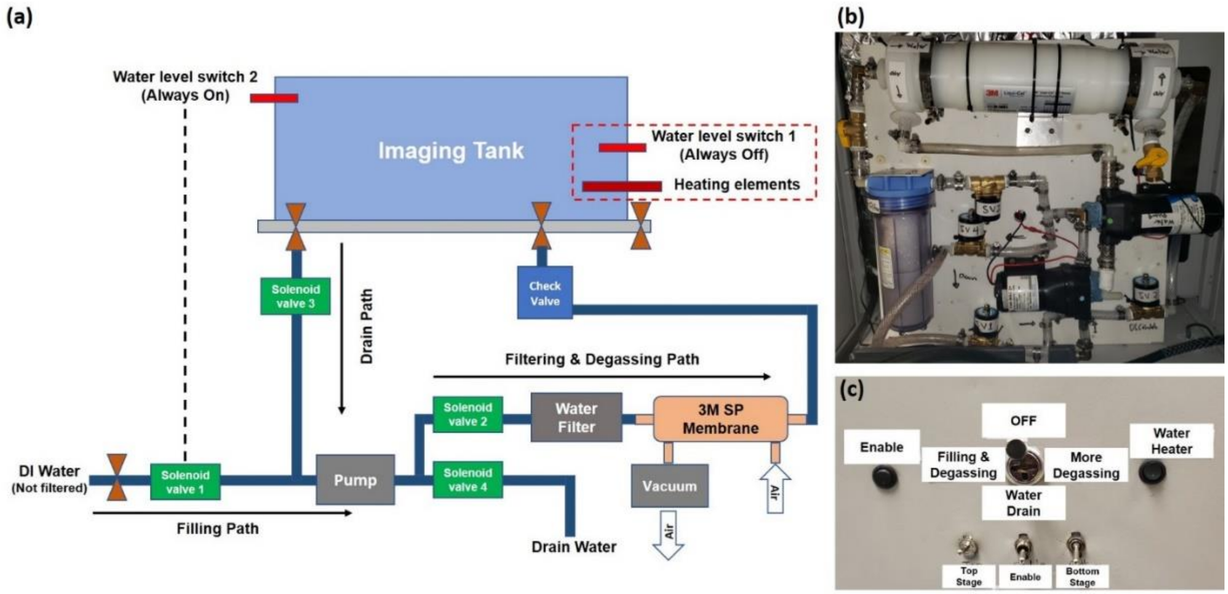

Figure 21: (a) Block diagram of the components of the degassing system in the US/PA tomography system (b) Photograph of the degassing system (c) Photograph of the control panel used to run the degassing system, water heater, top stage, and bottom stage.

2.4.3.2 Optical parts

The optical part that connects to the scanning tank consists of the cone-shaped reflector (68-791, Edmund Optics, New Jersey, USA), large scale parabolic reflector (P19-0300, Optiforms Inc, California, USA), and 5mm thickness optical window made of H-K9L glass. By positioning the cone mirror in the path of the laser beam, which reflected from the protected silver 45-degree mirror, it creates a disc-shaped laser beam directed to the parabolic reflector. After that, the parabolic reflector will create a large base, hollow, cone-shaped beam with a 53-degree angle that could be used in full-ring illumination (**Figure 22a**). Since the position of the ring beam is fixed (not adjustable) by the cone and parabolic mirrors, the ring location was adjusted by translating the scanned object in the vertical direction, so in this prototype, the object moves to adjust the position of the ring beam (**Figure 22b**).

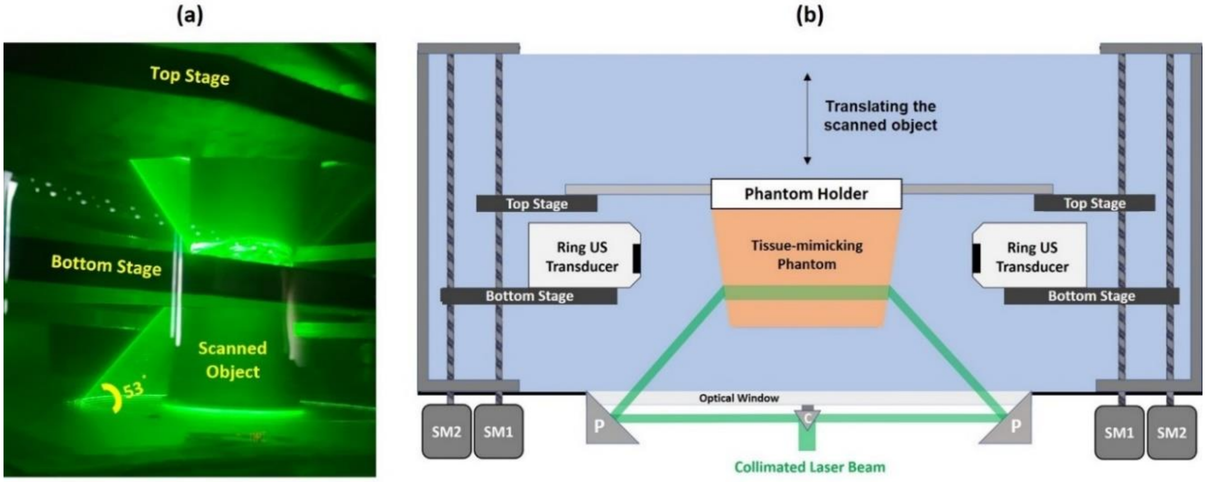

Figure 22: (a) Photograph of the cone-shaped beam created by the large parabolic reflector (b) The 2-D graph shows the path of the collimated beam to create a full-ring beam. The parabolic reflector “P”, cone-shaped reflector “C”, and stepping motors “SM” are shown in the graph.

Energy loss is expected in the optical system due to the different optical reflectance of the different coated materials. In this prototype, the coating material of the cone-shaped and parabolic reflectors are protected aluminum while the 45-degree mirror is protected silver. By using the reflectance data of each optical component, which are provided by the manufacturer, the transmitted energy was calculated. The maximum energy loss is about 50%, which occurred at 840 nm wavelength, while 532 nm has the maximum transmitted energy, which is about 75% (**Figure 23**). It is important to mention that the transmitted energy is calculated, and it is based on ideal condition and may not represent the actual measured energy during experiments.

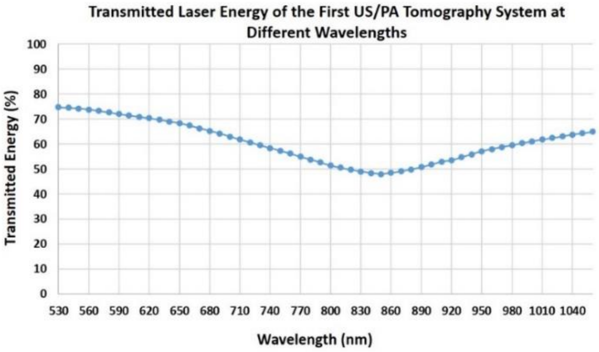

Figure 23: Estimated percentage of the transmitted laser energy calculated by using the transmittance and reflectance data sheets of each optical component in the omnidirectional full-ring US/PA tomography system (first prototype).

2.4.4 Electromechanical components

In this prototype, modified electrical circuits were designed and used to control the degassing system, water heater, sensors, and the stepping motors to move stages. **Figure 24** shows the block diagram and pictures of the electrical circuits that mainly use 12V electric relays to control the operation. In the degassing and heating system, there are four relays with four On/Off switches; each relay is used to run one specific function (**Figure 24a**). The first relay (Relay 1) is responsible for filling and degassing the water that comes from the water source. This relay is connected to the water pump, vacuum, solenoid valve 1, and solenoid valve 2. In addition, there is a floating water sensor that shuts down this function to prevent waterflood. The second relay is responsible for the extra degassing function which needs the same parts in relay 1 except solenoid valve 1 is substituted for solenoid valve 3. The draining function is operated by the third relay which runs the water pump, solenoid valve 3, and solenoid valve 4. The fourth relay is connected to the 110 V heating element which has a thermostat sensor placed inside the water tank. Because the heating elements should work in a water medium, there is a floating water sensor between switch 4 and the relay so the relay cannot work until the water covers the heating element.

Because the current UST prototype system has its built-in software that controls all scanning and motors function, it was essential to keep the same stepping motor driver and use it to control the new stepping motors which are responsible for translating top and bottom stages. To achieve that, the second electrical circuit consisted of two relays built to connect the driver and stepping motors, so each relay is responsible for one stage (**Figure 24c)**. Manual On/Off switches are used to shift between the top and bottom stage. The control panel that contains all switches was shown earlier in **Figure 21c**.

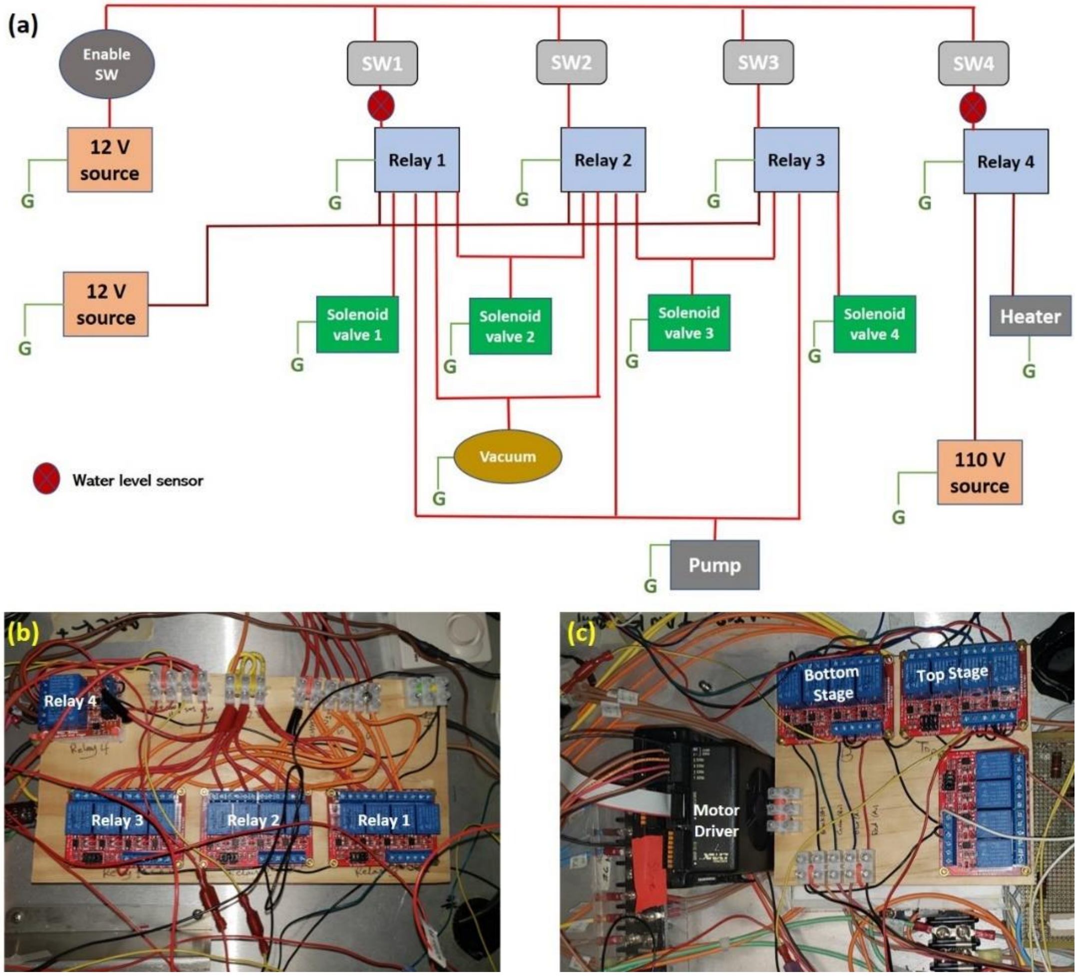

Figure 24: (a) Block diagram of the electric circuit of the degassing and heating system of the omnidirectional US/PA tomography system (b) The photograph shows electric circuit of the degassing and heating system (c) Photograph of the electric circuit of the stepping motors that control top and bottom stages. The motor driver is seen in the photo.

2.4.5 Timing and synchronization

With most UST/PAT systems, the tunable laser source is used as the master clock to control the UST engine during PAT imaging. However, in the current prototype, this is not possible because the UST cannot receive an external trigger (from the laser source). This fundamental problem tackled by driving a trigger signal from the first UST data processing board to trigger the laser. The first PC board in the UST engine is responsible for the first 24 elements of the ring US transducer. For this reason, this signal indicates the starting acquisition time in the ring US transducer during PAT imaging (receiving mode). The main issue with this weak signal is that it is a 40 ns signal which cannot be detected by the laser source which needs a stable 100 µs signal (10 Hz) for triggering. For this reason, a function generator (33220A, Agilent, California, USA) is utilized to remodel the 40 ns signal to a 100 microsecond, 5 V amplitude signal which makes it compatible for the pulsed laser as shown in **Figure 25**. A BNC cable was used to transfer the signal from the UST system to the external trigger port of the function generator. Using the Burst mode in the function generator, a 5V, 100 µs output signal is generated and transmitted to the external trigger port of the pulsed laser. The laser can run once it detects the trigger signals from the function generator, but it will stop generating laser pulses once the triggering signal stops for 500 ms.

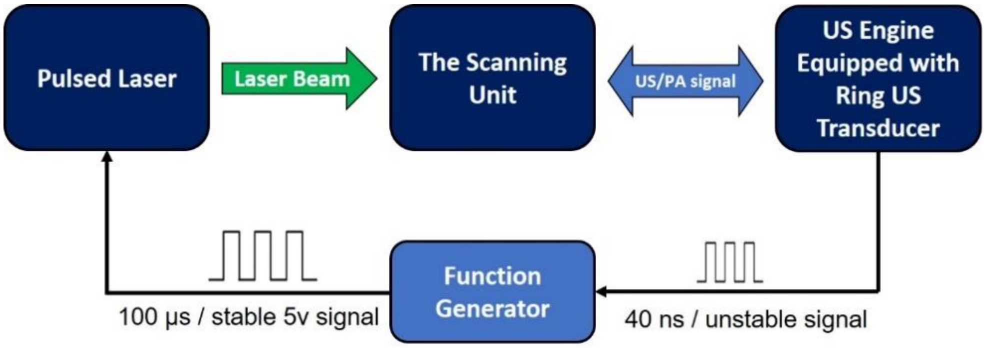

Figure 25: Block diagram of the method used to synchronize the UST engine and the laser source.

The second major problem was caused by the initial built-in laser flash lamp warmup time. The laser required a 10 seconds warm-up time before it starts firing a beam. At the same time, the maximum acquisition time for the UST system is 10 seconds, which meant that by the time the laser started firing, the UST engine had stopped acquiring data. This problem was solved by the laser company after changing the safety configuration of the laser, so the countdown time reduced from 10 seconds to 8.6 seconds. This will give 1.4 seconds to illuminate the sample with 14 shots (in the ideal condition) to obtain 14 data sets for the targeted cross-sectional slice. Because the UST engine and the pulsed laser run from two separate on/off switches, there is a possible delay from the user beginning of the synchronization. For this reason, we get less than

14 data sets from the 14 laser shots, so typically we used the last 10 RF data sets to reconstruct the PAT image (**Figure 26**).

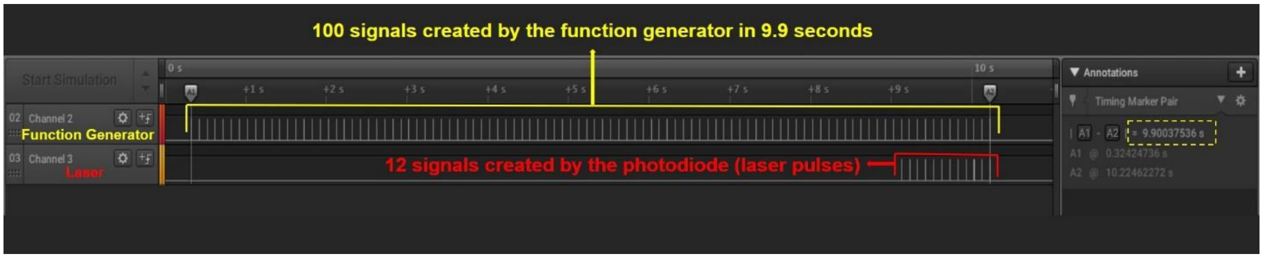

Figure 26: Screen capture shows the electrical pulses generated from the function generator (yellow) and the laser (red) in 10 seconds period.

The delay time between the function generator and the laser pulse was measured at 100% laser energy, and the measured delay time was 316.4 µs (**Figure 27**). This time may change based on the set laser energy due to the increase in Q-switch delay at low energy levels. In general, after each laser shot, there is enough time to acquire the data before the next shot.

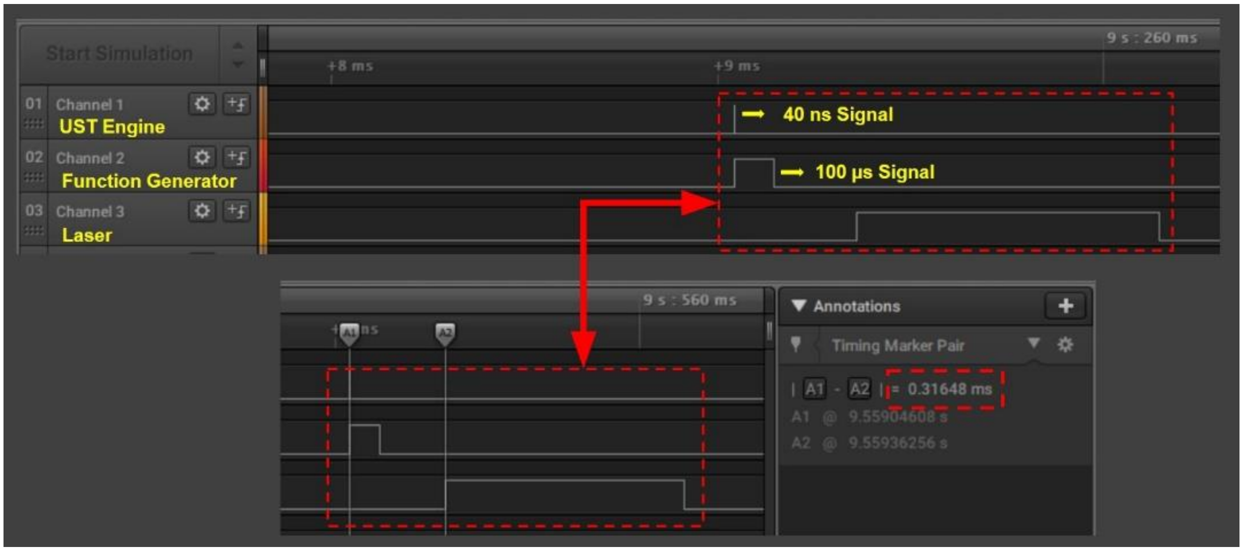

Figure 27: Two screen captures show all three pulses created by the UST engine, function generator, and the laser. The delay time between the function generator (A1) and the laser pulse (A2) is 316.4 µs.

CHAPTER 3 - ALL-REFLECTIVE RING ILLUMINATION SYSTEM FOR PHOTOACOUSTIC TOMOGRAPHY

3.1 Introduction

In this chapter, three different experiments, using a full-ring illumination method, will be discussed. In the first two experiments, a ring illumination source was used with a linear US transducer to study the efficiency of full-ring illumination in tissue-mimicking phantoms. In the final experiment, the first prototype of the omnidirectional US/PA tomography system was used to image a tissue-mimicking phantom. The data generated using the system is presented with an eye towards laying the groundwork for a future three-mirror system with near-normal tissue illumination and even greater imaging depth. The results of this chapter have been published in the Journal of Biomedical Optics (SPIE) in May 2019 [100].

3.2 Material and Methods

3.2.1 Development and validation of ring-illumination optical system with linear-array acquisition

The performance of the ring illumination mode was evaluated with regards to the PA imaging depth using two tissue-mimicking phantoms made of 10% porcine gelatin (G2500, SIGMA-ALDRICH, Missouri, USA) and 0.2% cellulose (S5504, SIGMA-ALDRICH, Missouri, USA). For the first experiment, a 700 µm diameter graphite absorber was inserted obliquely into a gelatin phantom, and the PA signal was measured with respect to the horizontal depth (**Figure 28a**). The illumination source for the experiment was a pulsed 532 nm, Nd:YAG, 8 ns laser (Quanta-Ray Pro 270, Spectra-physics, California, USA) with an output of 10 mJ per pulse. A 100 mm diameter parabolic mirror (45-944, Edmund Optics, New Jersey, USA) and cone-shaped reflector (68-791, Edmund Optics, New Jersey, USA) were used to create the ring beam by adjusting the distance between the cone mirror and the parabolic ring reflector (**Figure 28b**). For the second experiment, a 70 mm diameter gelatin phantom containing two graphite absorbers with 500 µm diameters were placed in two planes (**Figure 28c**) and imaged to determine the maximum imaging depth and the plane selectivity of the full-ring illumination method. Large scale parabolic reflector (P19-0300, Optiforms Inc, California, USA) with 243 mm diameter was utilized with a cone-shaped reflector to create a large ring-shaped beam with 4 mm thickness. A 532 nm laser source (PhocusCore, Optotek, California, USA) was used, resulting in 4.77 mJ/cm^2 fluence in the targeted cross-sectional area. In this experiment, it was not possible to adjust the position of the ring beam, so the beam was 17 mm below the targeted cross-sectional area (**Figure 28c**). In both experiments, a programmable US scanner (Vantage 128, Verasonics Inc., Washington, USA) was utilized with an L11-4 linear array transducer, operating at 8.4 MHz center frequency, for US and PA signal acquisition.

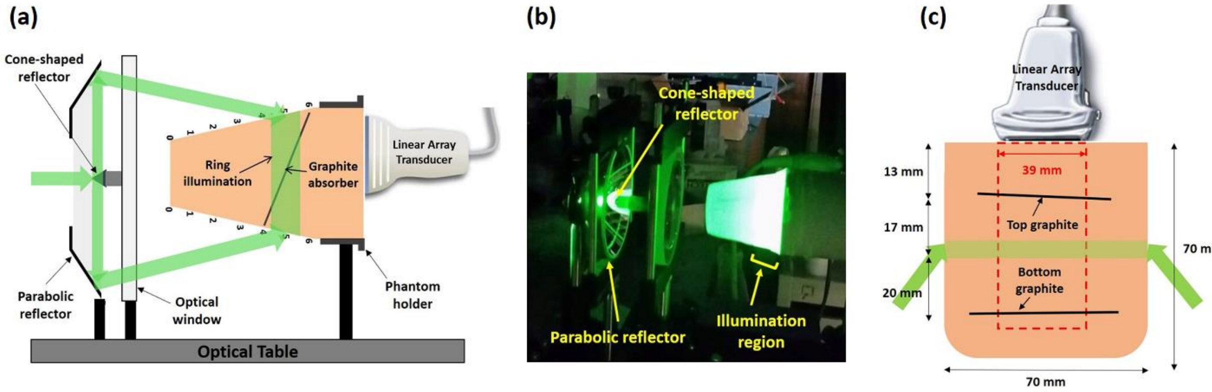

Figure 28: (a) Experimental setup of the breast phantom embedded with a diagonal graphite absorber, and (b) the photograph of the same experimental setup. (c) Diagram showing the dimensions of the tissue-mimicking phantom used for the second experiment. The US scanning area is enclosed in the red dashed lines, and the ring beam positioned 17 mm below the targeted cross-section.

3.2.2 Photoacoustic tomography using full-ring illumination and ring-shaped transducer

The full ring US transducer and illumination system, shown in **Figure 29a**, also used a gelatin phantom for system characterization. In this experiment, an 89 mJ/pulse laser source (PhocusCore, Optotek, California, USA) was expanded to a ring shape resulting in 4.7 mJ/cm^2 of fluence at 532 nm. The ring US transducer has a 200 mm inner diameter and is comprised of 256 elements, with an element pitch of 2.45 mm and a height of 9 mm. In PAT mode, the scattered signals are recorded by all 256 elements at a sampling rate of 8.33 MHz. The 243 mm diameter parabolic reflector and the cone-shaped reflector were used to create the ring-shaped beam with 4 mm thickness on the phantom surface. The phantom used for this experiment was a 7.5 cm in diameter and made of 12% porcine skin gelatin (G2500, SIGMA-ALDRICH, Missouri, USA) mixed with 0.4% cellulose (S5504, SIGMA-ALDRICH, Missouri, USA). Three graphite rods, with 2 mm thickness, were placed horizontally inside the phantom in three layers (**Figure 29b**). The ring beam was adjusted on each cross-sectional slice by translating the phantom in the vertical direction. The results from this experiment demonstrate the uniqueness of the all-reflective PAT system in creating co-registered PA/US tomographic images with significant depth and will be discussed further in the results section.

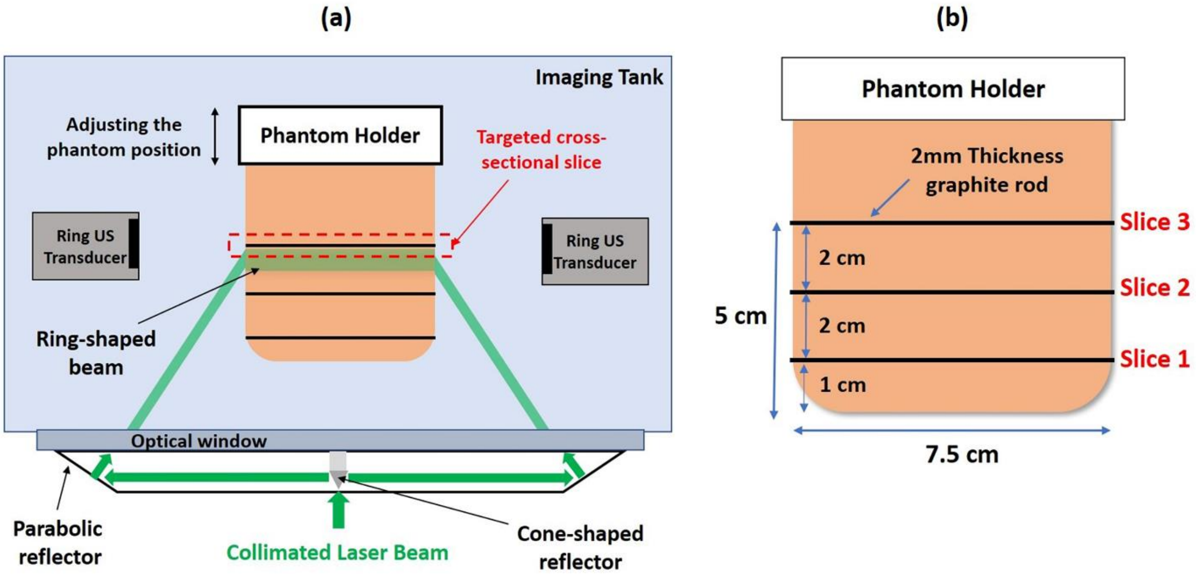

Figure 29: (a) The setup for the full-ring illumination and full ring acquisition experiments. The cone-shaped mirror and the parabolic reflector create the ring-shaped beam for the scanned cross-section. The ring beam was positioned 10 mm below targeted cross-sectional slice for the discussed experiments (b) The diagram shows the dimension of the tissue-mimicking phantom and the position of the graphite rods from the bottom slice (Slice 1) to the top slice (Slice 3).

3.3 Results and Discussion

3.3.1 Photoacoustic results using full-ring illumination with a linear array transducer

Figure 30 plots the PA image for the diagonal graphite absorber in gelatin for the experimental setup shown in **Figure 28a**. A clear PA signal was detected within the field of view of the linear array US transducer, and a depth of 25 mm inside the phantom was imaged. As anticipated, the PA signal intensity was the largest superficially and was attenuated with horizontal depth (**Figure 30a**) due to absorption and scattering. The normalized PA amplitude versus horizontal depth for this image was plotted in **Figure 30b**, demonstrating the depth dependence of the fluence and the relative uniformity of the PA signal within the middle portion of the phantom. The uniform PA signal between the 10 to 20 mm underscores the effectiveness of omnidirectional ring illumination in providing a uniform fluence map within a targeted cross-section. In an ideal PA platform, the fluence is depth independent, and the proposed ring illumination system can enhance the PAT imaging by providing a more uniform illumination map. The PA signal after 25 mm disappears as the angled optical absorber moves outside of the selected illuminated cross-sectional area.

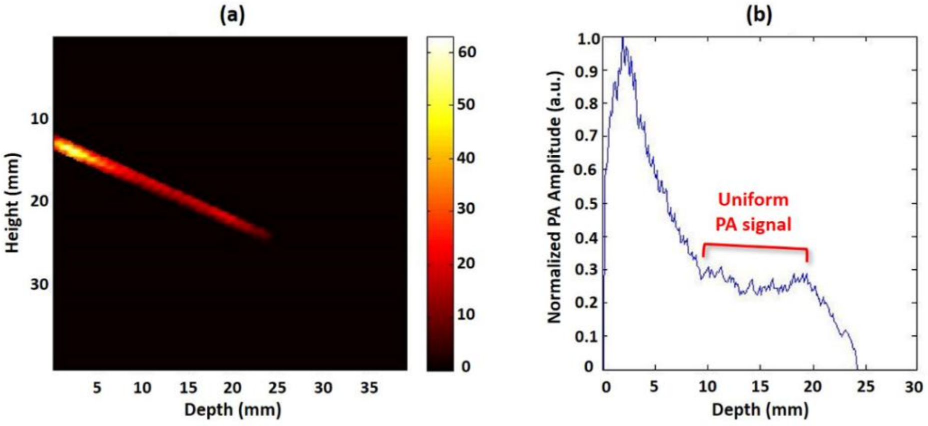

Figure 30: (a) The PA signal distribution across the illuminated cross-section slice of the gelatin phantom. (b) The graph demonstrations a normalized PA amplitude versus depth. A uniform PA signal amplitude is seen between the depths of 10 to 20 mm

Figure 31 plots the results from the second experiment, which used two graphite absorbers in separate planes, as shown in **Figure 28c**. Since the linear array transducer has a limited field of view, only a section of the horizontal graphite absorber is shown (**Figure 31a**). As anticipated, both objects can be seen in US image, while in the PA image, the targeted layer shows a high PA signal which demonstrates the selectivity of the full-ring illumination mode in imaging a targeted cross-sectional slice. The full-ring illumination was also able to deliver sufficient energy to the core of 70 mm tissue-mimicking phantom (**Figure 31b**). This finding highlights the benefit of the ring-illumination system, which allows for a lower fluence and a greater cross-sectional illumination depth. The limited field of view of the linear transducer used in these experiments would also not be a problem for the full-ring US transducer, where all objects would be visualized regardless of location.

It is important to mention that there was an observed PA signal from the middle layer of the phantom (at a depth of 30 mm) which happen due to two reasons. First, the phantom was created in two parts by initially pouring the first layer and then allowing it to set so it could support the graphite rod, after which a second layer of the same material was poured to finish the phantom. The setting process of the first layer and the possible settling of the cellulose scattering material could have created the PA signal seen at the interface. The second reason is related to the incident position of the ring beam on the interface surface between two layers of gelatin phantom, which is located at 20 mm above the bottom graphite.

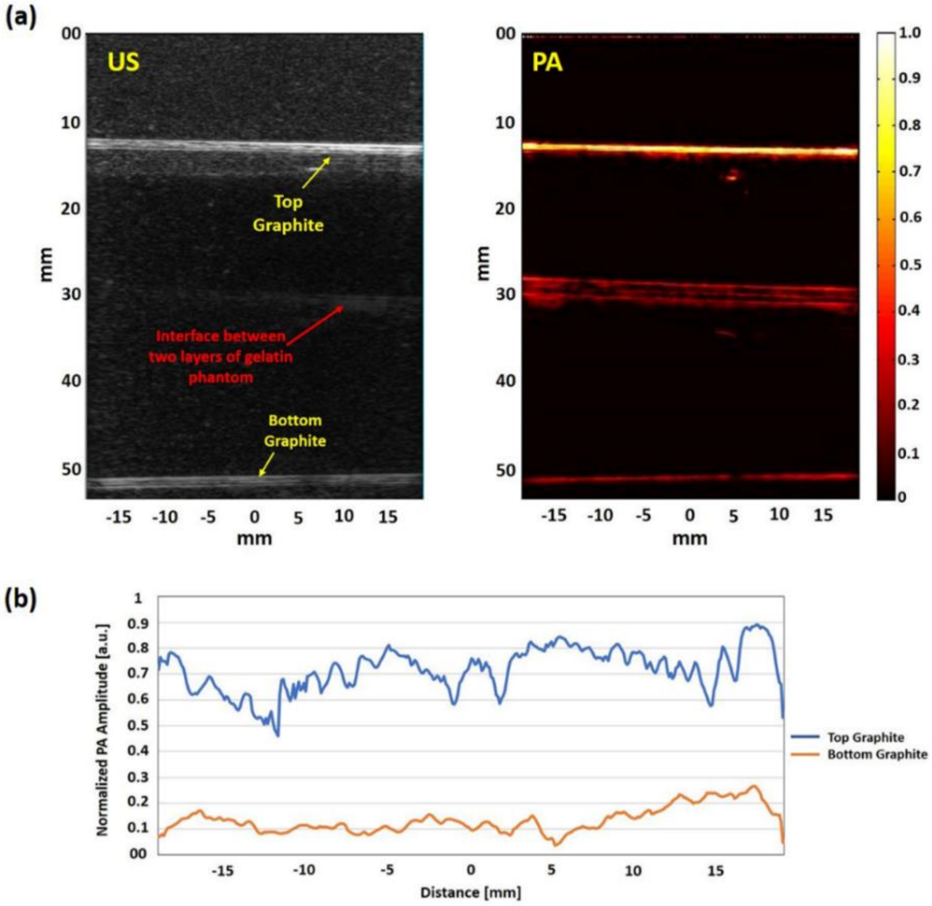

Figure 31: (a) The US image (left) showing the graphite absorbers in two different planes. The interface seen in the picture is an artifact from the phantom making process. The PA image (right) is showing the top and the bottom graphite absorbers, with a more visible top object. (b) The plot of the normalized PA signal amplitude across the top and bottom graphite absorber. The targeted, top graphite absorber has a larger PA signal amplitude.

3.3.2 Large-scale omnidirectional illumination for full-ring photoacoustic tomography experiment

Figure 32 shows the UST and PAT images for the full-ring tomography system shown in **Figure 29b**. The UST images were reconstructed using the waveform method [101], and PAT images were reconstructed using the back-projection method [102]. For the back-projection reconstruction, the RF signals received at each transducer across multiple acquisitions of the same slice were averaged together to increase the signal-to-noise ratio (SNR). In **Figure 32**, the top and bottom cross-sectional slices, which are separated by 4 cm of gelatin, are shown. In general, the results demonstrate the vertical depth independent imaging capability of the full ring illumination system utilizing a ring US transducer.

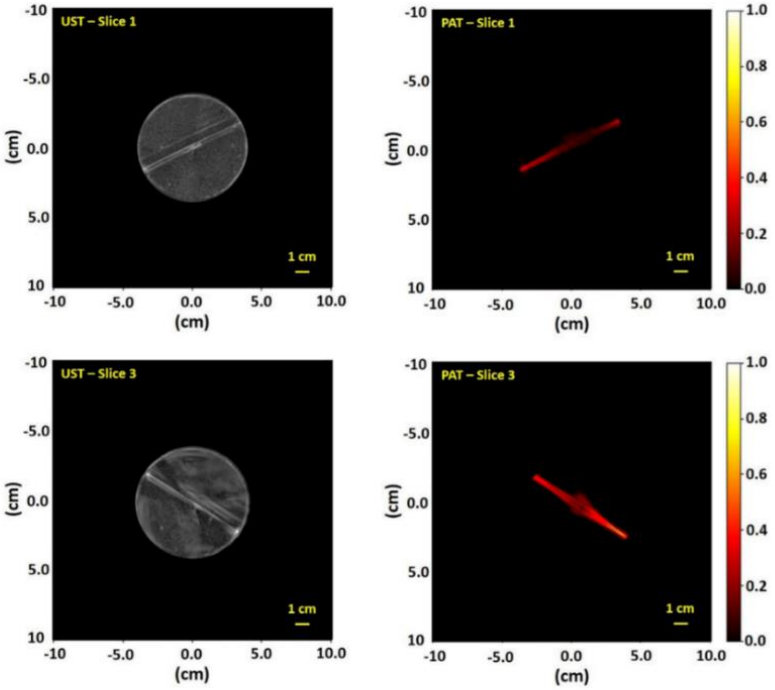

Figure 32: UST (left), PAT (right) images of slices 1 and 3, showing the 8 cm graphite absorber in the tissue-mimicking phantom. The full-ring illumination was able to visualize the whole objects in all slices.

The normalized PA amplitude as a function of the horizontal depth for the three different cross-sections is shown in **Figure 33**. As anticipated, all three slices showed a high PA signal close to the outer surface, and the signal degraded slightly as the horizontal depth increase. In general, the results once again show the deposited energy uniformity within the phantom irrespective of vertical imaging depth.

To increase the fluence in the central part of the scanned slice, it is important to improve the incident angle of the ring beam and the incident location of the ring beam with respect to the targeted cross-sectional area. In the previous experiment, the ring beam was positioned 10 mm below the targeted cross-sectional slice. Future works will examine the effects of target illumination as a function of beam position below a cross-sectional area and the resulting PA image quality.

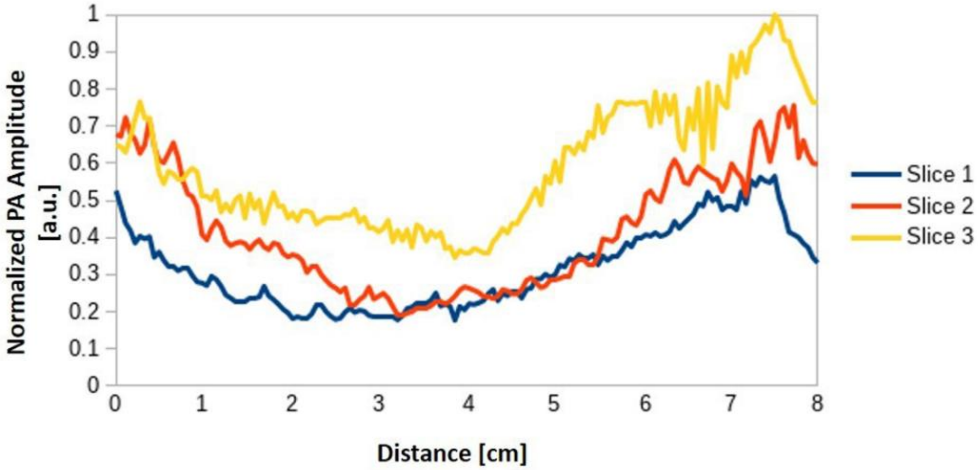

Figure 33: Normalized PA amplitude across the 8 cm graphite object for all three cross-sectional slices demonstrating the uniformity of the PA signal across the targeted cross-sectional slice.

3.3.3 Future work: an optimal, adjustable, all-reflective, full-ring illumination photoacoustic tomography system

For the full-ring illumination and US transducer system, the single cone mirror and parabolic reflector imaging system was able to create a ringed beam with a 39^o angle with respect to the phantom surface. To improve the efficiency of the illumination, it is important to enhance the incident angle of the ring beam. The proposed three-mirror system (**Figure 34**) will have a tissue incidence angle of 66 degrees with respect to the object surface, as opposed to 90-degrees or normal incidence, which is anticipated to improve the PAT results. This system consists of a cone-shaped reflector and two conical reflectors which can be adjusted independently for scanning the length of a cylindrical object. As shown in **Figure 34**, the collimated beam from the laser source is directed normally to the cone-shaped reflector, and upon reflection, a circular beam is directed towards the stationary conical ring reflector. The stationary conical ring reflector then transmits the cylindrical-shaped beam to the mobile conical mirror which focuses the beam onto the targeted slice of the object. The cone-shaped reflector and the first stationary mirror are external to the water tank that houses the second mobile mirror and the ring US transducer.

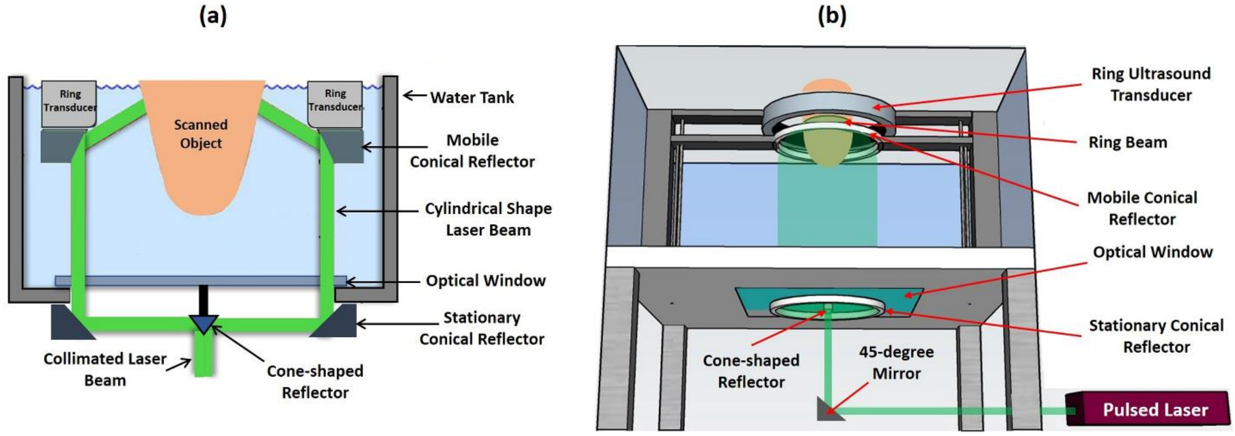

Figure 34: (a) Cross-sectional view of the all-reflective, full-ring illumination, and full-ring US transducer system, with three reflective elements in the imaging tank. (b) Three-dimensional view of the system showing a ring US-transducer, a pulsed laser, a cone-shaped reflector, and two conical reflectors.

During the scanning, the mobile conical reflector moves synchronously with the ring US transducer. Since the mobile reflector is placed below the transducer level, the breast tissue coverage will be identical to UST and imaging areas close to the chest wall is feasible. The size and profile of the breast are defined by the UST images which will be used to find the optimal position of the mobile reflector and adjust it to match the illumination and the acoustic acquisition planes. The design was verified by using ray tracing, which showed that it could illuminate breast tissue with 140 mm in diameter.

3.4 Conclusions

Multiple, proof of concept experiments using mirror-based, full ring illumination systems were presented in this work for PAT imaging. A diagonal graphite absorber in gelatin and planar graphite absorbers were used to demonstrate uniformity of illumination system irrespective of vertical imaging depth. These experiments were followed by a full ring illumination and full ring US transducer system, which again demonstrated the energy uniformity within the phantom even with a non-optimal 39^o illumination angle. Lastly, a proposed three-reflector, ring illumination US/PA tomographic system was presented with a 66^o illumination angle, which promises exciting future results for medical diagnosis due to its practicality of design and ease of scalability. All of the presented setups achieve a low fluence due to their inherent ring design and will no doubt benefit patients and clinicians in future imaging and diagnostic needs.

CHAPTER 4 - PHOTOACOUSTIC TOMOGRAPHY WITH A RING ULTRASOUND TRANSDUCER: A COMPARATIVE STUDY ON DIFFERENT ILLUMINATION STRATEGIES

4.1 Introduction

In this chapter, three different illumination methodologies for PAT imaging: full-ring, diffuse, and point illuminations, are compared (**Figure 35**). Point or diffuse illuminations are suitable for imaging cross-sections close to the point of light entry and the given fluence drops with light propagating through the tissue towards higher vertical depths. Using new findings from the three methods, it aims to show that the full-ring illumination is the most effective method for creating PAT images due to its inherent cross-sectional fluence uniformity across vertical imaging depths. This is especially important for breast cancer screening when imaging close to the chest wall can be difficult. The three illumination methods are compared by imaging a three-layer polyvinyl chloride (PVC) tissue-mimicking phantom to gauge the advantages and disadvantages of common PAT imaging techniques. The experiments presented in this chapter also all use the same data acquisition system and settings. Comparisons are made between normalized PAT amplitudes for each cross-section and illumination methodology. Furthermore, the optimum position of the ring beam, with respect to the targeted cross-section is examined. The results of this chapter have been published in Applied Sciences Journal in July 2019 [103].

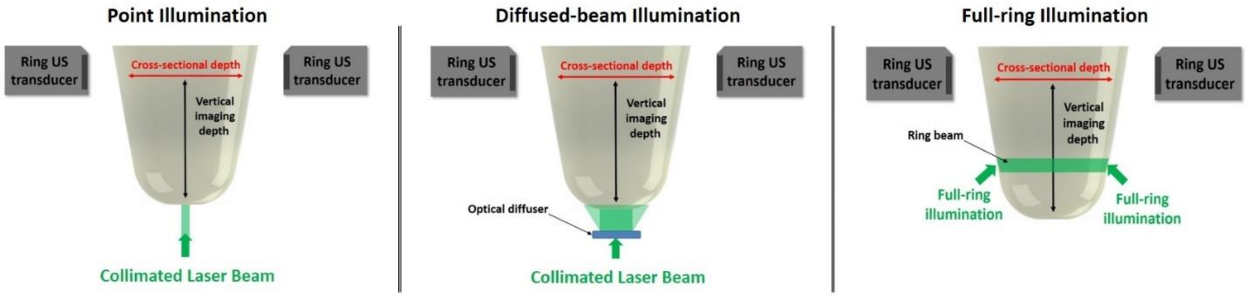

Figure 35: The three methods of illumination for PAT imaging that are compared in this study, with the definitions of vertical and cross-sectional imaging depths.

4.2 Material and Methods

4.2.1 UST/PAT acquisition system

A 200 mm diameter, 256 element ring US transducer (Barbara Ann Karmanos Cancer Institute, Detroit, USA) with a center frequency of 2 MHz and bandwidth is 60% was used for all data acquisition. The presented system has a measured lateral resolution of 1 mm as determined by measuring a 200-micrometer light-absorbing string. This transducer has an element pitch of 2.45 mm and a height of 9 mm. The scattered US waves from a PA imaging event are recorded by all 256 elements using a sampling frequency of 8.33 MHz. As shown in **Figure 36a**, the US ring transducer is housed in an acrylic tank and is supplied with degassed, distilled water. During PAT imaging the ring US transducer uses a 10 dB linear, time gain compensation (TGC) for acquiring the data, which is designed to optimize the signal-to-noise ratio (SNR) for the given phantom.

4.2.2 Laser source and light illumination schemes

A tunable, 10 ns pulsed laser (Phocus Core, Optotek, California, USA) is used for all PAT imaging experiments. The laser generates around 100 mJ per pulse at 532 nm. In the full-ring illumination mode, a large parabolic reflector (P19-0300, Optiforms Inc, California, USA) is used with a 10 mm diameter cone mirror (68-791, Edmund Optics, New Jersey, USA) to create the 4 mm ring-shaped beam on the phantom surface (**Figure 36a**). Since the beam position is stationary, neither the cone mirror nor parabolic reflector is mobile. The ring location is adjusted across each cross-section by translating the phantom in the vertical direction (**Figure 36b**). For the diffused-beam experiments, a 120 grit ground glass diffuser (DG10-120, Thorlabs Inc, New Jersey, USA) is placed in the laser light path inside the water tank after removing the cone mirror (**Figure 36c**). Finally, point illumination only uses the 45-degree mirror for directing the laser beam onto the phantom (**Figure 36d**).

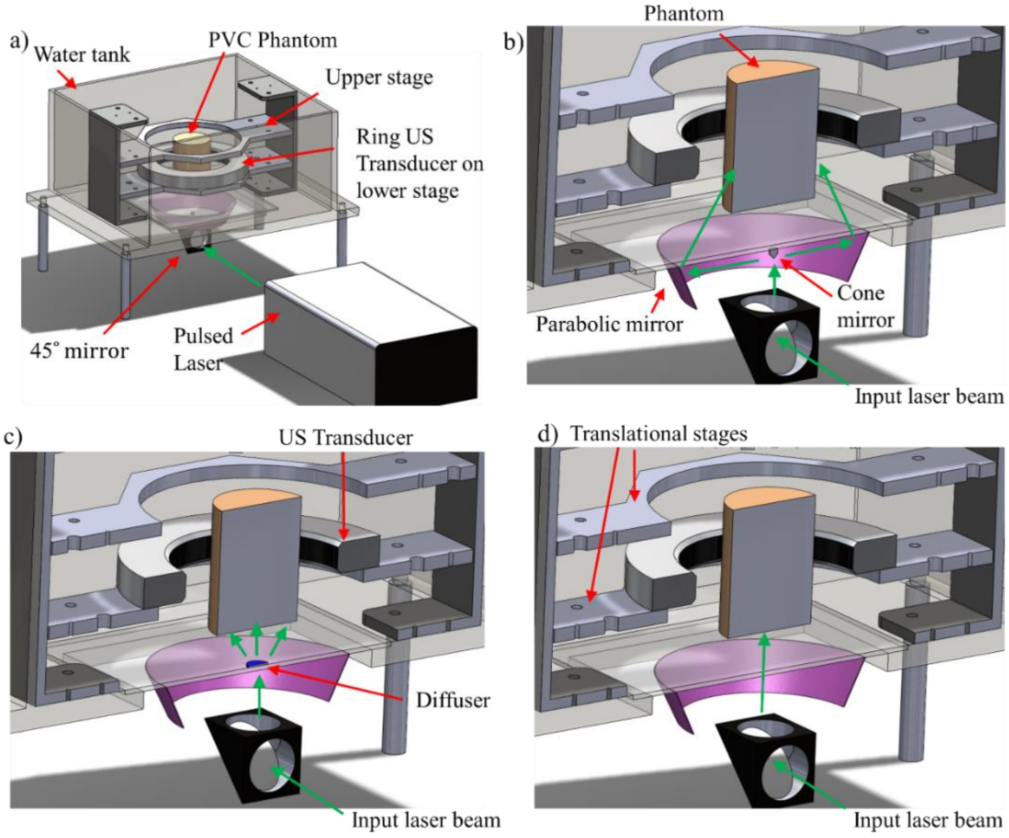

Figure 36: (a) PAT experimental setup showing the water tank, ring US transducer, and the translational stages. The experimental setups for the (b) full ring, (c) diffuse-beam, and (d) point illumination of the phantom.

4.2.3 Tissue-mimicking phantoms

The performance of the three different illumination methods was evaluated with regards to the PA imaging depth using a phantom made of polyvinyl chloride (PVC) (M-F Manufacturing Super Soft, USA), with 0.2% fine ground silica (US Silica MIN-U-SIL5) used as an optical diffuser. To create a PVC phantom [104], the plastisol was first mixed with the ground silica and then heated in a microwave to 170° C. In a mold, three graphite rods with 2 mm diameter were placed horizontally, and the PVC was poured to create the three layers, as shown in **Figure 37**. After cooling, the phantom was removed from the mold and used for the experiments described. Graphite was chosen as an absorber due to its broadband absorption characteristics and ease of placement inside the phantom.

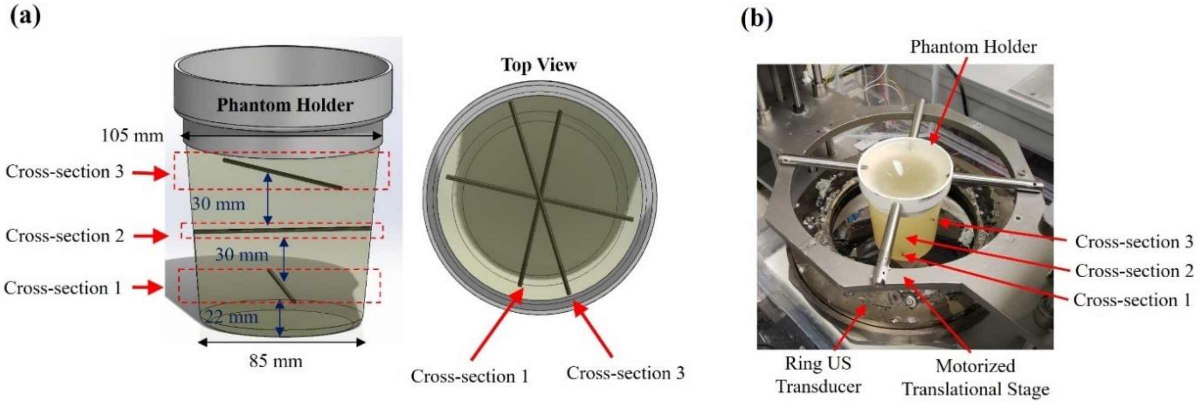

Figure 37: (a) Graph illustrates the PVC phantom and graphite inclusions and their dimensions. (b) A photograph of the experimental setup including the ring US transducer. A motorized translational stage was used to adjust the position of the phantom to acquired images at multiple cross-sections.

4.2.4 UST and PAT image reconstruction

In all instance, the waveform method was used to reconstruct the UST images [101], while filtered back-projection was utilized to reconstruct the PAT images [102]. For PAT back-projection reconstruction, the RF (radio frequency) values for each cross-section were averaged 10 times to increase the overall SNR. In UST mode, a 20 dB linear gain TGC was used for acquiring the US images, while in PAT mode, as previously described, a linear 10 dB TGC was used for data acquisition. For US imaging, the used TGC was optimized to minimize the transducer saturation, which resulted in cleaner images. This was done empirically. For PAT imaging, the value chosen was designed to reduce the signal emanating from other cross-sections from appearing in the cross-section of interest.

4.3 Results and Discussion

4.3.1 A comparison of the three different illumination methods

The results discussed in this section focus on analyzing the PAT images and PA signal amplitudes from progressively deeper phantom cross-sections using the discussed illumination methodologies. **Figure 38** shows the UST and PAT images for the first and third cross-sections, which are separated by 60 mm. The PAT images are masked based on the region of interest (ROI) as determined by the UST image. For each illumination method, the PA amplitude is normalized to the highest value for the method across all cross-sections. For example, for the full-ring illumination method, images were normalized to the highest amplitude of PA detected within the three slices, which are separated by 30 mm each. This allows for visualization of the effect of depth on the PA signal amplitudes for each illumination method. As can be seen in the PAT images, the graphite absorber is visible in the first and third layers (i.e., larger vertical depth) of the full-ring illumination method, which is not the case for the diffuse and point-source methods.

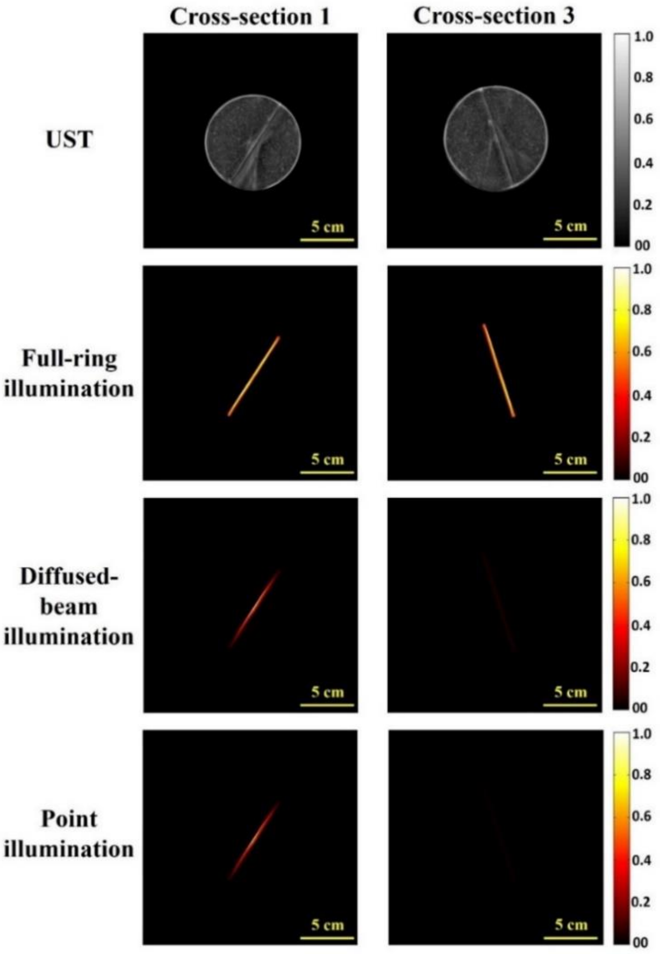

Figure 38: UST and normalized PAT images of the PVC phantom with graphite absorber using the three different illumination techniques for cross-sections 1 and 3.

To further quantify the results shown in **Figure 38**, the PA signal amplitude across the graphite absorber for each illumination method, and for each cross-section, is plotted in **Figure 39**. For the full-ring illumination method, the PA values are nearly constant across the three cross-sections (**Figure 39a**). However, the peak amplitude value of the PA signal decreases by 25 times for point-source illumination and 15 times for the diffused-beam illumination between the first and third cross-sections. As seen by the uniformity in the amplitudes between three cross-sections for the full-ring illumination method, this imaging technique can provide a consistent image regardless of vertical depth. On the other hand, the diffused (**Figure 39b**) and point illumination (**Figure 39c**) methodologies show variance in PA amplitude signals. This finding demonstrates that the full-ring illumination is capable of providing sufficient fluences at lower vertical depths, which results in detectable and reliable PAT images across cross-sections.

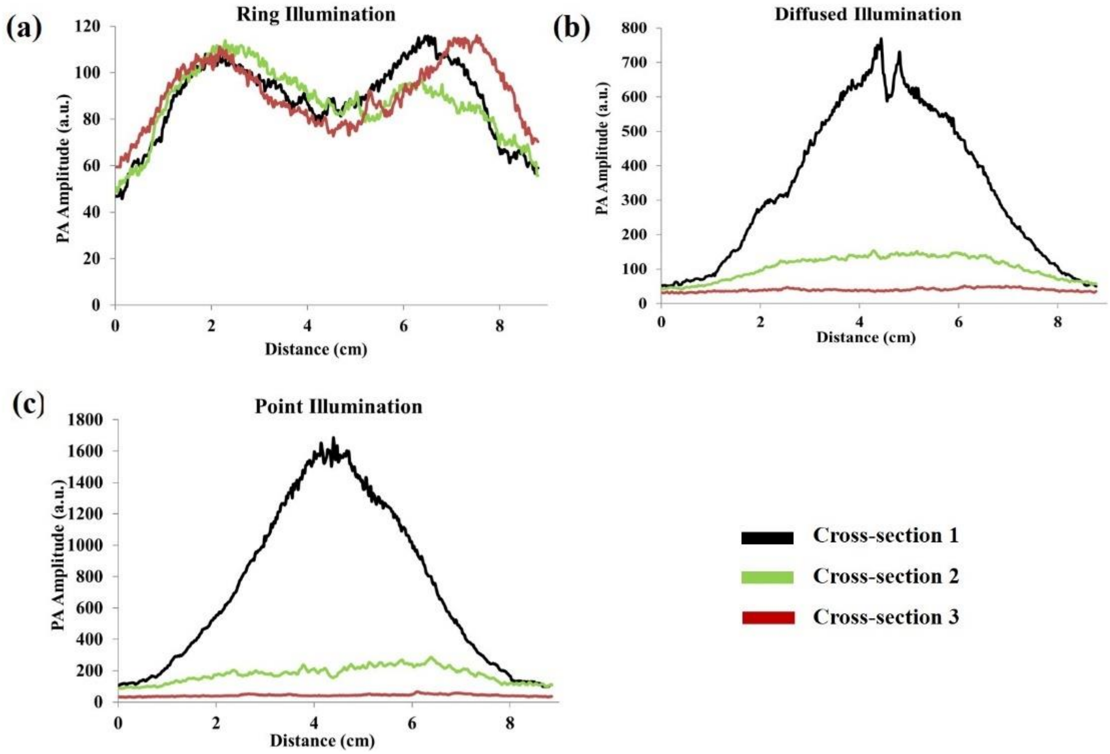

Figure 39: PA amplitude across the graphite absorber for three different cross-sections for (a) full-ring, (b) diffused-beam, and (c) point illumination.

To further compare the performance of the three illumination strategies, the SNR and contrast to noise ratio (CNR) of the PAT images are measured. In the SNR, the value is calculated by:

$$SNR = 20 \times log10\,(\frac{M_S}{M_B}) \tag{4.1}$$

where M_S refers to the mean of the PA signal, as marked by the US image ROI, while M_B refers to the mean of phantom background. The CNR is determined by:

$$CNR = 20 \times log10\,(\frac{M_S - M_B}{\sigma_B}) \tag{4.2}$$

where Ms refers to the mean of the PA signal, M_B refers to the mean of phantom background, and σ_B is the standard deviation of the phantom background. For the full-ring illumination method, the PA amplitude values used are from irradiating the target cross-section 15 mm below the cross-section of interest, as shown in **Figure 41a**. As can be seen in **Figure 40 a** and **b**, the SNR and CNR are nearly constant for the full-ring illumination across the three cross-sections, which is not the case for diffuse and point illuminations. **Figure 40c** also plots the PA amplitudes across the graphite object at the third cross-section for all illumination methods. Based on the laser beam diameter of 8 mm; optical losses in the system, and 100 mJ input energy, the diffuse illumination method has a fluence of 9.3 mJ/cm^2, compared to 175 mJ/cm^2 for point illumination, and 3.54 mJ/cm^2 for the full ring illumination. Full-ring calculations use a beam height of 4 mm circumferentially on a 9 cm diameter phantom, and diffused beam calculations use a beam diameter of 30 mm at the phantom. Even though point illumination has about 49 times the fluence of full-ring illumination method, its amplitudes are much smaller at this cross-sectional depth.

When compared to the diffused-beam and point illuminations, full-ring illumination has a higher PA amplitude at cross-section 3. It has near-constant SNR, CNR, and PA signal amplitude across all cross-sections, making it an effective illumination method for breast imaging. Given that imaging breast regions close to the chest wall (i.e., large vertical depth) are clinically important, the full-ring illumination shows promise in accessing these regions and thus provides a means for reliable whole breast PAT imaging with a ring US transducer.

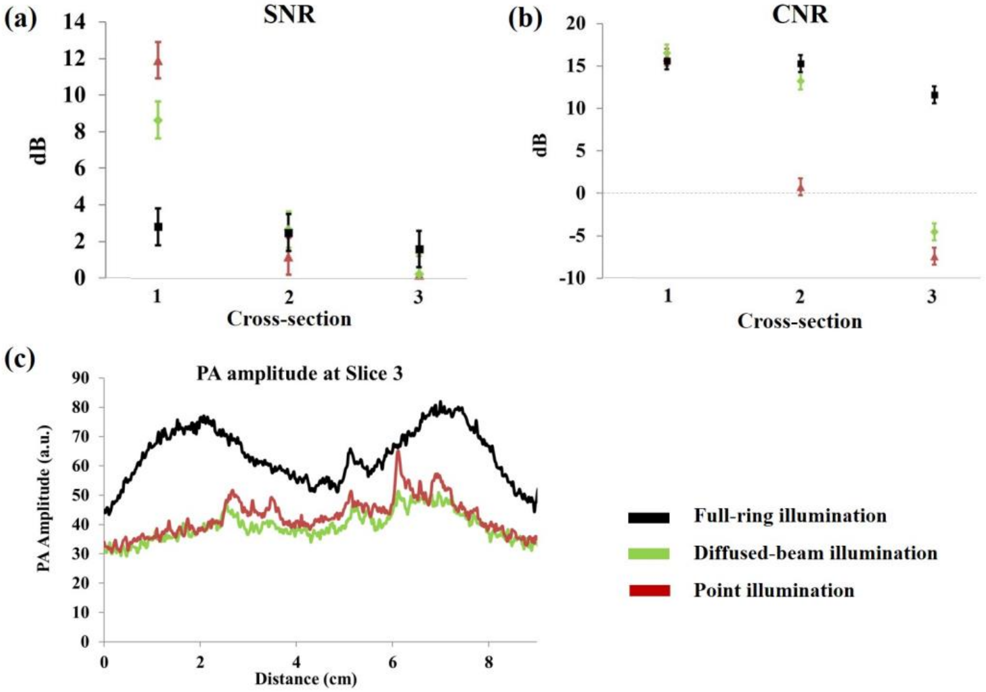

Figure 40: The SNR and CNR of the PA amplitudes at three different cross-sections are plotted in (a) and (b) respectively. For the full-ring illumination, the values are determined based on the illumination at 15 mm below the cross-section of interest. (c) Plots the PA amplitude for the top cross-section (cross-section 3) for full-ring, diffuse, and point illumination.

4.3.2 The PA amplitude of the targeted cross-section as a function of illumination position

In this section, the optimum position for the full-ring beam was investigated by evaluating the effect of the distance between the ring-shaped beam and the targeted cross-section. The distance between the targeted cross-section and the full-ring beam was changed within a range of 0 to 20 mm. Zero millimeters represents the case where the ring beam is illuminating the targeted cross-section at the graphite rod, while the 20 mm case is when the ring beam is 20 mm below the graphite rod (**Figure 41a**). In this study, a selected cross-section was imaged while changing the illumination location from 0 to 20 mm. The five different positions chosen to illuminate the targeted cross-section of the graphite rod were 0, 5, 10, 15, and 20 mm. A 532 nm laser with 100 mJ per pulse energy was used for this experiment. The location of the full-ring illumination was adjusted by translating the phantom in steps of 5 mm in the vertical direction.

In **Figure 41b**, the PA amplitude was measured by drawing a line across the targeted graphite for all five positions. The overall shape of the PA amplitude is constant while the maximum increases as one moves further below the desired imaging cross-section. This increased visibility could be due to the fact that the incidence angle of the beam illuminates the central part of the object more directly as it moves below the cross-section. A possible reason for the stronger PA signal, when illuminating 20 mm below the targeted cross-section, could the incident angle of the light diffusion within the tissue. In the current prototype, the ring mirror is illuminating the object cross-section at an angle of 39^o with respect to the object surface. The optimum illumination will occur if the ring beam falls normal to the surface. The 0 and 5 mm cross-sections use the US image as a mask to crop out the large PA peaks generated at the surface of the phantom. The graphite absorber was embedded within the PVC background with a margin from the surface. Here we only evaluated the signal arising from the absorber. In cases where the illumination was coincident with the center of the transducer, a strong PA signal from the surface was observed (not shown in these masked images). Hence, imaging below the transducer can help better visualize more central parts of the object due to the elimination of a large PA signal arising from the light-entering surface. Large PA signal at the surface is primarily due to the large fluence at the surface, which can affect the visualization of deeper regions due to a limited dynamic range in PA acquisition. This is not the case where the illumination was adjusted with a 10 to 20 mm with respect to the center of the US detectors (i.e., illuminating below the imaged plane). The averaged PA amplitude from all five illumination methods (shown in red in **Figure**

41b) is similar to the 10 mm illumination results. It is worth mentioning that these results are not necessarily general for all ring illumination systems and are dependent on the incident angle of beam with respect to the object (39 degrees in our case). The results might vary in other ring illumination systems if the incident angle is changed.

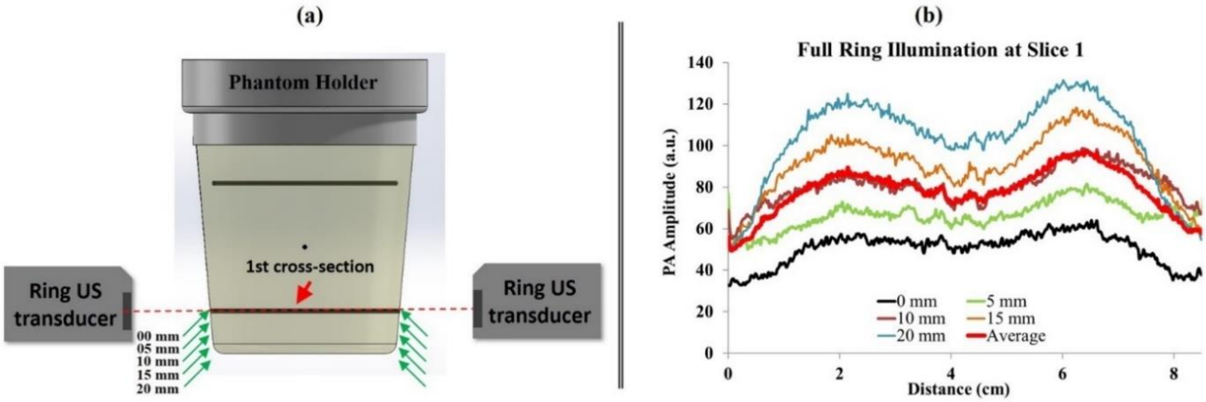

Figure 41: (a) The image shows the different positions of the ring beam based on the targeted cross-section (cross-section 1). The targeted cross-section is located in the central field of view of the US elements. (b) PA amplitude at cross-section 1 plotted as a function of illumination depth below the cross-section.

These findings are important because they help to define the illumination scenario based on the characteristics and size of the given object. For example, large diameter phantom might need to acquire PAT images using more than one position of full-ring illumination to cover the regions closer to the outer surface and deeper regions (with illumination offset from the imaging plane). In addition, illuminating below the targeted cross-section (below the central line of the US elements) could help to limit the high PA signals that are generated from the outer surface of the scanned object. The used illumination method has a significant effect on imaging's vertical depth, which is significant when visualizing anatomy such as the breast.

4.4 Conclusions

Phantoms with horizontal graphite absorbers was used to examine the efficacy of full-ring, diffuse, and point illumination PAT imaging using a ring US transducer. The full-ring illumination was able to provide a more uniform fluence irrespective of the vertical depth of the imaged cross-section, while the point source and diffused-beam resulted in a high fluence at the point of entry, which diminished with vertical depth. In addition, the preliminary results indicate that illuminating an object 10-15 mm below the imaged cross-section of interest might be optimal for this system since it avoids large surface reflections and provides better coverage to the cross-section.

CHAPTER 5 - CHARACTERIZATION OF THE OMNIDIRECTIONAL FULL-RING US/PA TOMOGRAPHY SYSTEM USING EXCISED HUMAN TISSUES

5.1 Introduction

PA imaging is used in many applications where endogenous contrast agents such as angiogenesis and hypoxia are present [70, 105-107]. PA imaging takes advantage of the ability to generate PA signal in tissues as they are illuminated with short pulses of high-energy laser. These signals allow the detection of concentrations of chromophores (such as oxygenated hemoglobin, deoxygenated hemoglobin, and lipids) and the mapping of tissues to find angiogenesis (formation of new blood vessels from others), a process that occurs in the malignant transformation of tumor growth. Angiogenesis (hemoglobin content and tissue vascularization) can be imaged using PA imaging as hemoglobin is a strong absorber in that particular region [66]. In many research studies about the presence of breast cancer, PA techniques for imaging angiogenesis was a key point. Increased blood vascular density (i.e., vascularity) is one of the key biomarkers of breast cancer that can be detected by PA imaging. Strong PA signals can be detected from the angiogenesis when laser energy, with appropriate near-infrared (NIR) wavelength, was applied to the scanned object [108, 109]. Imaging the angiogenesis of the breast can probably increase the sensitivity and specificity of cancer detection in the imaging modality [110]. By using NIR wavelength (756 nm), the vasculature can be visualized throughout the breast tissue as well as the chest [88]. For this reason, PA imaging of angiogenesis helps to increase the visualization of the malignant cells of breast cancer [111, 112].

On the other hand, knowledge of the correlation between breast cancer and hypoxia has largely contributed to recent developments in PA imaging. Hypoxia is defined as low tissue oxygenation, so the blood surrounding affected cells has a lower oxygen level than the blood surrounding normal cells [113]. Usually, cancer cells consume more oxygen than normal cells, leading to a relatively lower tissue oxygenation level in the cancerous fabric [112]. For this reason, hypoxia is a common cancer biomarker [74, 113]. This phenomenon has boosted the efficiency of PA imaging in detecting breast cancer because it is a reliable tool for measuring tissue oxygenation by finding the ratio between oxyhemoglobin to total hemoglobin in the blood (SO_2) [55]. The principle of PA imaging of SO_2 is based on the dissimilarity between optical absorption of oxyhemoglobin and deoxyhemoglobin [60]. Based on the absorption coefficient of oxygenated and deoxygenated blood, using a NIR wavelength could enhance the PA signals significantly during blood imaging in the breast.

In this chapter, several experiments in different tissue-mimicking phantoms were performed to study the efficiency of the omnidirectional full-ring US/PA tomography system in detecting angiogenesis such as blood and mimicked vasculature. By utilizing low laser energy with appropriate wavelength, the results show the benefit of full-ring illumination method in PAT imaging to detect the human blood and mimicked vasculature in remarkable depth. In addition, the mimicked vasculature samples show different PA intensity varied based on the sample density.

5.2 Materials and Methods

5.2.1 UST/PAT acquisition system and laser source

In all experiments in this chapter, the 200 mm diameter, 256-element ring US transducer (Barbara Ann Karmanos Cancer Institute, Detroit, USA) was used for all data acquisition. To optimize the signal-to-noise ratio (SNR) for the given phantom, the ring US transducer uses a 20 dB linear time gain compensation (TGC) for acquiring the data during PAT imaging.

For laser and illumination method, the tunable laser (Phocus Core, Optotek, California, USA) 10 ns pulsed laser was used for all experiments. The large parabolic reflector (P19-0300, Optiforms Inc, California, USA) was used with a 10 mm diameter cone mirror (68-791, Edmund Optics, New Jersey, USA) to create the ring beam. However, the laser energy, applied wavelength, and position of the ring beam are varied in each experiment, so those parameters will be explained individually in each experiment. The UST and PAT data were acquired for all experiments and reconstructed with the same method that illustrated earlier in section (4.2.4).

5.2.2 Utilizing synthetic tissue-mimicking phantom to image different blood concentration

The main purpose of this experiment is to observe the benefit of using the omnidirectional full-ring illumination system to detect different blood concentration, with two different diameters, at different depths. The reason for using full-ring illumination here is to direct the laser beam on one specified cross-sectional area instead of illuminating the whole object with diffused or point beam. A phantom, made of polyvinyl chloride (PVC) (M-F Manufacturing Super Soft, USA) with 0.2% fine ground silica (US Silica MIN-U-SIL5), was built for the purpose of this study. To create a PVC phantom [104], the plastisol was first mixed with the ground silica and then heated in a microwave to 170° C. In the 115 mm diameter mold, ten rods with two different diameters (3 mm and 1 mm) were placed in spiral configuration with different horizontal depths. After that, the 170° C PVC was poured in the mold containing the rods, and then the mold was removed when the PVC cooled down. The final shape shows a 115 mm diameter cylindrical-shaped PVC phantom that has 10 holes organized in a spiral configuration (**Figure 42a**). Three different human blood concentration was chosen to perform three tests (1%, 10%, and 100%). In the 1% and 10% blood samples, the blood was diluted by using degassed distilled water. In each experiment, the blood was injected in the hole by a long-needled syringe to form a blood inclusion. After each experiment, the blood was removed by using the same syringe, and then the phantom washed with water. To avoid error that could occur when using the same phantom with different blood concentration tests, it was decided to start the experiments with the lower concentration blood and also wash each hole with distilled water after each experiment. In this case, the chance of getting a wrong PA signal from the blood that could stick in holes is limited if a high concentration blood sample is used initially. The 115 mm diameter (4 mm thickness) ring-shaped beam was positioned 13 mm below the targeted cross-sectional slice of the phantom (**Figure 42b**). The phantom was illuminated with about 40 mJ/pulse laser beam at 532 nm wavelength. With 14.45 cm^2 ring-shaped surface area, the fluence becomes 2.7 mJ/cm^2. The main reason for choosing the 532 nm wavelength is because it shows a higher absorption coefficient in blood [67].

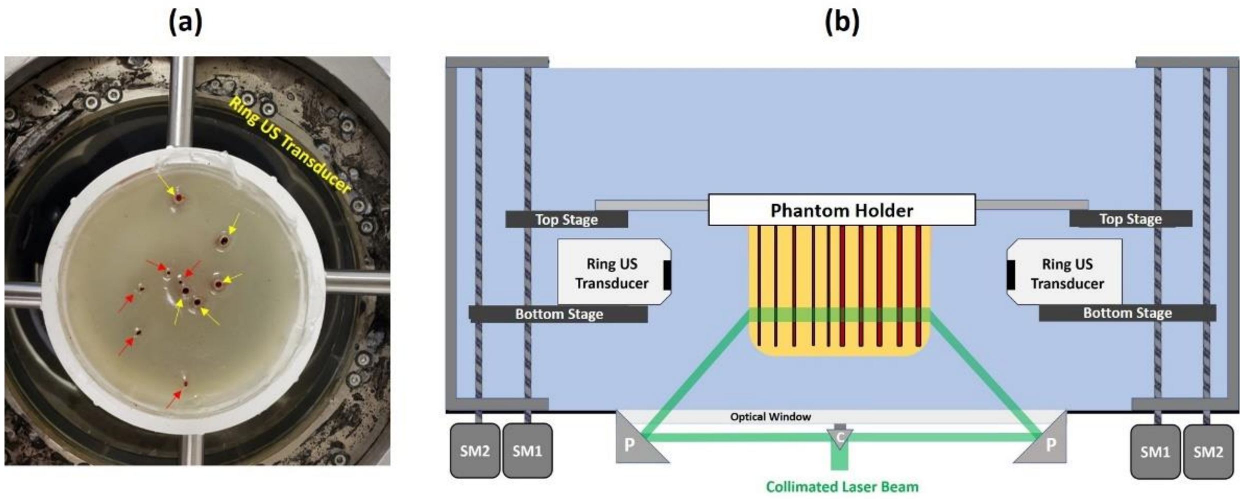

Figure 42: (a) Graph of PVC phantom filled with human blood in 3 mm (yellow) and 1 mm (red) holes. (b) Experimental setup of the different concentration experiments. The ring beam was positioned 13 mm below the targeted cross-sectional slice.

5.2.3 Imaging graphite rods and human blood embedded in breast fat mimicked phantoms

The primary purpose of these experiments was to examine the performance of the omnidirectional full-ring illumination PAT system in detecting light-absorbing objects embedded in real human tissue such as fat. A 600 ml excised female breast fat is centrifuged for 10 minutes at 1200 rpm to separate blood from the breast fat (**Figure 43a**). After that, the fat tissue was used in two different phantom holders to perform two tests. The first phantom was made of an acoustically and optically transparent clear plastic container glued to the phantom holder and then filled with the centrifuged human breast fat. Five light-absorbing materials (2 mm diameter graphite rods) were vertically embedded in the phantom (**Figure 43b**). The diameter of the targeted cross-sectional slice was about 84 mm, and the distance between each graphite rod was about 12 mm, so the central rod was located 42 mm from the outer surface (**Figure 43c**). The transmittance of the clear plastic container was examined and found that it can pass about 75% of the applied laser energy, so there will be a 25% energy loss.

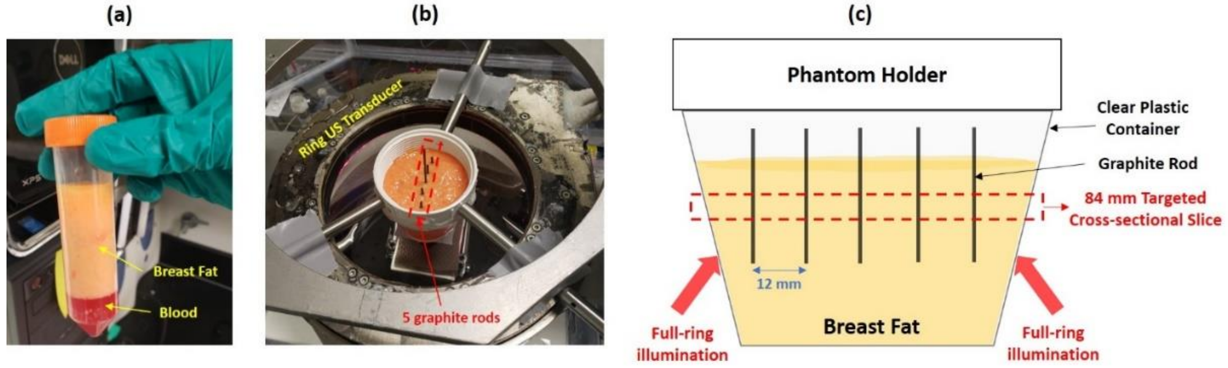

Figure 43: (a) Photograph of the fat sample after 10 minutes centrifuge at 1200 rpm (b) Photograph of the breast fat phantom embedded with five graphite rods (c) Graph shows the dimension of the examined phantom.

The second phantom was made of a transparent cone-shaped clear plastic sheet mounted to the phantom holder and then filled with the centrifuged human breast fat. Two glass tubes, with 3 mm diameter, filled with water and human blood, were placed in different positions inside the phantom (**Figure 44a**). In the first test, the blood tube was about 14 mm from the outer surface, while the tube was 30 mm from the outer surface in the second test. The main reason for using a glass tube filled with water in this experiment is to observe if there is any PA signal that could be created by the tube’s material. In each experiment, the phantom placed inside the scanning tank that filled with degassed distilled water and illuminated with the ring beam positioned 13 mm below the targeted cross-section. It is important to mention that the reason for changing from clear plastic container to the clear sheet is because the sheet shows lower energy loss, about 10%, than the clear plastic container.

In earlier experiments with PVC and gelatin phantoms, blood and graphite showed a high-intensity PA signal at 532 nm wavelength. However, it was not possible to use the 532 nm wavelength in experiment utilizing breast fat because the fat phantom showed high PA signal on the outer surface during PAT imaging (**Figure 44b**). The possible reason for this issue is that the absorption coefficient in fat is higher in 532 nm than 680 nm [114]. In addition, there is a possibility that the breast fat sample may still contain blood molecules, which has a high absorption coefficient at 532 nm, even after centrifugation. For this reason, different wavelengths were tested and found that 680 nm wavelength was appropriate for experiments utilizing phantoms filled with breast fat. The applied laser energy is measured inside the water medium and found that it's 38 mJ/pulse.

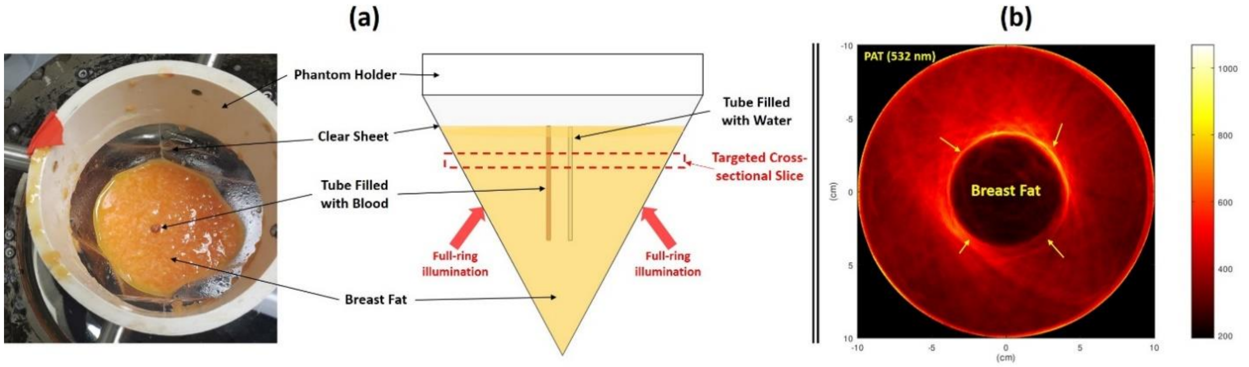

Figure 44: (a) Photograph (left) and graph (right) of the cone-shaped phantom filled with breast fat and embedded with two glass tubes filled with blood and water. The water tube is not clear in the photograph because the tube was dipped in the fat. The full-ring beam was positioned 13 mm below the targeted cross-sectional slice. (b) PAT test of phantom filled with breast fat and embedded with 5 graphite rods. The results show a high PA signal from the outer surface (yellow arrows)

5.2.4 Effect of the vascular density (mimicked) on the PA signal

In this section, two experiments were performed and in each experiment, two different density objects were tested by using the omnidirectional full-ring tomography system. The main purpose of these experiments was to study the effect of the object's density on the intensity of the PA signal. As mentioned earlier in the introduction of this chapter, angiogenesis, such as microvascular structure, is a known sign of cancer cells and can be imaged by using the PA imaging. The high density in vasculature will show high PA signal, which can be used to define the presence of breast cancer.

In the first experiments, vascular density phantom created using a 1 mm diameter, coiled black wire, which was wrapped around an 8 mm abject with different coil pitch. The high-density phantom had more coils per centimeter than the low-density phantom. In each test, the 8 mm diameter dense phantom was placed in the field of view of the ring US transducer inside the imaging tank filled with degassed distilled water (**Figure 45**). The ring beam was used to illuminate the targeted part of the object with 40 mJ/pulse at 532 nm. The reason for choosing 532 nm was due to its high absorption in previous experiments using black graphite rods. In addition, the breast fat background is not used in this test.

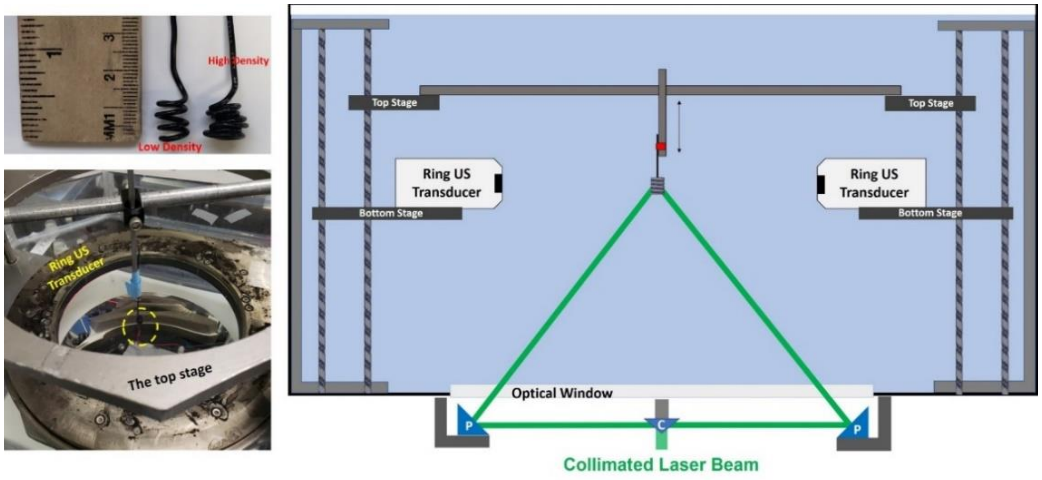

Figure 45: (Left) Photograph displays the size of the low- and high-density phantoms. (Right) The experimental setup of the different density tests.

In the second experiments, two samples were made with clear, flexible tubes with 0.5 mm diameter filled with human blood and coiled around a clear 5 mm tube filled with water. The first object represents the high-density sample with 10 twists per centimeter, while the second object represents the low-density sample with 5 twists per centimeter (**Figure 46a**). In each experiment, the sample was placed in the middle of excised human fat and illuminated with 38 mJ/pulse at 680 nm wavelength (**Figure 46b**). The targeted cross-sectional slice in this test is 84 mm diameter, so the outer surface of the blood sample located about 38 mm from the outer surface of the phantom.

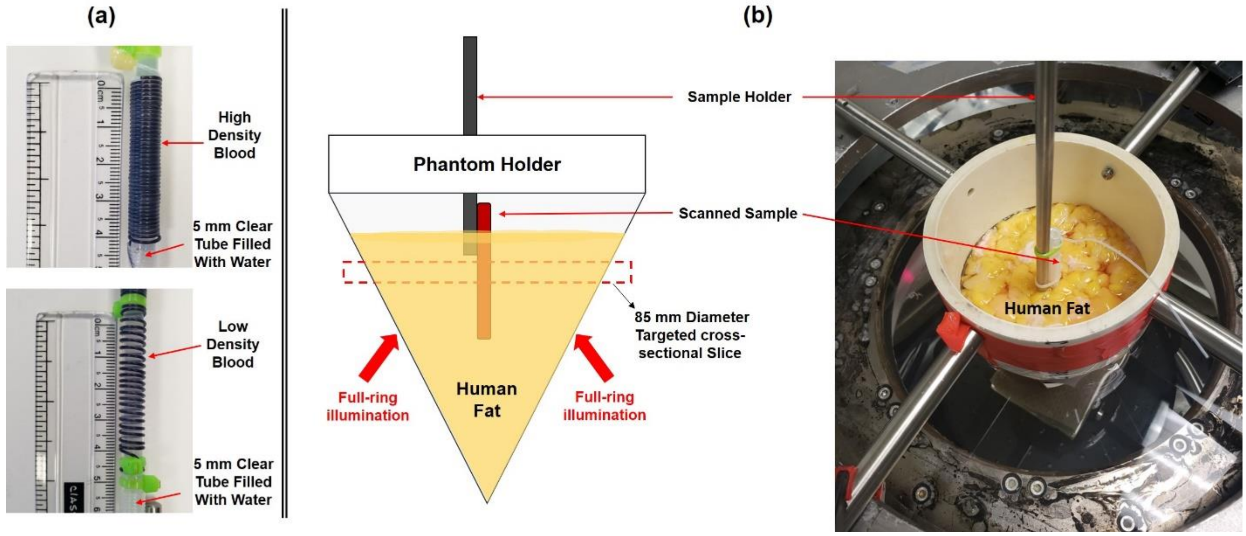

Figure 46: (a) Photograph of the high-density and low-density blood samples. (b) the graph shows the experimental setup of the different density test.

5.3 Results and discussion

5.3.1 Different blood concentration in tissue synthetic phantom

The results discussed in this section focus on analyzing the PAT images and PA signal amplitude from the synthetic PVC phantom filled with three different blood concentrations illustrated earlier in **Figure 42**. The UST and normalized PAT images of the 1%, 10%, and 100% blood concentrations are presented in **Figure 47**. The PAT images are normalized based on the highest PA intensity, which was in the 100% blood concentration test. This allows for visualization of the effect of blood concentration on the PA signal amplitudes in each experiment. As anticipated, the 100% blood sample shows a higher PA signal than the 10% and 1% samples. In addition, all blood inclusions are apparent in the 100% and 10% samples, while the 1% blood sample showed the side blood inclusion, which is closer to the outer surface.

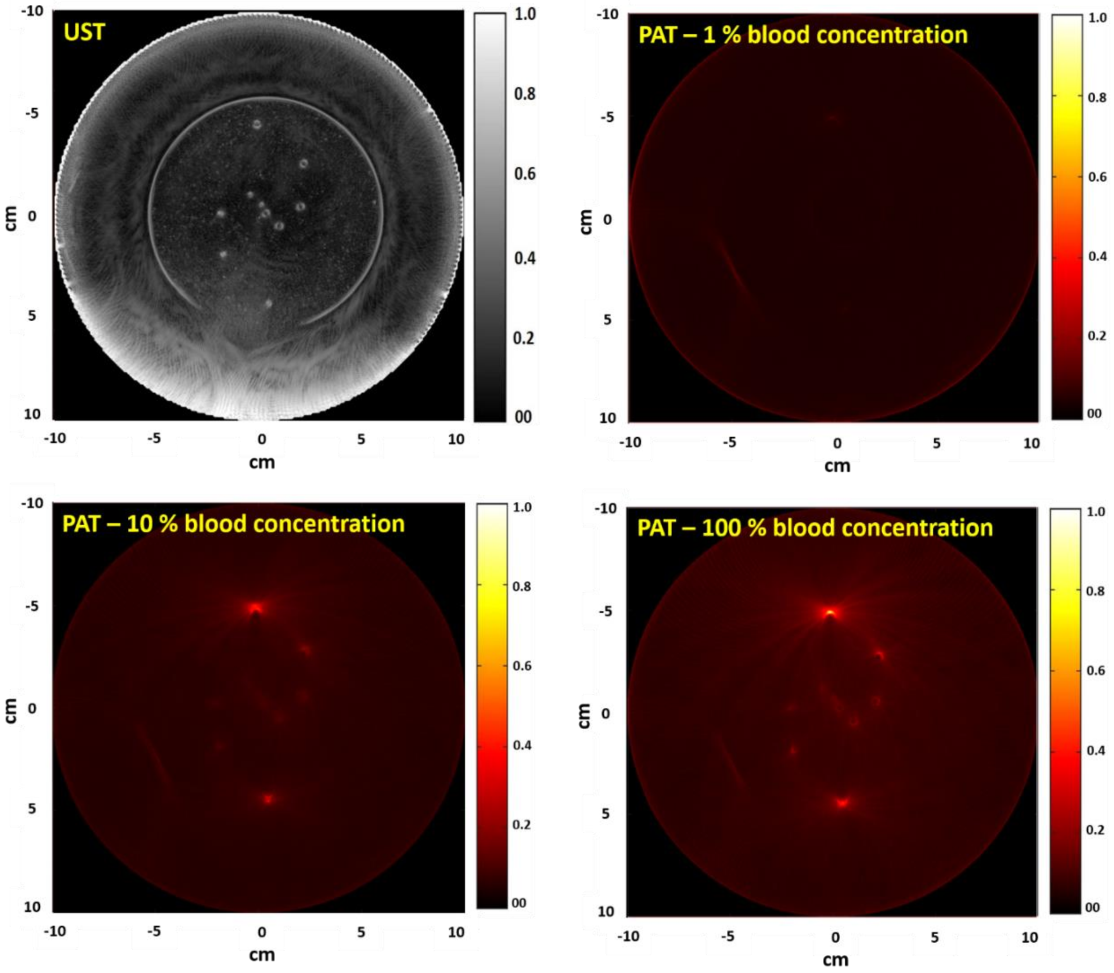

Figure 47: UST and three different blood concentration PAT images of the synthetic tissue-mimicking phantom. PAT images were normalized to the highest PA intensity value.

The PA signal amplitude for each blood concentration across different depths of blood is plotted in **Figure 48** to quantify the results shown in **Figure 47**. By defining the ROI from the UST image, the PA intensity for each blood sample was measured. In general, both graphs show the same reduction in signal intensity with respect to phantom depth in the two different diameter blood inclusion. As expected, the highest concentration blood sample shows a higher PA signal than the lower ones. In 100% and 10% blood concentration, the PA signal dramatically dropped between the first and second blood inclusion, after that the PA signal becomes more uniform in the rest of the blood inclusions. The possible reason for the drop in the intensity of the PA signal between the first and second blood inclusions is due to the reduction in the fluence across the horizontal depth. In addition, the significant uniform PA signal is caused by the uniform distribution of the laser beam created by the full-ring illumination, which is a main advantage of using the proposed illumination method.

Even with the 90% difference in blood concentration between the two samples (100% and 10%), the graphs show a maximum 30% PA intensity difference in the 3 mm samples and about 40% difference in the 1 mm samples. Conversely, the 1% blood test shows a small PA signal in the blood inclusion next to the outer surface, but in general, all blood inclusions show the same PA signal intensity, which is considered as background signal.

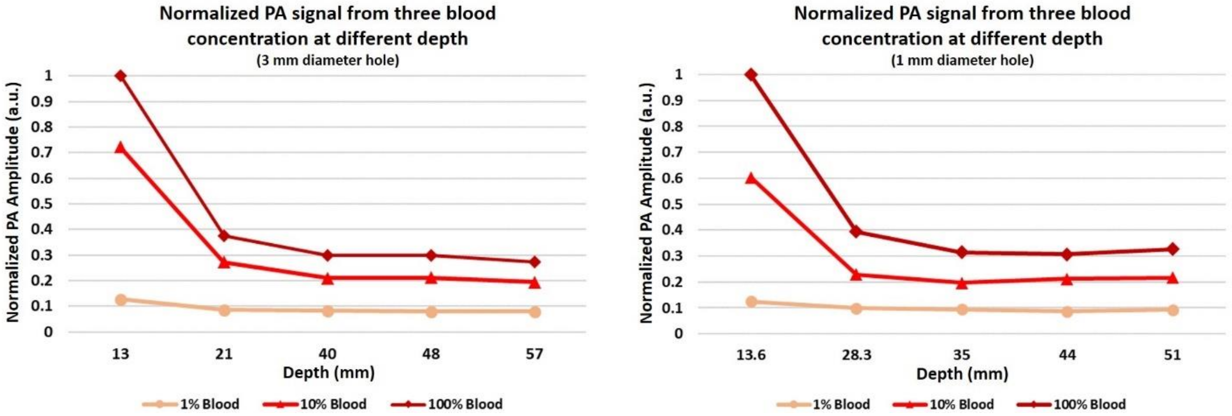

Figure 48: Graphs display the change in the normalized PA intensity based on a change in blood concentration and horizontal depth in 3 mm blood sample (left) and 1 mm blood sample (right)

5.3.2 Imaging light-absorbing materials in breast-fat mimicked phantoms

Figure 49 shows the UST and normalized PAT images of the breast fat phantom embedded with five graphite rods illustrated early in **Figure 43**. The PAT image was normalized by dividing all PA intensity values by the highest value in the image. In the reflection UST image, it was hard to distinguish between the graphite rods and other fat tissue in the phantom. However, the PAT image helped to identify the location of the graphite rods inside the breast fat medium. As seen in the PAT image, graphite rods located close to the outer surface can be seen more clearly than the central rods. Even with the 25% energy loss caused by the clear plastic container, the PAT utilizing full-ring illumination shows all graphite rods and achieved 42 mm penetration depth in this test.

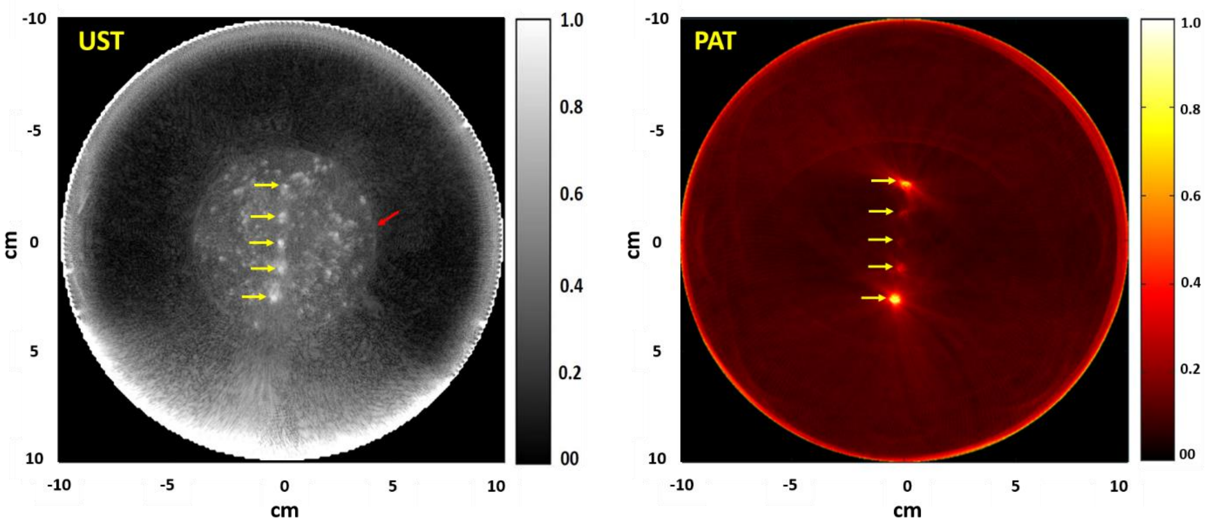

Figure 49: UST (left) and PAT (right) images of the breast fat phantom with five graphite rods (marked with yellow arrows). The red arrow in the UST image shows the outer surface of the phantom, which is the clear plastic holder.

The mean, maximum, and minimum normalized PA intensity was measured in the ROI of each graphite rod. In general, the PA intensity showed a reduction from the outer surface to the center of the phantom (**Figure 50**). However, there was a marked difference in the PA amplitude between the side rods (1 to 5) and (2 to 4). There are possible reasons for the difference in the PA intensity. The first possible reason is that the position of the graphite rods with respect to the outer surface is not equally spaced, which causes the difference in signal intensity. The second possible reason is due to the difference in beam intensity. Ideal ring illumination occurs if the laser beam falls on each optical part without any deviation that could arise from the movement of the optics. Because the cone-shaped reflector mirror is taped to the bottom of the imaging tank, some misalignment could occur if the cone-shaped mirror is moved few micrometers. In addition, the phantom is placed in the exact center of the ring US transducer, but still, the phantom could move from its position due to the water pressure that occurs during the tank filling. Moreover, the phantom could move from the vibration created by the stepping motors during the vertical adjustment of the phantom. Overall, the full-ring illumination still shows a promising penetration depth in the targeted cross-sectional slice.

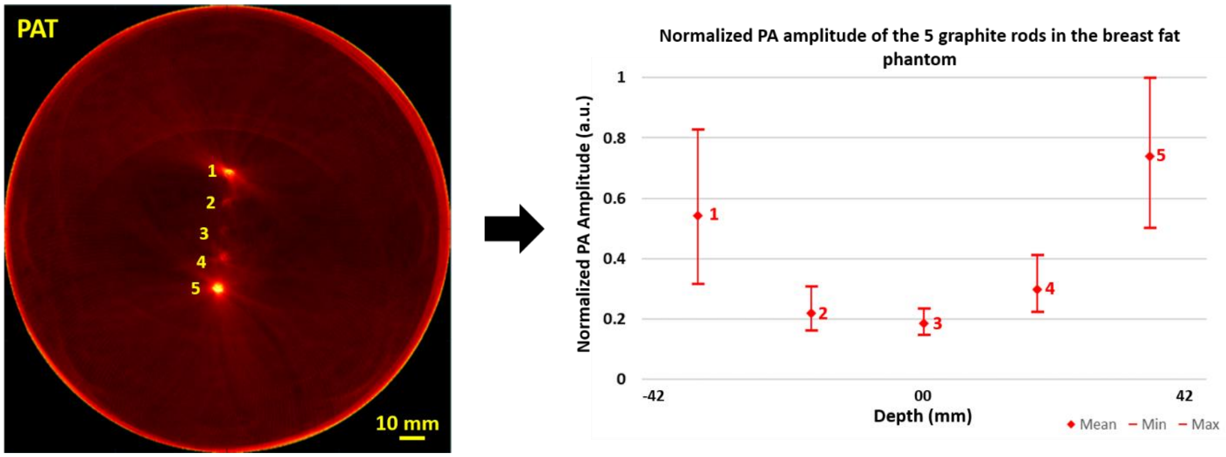

Figure 50: Graph of the normalized PA amplitude of the five graphite rods in the breast fat phantom. The PA amplitude was measured by calculating the PA intensity of the ROI of each object.

In the same phantom, one more test was performed to observe the change of the PA intensity of the central object, which was located 42 mm from the outer surface. In this test, the phantom was illuminated with the same energy after removing all four side graphite rods and keeping the central one. The UST and PAT images were reconstructed, and the mean PA intensity of the ROI was measured and compared with the PA intensity of the central rod measured in the previous experiment. The PA intensity was normalized by dividing all values in the ROI by the highest measured value in both tests. The results showed that there is a 30% difference in the mean PA intensity after removing the surrounding graphite rods (**Figure 51**). In addition, the variation between the maximum and minimum PA signal is increased in this test. It was concluded that the intensity of the PA signal is affected during full-ring illumination if the targeted object was surrounded by other light-absorbing objects or tissue.

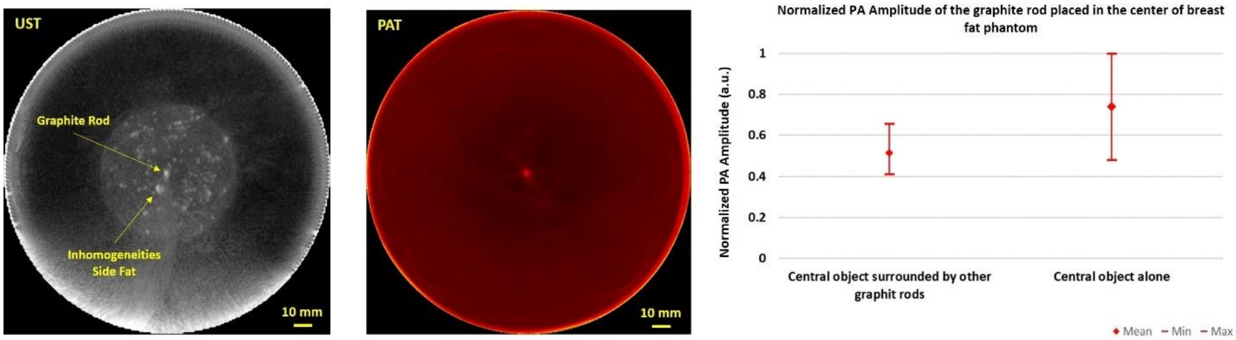

Figure 51: (Left) UST image of the breast fat phantom after removing four graphite rods and keeping the central rod. (Middle) the PAT image shows the location of the central object. (Right) Graph of the mean, minimum, and maximum PA intensity of the central graphite rod under two conditions.

Figure 52 shows the UST and PAT images of the cone-shaped breast fat phantom, illustrated in **Figure 44**. In both tests, the tube that filled with human blood could be seen clearly in 14 mm and 30 mm depths. Instead, the water tube was observed in the UST images while it can not be seen in PAT images. Using 680 nm wavelength, which can be absorbed by the blood and transmitted by water, explain the reason for not observing the water tube. The same was true for previous experiments; the intensity signal of the targeted object was affected by the horizontal depth. For this reason, the blood tube was more apparent in the 14 mm than the 30 mm depth.

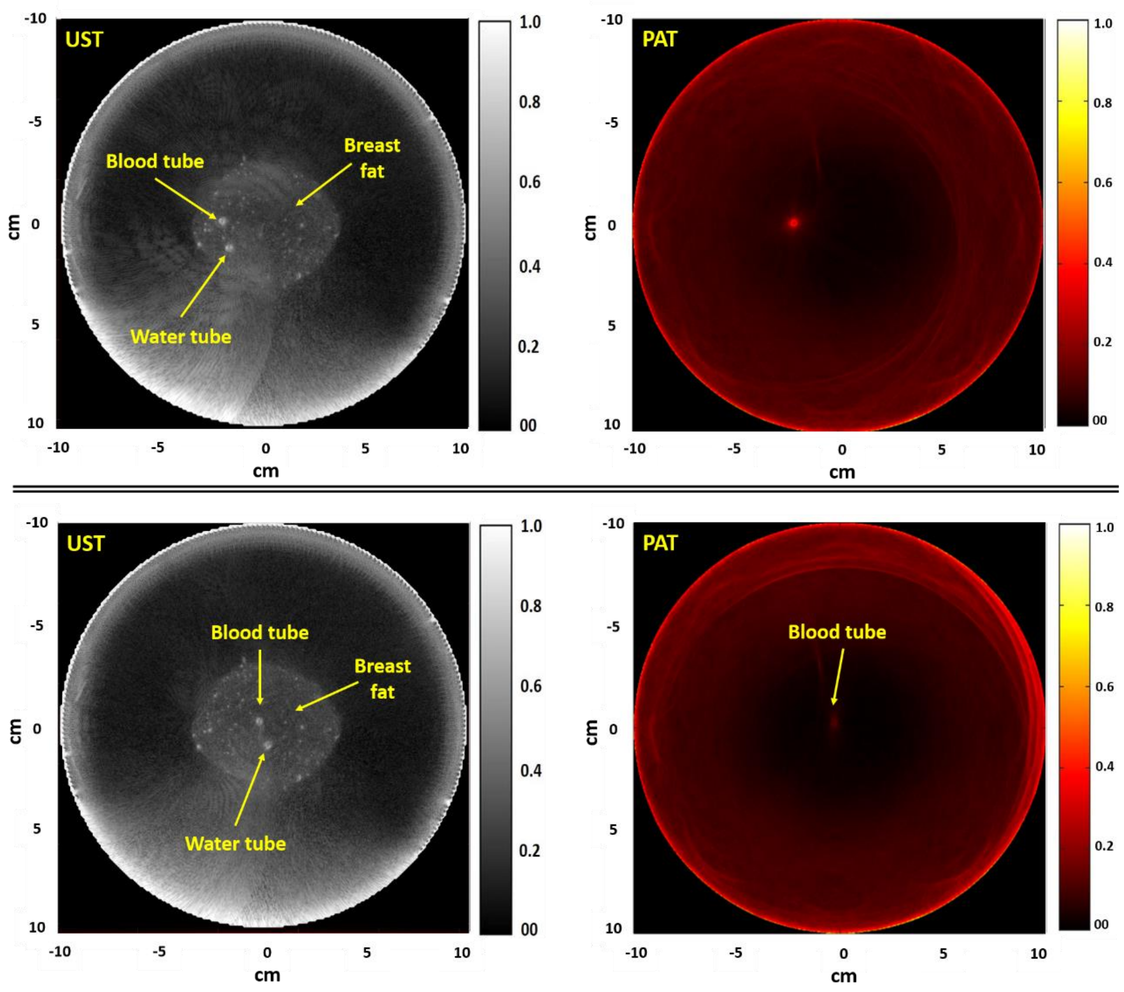

Figure 52: UST and PAT images of two tests using cone-shaped phantom filled with breast fat and then embedded with blood and water tubes. The top part represents the first test where the blood tube was 14 mm from the outer surface, while the bottom part is the second test where the blood tube was in the phantom center (30 mm).

The mean, maximum, and minimum PA signal intensities of blood tube in both tests were measured and calculated by defining the ROI of the blood tube and then normalizing them (**Figure 53**). There is about a 53% drop in the mean intensity of the PA signal between the two positions (14 mm and 30 mm) of the same blood tube. In addition, the object located in the center shows mean PA intensity closer to the maximum and minimum values, while the side object displays a significant difference between the maximum and minimum intensity values. This finding was observed earlier in **Figure 50** and was always linked with lower standard deviation. The explanation for that is because more penetration depth leads to a reduction in the fluence, decrease in intensity variation, which causes a low standard deviation.

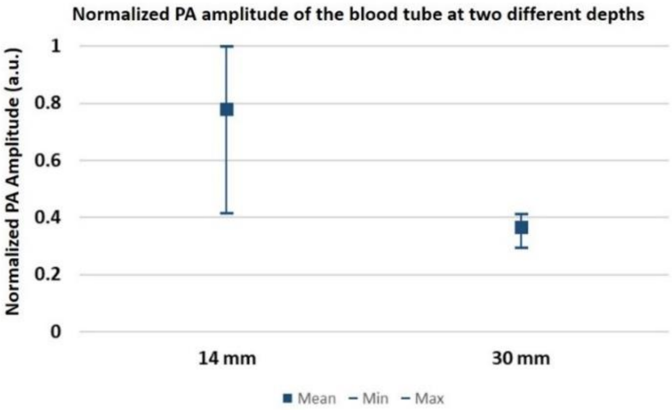

Figure 53: Graph of the normalized mean, maximum, and minimum PA amplitude of a blood tube positioned 14 mm and 30 mm from the outer surface.

5.3.3 Effect of the mimicked vascular density on the intensity of PA signal

In **Figure 54**, the UST and PAT images are shown for low-density and high-density objects illustrated in **Figure 45**. The PAT images were normalized by dividing each image with the highest measured PA value in both experiments, which was in the high-density object. In general, both objects inside the water medium appear clearly in the PAT images because the sample was not surrounded by tissue or a barrier in the path of the ring beam.

To quantify the results shown in **Figure 54**, the mean, maximum, and minimum PA signal amplitude across the different phantoms are plotted in **Figure 55**. The UST images were used to define the ROI of the targeted object in the PAT images. The mean, maximum, and minimum PA intensity were measured and then used to normalize the graph by dividing all values by the maximum intensity value in the high-density object. In this experiment, the high-density sample showed higher mean PA intensity than the low-density one. In addition, the graph shows high variance between the maximum and minimum PA intensity value in both objects. The high variance is caused by the fluence that occurred to the phantom placed in the water medium background.

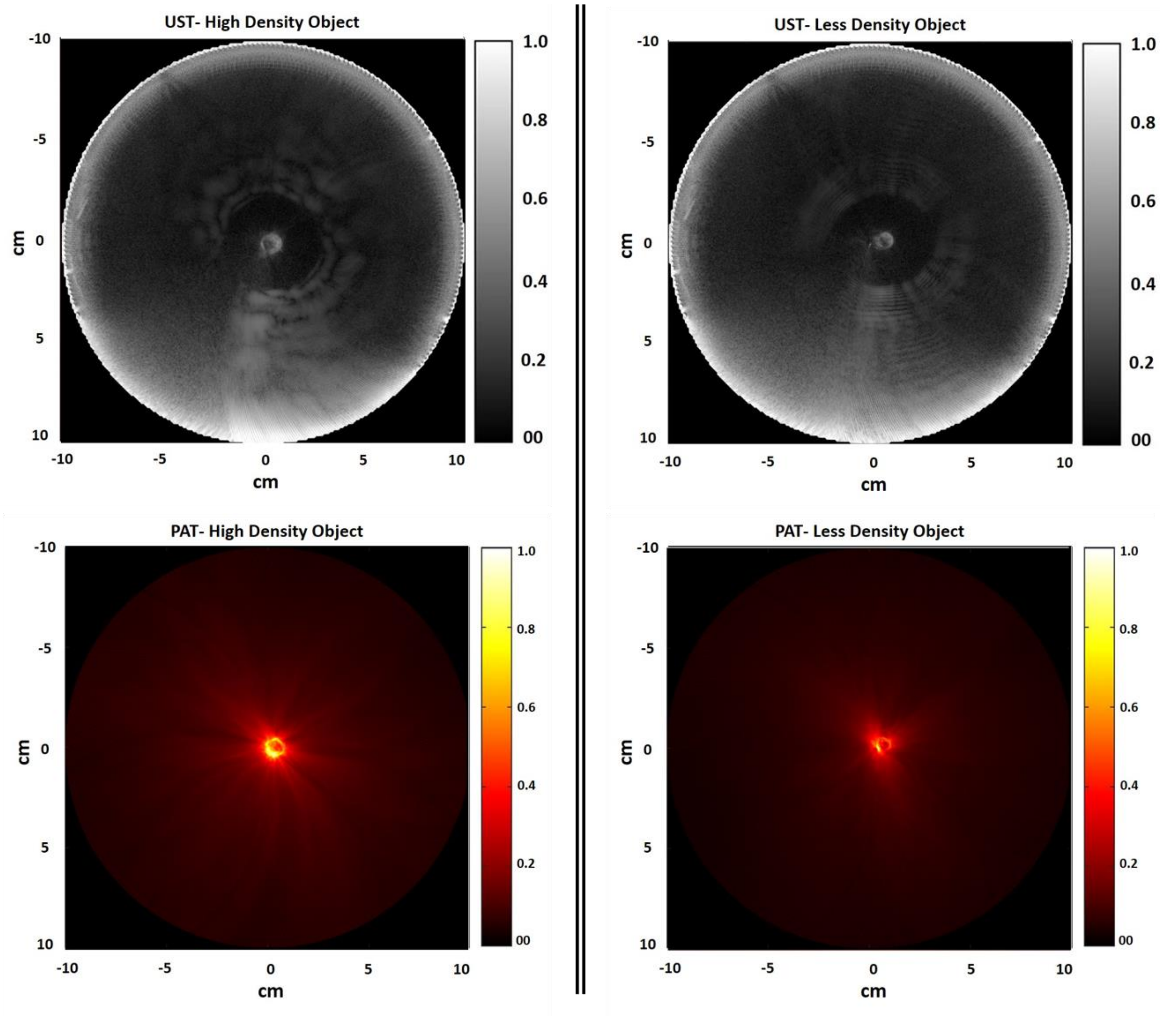

Figure 54: UST and normalized PAT images of the high-density (left) and low-density (right) light-absorbing object.

The weight of both objects was measured, and it was found that the high-density object was 0.645 g, while the low-density was 0.355 g**,** so the difference in weight was about 55%. In **Figure 55**, there is a 50% difference in the mean PA intensity between the two different density samples. We conclude in this experiment that there is a relation between the intensity of the PA signal and the object’s weight (density). The mean PA amplitude double in value as the object’s weight doubled.

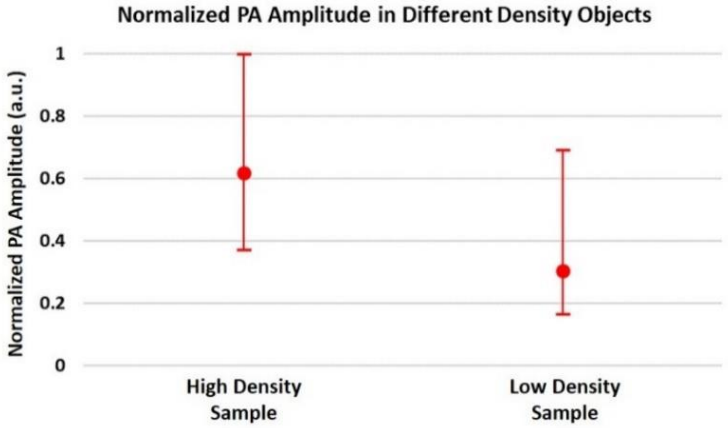

Figure 55: Normalized mean, maximum, and minimum PA amplitude of the high-density and low-density samples.

Figure 56 shows the UST and normalized PAT images of the different density vasculature experiments that illustrated earlier in **Figure 46**. The UST image demonstrates the content of the phantom that consists of human fat and the mimicked blood vasculature object. Conversely, the PAT image shows the blood vasculature, which has a high absorption coefficient at 680 nm. As anticipated, the targeted sample that mimicked high-density vasculature is clearly seen in the PAT image than the sample with low-density blood vasculature. In both PAT images, the PA signal is generated from the outer surface of each sample. Even with the low fluence (3.6 mJ/cm^2) that applied on the used phantom, the full-ring illumination was able to reach penetration depth close to 38 mm.

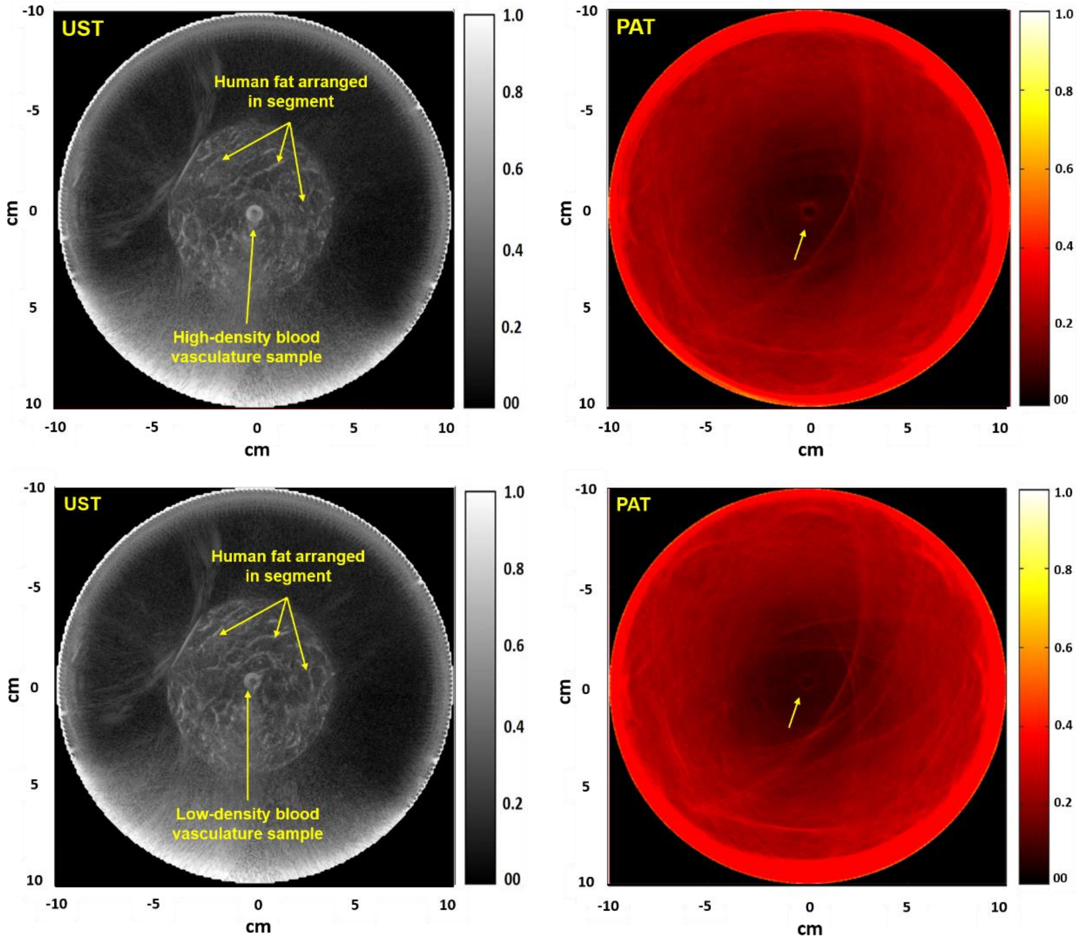

Figure 56: UST and normalized PAT images of high-density (up) and low-density (down) mimicked vascular phantom.

The PA amplitude was measured by drawing 3 cm line across the targeted vasculature samples. **Figure 57a** shows that the high-density sample has a higher PA signal generated from the outer surface than the low-density sample. In addition, both edges in each graph (labeled in red arrow) look uniform in both graphs, and that could be interpreted by the uniform distribution of the laser energy caused by the full-ring illumination method.

Same to previous experiments, the mean, maximum, and minimum intensity of the PA signal, which created by the outer surface of the high-density and low-density samples, were measured to observe the difference in the intensity of the PA signal (**Figure 57b)**. As anticipated, the mean intensity of the PA signal is high in the high-density sample than the low-density one. This finding is explained by the effect of vasculature density on PA signal, so the dense vasculature will show strong PA signal. However, the difference in the mean PA intensity between the two samples was 25%, which was unexpected since the samples have 2:1 difference in density. A possible reason for this finding is the difference in the sample position inside the fat, which causes variations in the PA amplitude. A second reason could be that even if the low-density sample was planned to have 5 coils per centimeter, there was a chance that the targeted cross-sectional slice had more than 5 coils at the time when the sample was embedded inside the human fat.

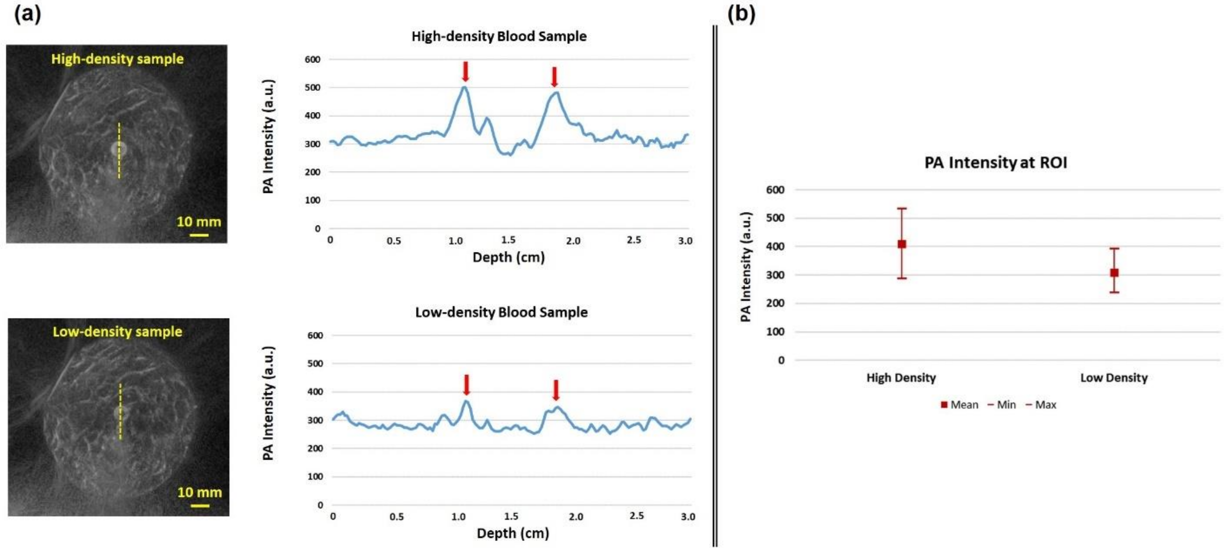

Figure 57: (a) Graphs illustrate the PA signals created by the outer surface of the targeted samples by drawing a single line across the targeted sample. The red arrows represent the edges of the sample. (b) The mean, maximum, and minimum PA intensity created by the ROI of the high and low-density samples.

5.4 Conclusion

Several experiments were performed to study the efficiency of the PAT utilizing full-ring illumination method on detecting angiogenesis contrast agents such as hemoglobin content and mimicked tissue vascularization. A synthetic PVC phantom, with 10 holes aligned in spiral configuration filled with different blood concentrations, was examined to observe the effect of blood concentration on PA signal at 532 nm wavelength. The 100% blood concentration showed the highest PA signal compared to 10% and 1% blood concentrations. In addition, the intensity of the PA signal showed 40% difference in PA signal between the 100% and 10% blood concentrations, while the 1% blood concentration test showed, in general, a uniform background PA signal. In addition, even with low applied fluence, the proposed PAT system was able to reach up to 42 mm penetration depth in real human tissues such as breast fat. Besides, it was able to show a clear PA signal from a blood tube positioned at 30 mm from the outer surface. Moreover, the variation of the mimicked vasculature density shows a variation on the PA intensity created from the sample, so the vasculature density has a direct relation to the intensity of the PA signal. Lastly, the PAT imaging using full-ring illumination shows a uniform PA signal at the outer surface of the targeted sample. Future experiments will focus on enhancing the intensity of the PA signal by increasing the applied fluence (energy/area) and improving the incident angle of the ring beam.

CHAPTER 6 - POTENTIAL APPLICATION OF THE OMNIDIRECTIONAL FULL-RING US/PA TOMOGRAPHY SYSTEM FOR MOLECULAR IMAGING OF BREAST CANCER USING MOLECULAR EXOGENOUS CONTRAST AGENTS

6.1 Introduction

In PA imaging, using contrast agents could increase the sensitivity of PA signals in the scanned region, and that will help in early detection of breast cancer. The development of PA imaging has coincided with the development and use of various contrast agents for molecular imaging [115]. In this chapter, a brief review is given about existing literature on PA imaging using exogenous contrast agents, such as metallic nanostructures and dyes, to target elements associated with breast cancer. After that, several preliminary experiments, utilizing gold nanoparticle (gold NPs), have been performed to examine the efficiency of the full-ring illumination system in detecting a sample of exogenous contrast agents at applied wavelengths. The proposed full-ring illumination PAT system shows promising results in imaging exogenous contrast agents embedded in a different medium. However, limitation related to the PAT system design, which caused energy loss at NIR wavelength spectrum, was observed.

6.2 Molecular Contrast Agents in Breast Cancer PA Imaging

6.2.1 Introduction

In the human body, there are a lot of elements associated with breast cancer. Examples of such elements associated are Human Epidermal Growth Factor (HER2), Estrogen Receptor (ER), Enhanced Permeation and Retention (EPR), and Epidermal Growth Factor Receptor (EGFR). The HER2 and ER are some of the dominant signaling pathways associated with human breast cancer [116]. HER2 is a receptor protein that is involved in regulating normal cell growth, especially in the ovaries and breast. The genes that code for the expression of HER2 play an important role in the development of breast cancer. Overexpression of the HER2 gene is a common defect associated with about 25% of breast cancers [117]. Since HER2-positive cancers have a poor prognosis, there is a need for effective diagnostic methods, such as PA modality.

Conversely, estrogen is a steroid hormone that regulates sexual function and reproductive development, primarily in women. Circulating estrogen binds to ER expressed in target tissues, such as those in the breast and uterus. The majority of human breast cancers start as estrogen-dependent [118]. Tumor progression is associated with differential expression of ER co-regulatory proteins leading to altered functions of ER [118]. ER-positive breast cancer accounts for about 75% of all breast cancers [119].

The EPR effect refers to the accumulation of nanoparticles and other macromolecules in tumor cells [120]. The EPR phenomenon involves anomalous molecular dynamics, which favor the deposit of specific sizes of macromolecules, such as NPs and liposomes. Because of enhanced permeability of tumor vasculature in breast cancer, the use of nano-sized agents has shown potential for enhancing the delivery of anticancer drugs. Moreover, the EPR effect associated with tumor vasculature offers the potential for the systemic delivery of anti-cancer agents. In addition, EPR is a potent target for improving both imaging and therapy [121]. Various contrast agents have exhibited the potential to accumulate in extra-vasculature compartments in cancer tissues through the EPR effect and to alter the absorptive properties of tumor tissues [122]. These contrast agents can be used for detection of EPR in cancer cells using PA imaging.

The EGFR is a transmembrane glycoprotein involved in the signaling of specific extracellular protein ligands. Overexpression of the EGFR gene is associated with various types of tumors. In breast cancer, the EGFR gene is amplified, resulting in a defective gene product and specific transmembrane dysfunctions. The EGFR has been associated with an aggressive subtype of breast cancer called Triple Negative Breast Cancer (TNBC) [123]. Consequently, these factors hold remarkable potential for the diagnosis and molecular targeting of breast cancer subtypes.

To target elements associated with breast cancer, exogenous contrast agents such as metallic nanoparticles, dyes, and carbon nanotubes can be used for this purpose. **Table 3** summarizes the literature in terms of the target PA agent, type of the contrast agent, the target object in breast cancer, the modification envisaged in the papers, and the application of the described methods.

6.2.2 Metallic nanoparticles (NPs) for breast PA imaging

Metallic nanoparticles (NPs) have important optical absorbance characteristics that make them suitable candidates for PA imaging. The metallic NPs also exhibit surface plasmon resonance and surface modification, which can be modified into different sizes and shapes. NP-based contrast agents promise improved potential for the detection of ER-positive cancer cells *in vivo* using PA imaging, CT scan, and Near-Infrared Fluorescence imaging [124]. Different studies were performed to validate gold NPs in breast PA imaging. An EGFR antibody conjugated to gold nanorods has been used to detect breast cancer in mice by using PA imaging [125]. The objective of the study was to assess the potential of using US-guided PA imaging and anti-EGFR antibodies to detect EGFR-positive breast tumors [125]. In another study, targeted nanodiamonds conjugated with HER2 peptide have been used as contrast agents to ensure high resolution of PA imaging. The findings indicate that contrast agents accumulate in tumors via the EPR effect [117]. A pigment called astaxanthin has been used for gold nanoparticle (AuNP) formation. These particles were found to have cytotoxic effects that could be detected using 808 nm NIR illumination. By applying the synthesized AuNPs in photoacoustic imaging coupled with ultrasound, good PA images were obtained [126]. AuNPs have been used as contrast agents targeting HER2 and EGFR receptors using photoacoustic imaging [127]. Silica-coated gold nanorods (SiO2-AuNRs) were used as agents for PA imaging targeting of the EGFR to improve prognosis [128]. Iron oxide NPs (IONPs) have been developed as useful agents for targeting HER2 receptors with PA imaging. A study demonstrated the suitability of IONPs as contrast agents for *in vivo* breast tumor imaging [129]. Silver nanosystems also provide robust contrast agents for breast cancer PA imaging and *in vitro* image-guided therapy [130]. The concentration-dependent PA signal from the Ag nanosystem in an *ex vivo* sample was measured, and the findings indicated that the Ag nanosystem could augment image-guided breast cancer therapy. Nanodiamonds are also potential contrast agents that have been developed for HER2 targeted breast cancer imaging [131]. Conjugated polymer (CP) nanoparticles were proposed as optical contrast agents for PA molecular imaging of breast cancer. The CP-based probes accumulate passively in tumor cells via the EPR effect [132]. Copper NPs also could be used as a contrast metal agent for PAT. Researchers encapsulated multiple copies of copper within phospholipid-entrapped NPs. The particles, measuring 70-80 nm, exhibited an optimal diameter for distribution in lymphatic systems. The results show the usefulness of copper as an optical contrast agent in breast cancer treatment [133].

6.2.3 Dyes for molecular-specific PA imaging

The second category of PA contrast agents is comprised of dyes, typically nanometer-scale fluorescent molecules, such as Indocyanine-green (ICG), methylene blue, Evans Blue, and Alexa Fluor 750. Because of their low molecular weights, organic fluorescent dyes can serve as contrast agents when using histochemical assays. The performance of ICG as a contrast agent has been evaluated in both PAT and fluorescent molecular tomography [134]. Kim et al [135] developed nanoparticles, measured at 100 nm and containing ICG, as contrast agents for PA imaging to investigate image contrasts based on PEBBLE (photonic explorers for biomedical use by biologically localized embedding) concentration in phantom objects. Conversely, Ma et al [136] characterized ER-positive breast cancer cells using the Indocyanine blue contrast agent. The study identified ER-beta as a mediator of ER action and a novel target for cancer therapy. Erpelding et al [137] used methylene blue as a contrast agent for PA imaging in rat sentinel lymph nodes (SLNs), which are associated with breast cancer. The purpose of the study was to evaluate the feasibility of SLN mapping using PA techniques. The researchers imaged the accumulation of methylene blue dye in axillary lymph nodes using PA imaging systems. The findings showed that PA images could facilitate the visualization of methylene blue accumulation in SLNSs.

Table 3: Summary of the metallic nanoparticles and dyes that have been used in some studies of breast cancer cells**.**

PA Agent	Type	Targeted Object	Modification	Application
Metallic nanoparticles:				
Gold-nanorods [125]	Noble metal nanoparticles	EGFR-targeted	Conjugation with US-guided PAI and EGFR antibody	in vivo
Irradiated nanodiaomonds (IND) [117]	Nanoparticle	HER2	--	in vivo
Au nanoparticle (AuNP) [126]	Noble metal nanoparticle	--	Astaxanthine	in vivo
Gold NPs [127]	Noble metal nanoparticle	HER2 and EGFR	--	--
Silica-coated gold nanorods (SiO2-AuNRs) [128]	Nanoparticles	EGFR	Silica coating	--
Iron oxide NPs (IONPs) [129]	Nanoparticles	HER2	Anti-HER-2 moieties	In vivo
Silver nanoparticles [130]	Noble metal nanoparticle	EPR non-targeted	PEGylated form of AgNPs	in vivo ex vivo
Nanodiamonds [131]	Nanoparticles	HER2	PEG	in vivo
Copper neodecanoate nanoparticles [133]	Noble metal nanoparticle	None	--	in vivo
Conjugated polymers (CP) nanoparticles [132]	Nanoparticles	EPR	--	in vivo
Dyes:				
Indocyanine green (ICG) [135]	NIR fluorescent dye	HER2	PEBBLE	in vivo
Indocyanine blue [136]	NIR fluorescent dye	ER	--	in vivo
Methylene blue [137]	NIR dye	None	--	--

From the brief literature, it was concluded that metallic NPs are a very useful tool that could conjugate with elements related to the breast cancer to increase the sensitivity of the PA imaging. In the next section, three preliminary studies utilizing gold NPs filled inside a glass tube and imaged at different wavelengths and mediums to observe the ability of the proposed omnidirectional full-ring US/PA tomography system to perform future spectroscopic imaging. Because the optical parts in the system have a different reflectance for different wavelengths and water transmittance varies with wavelengths [138], it was essential to first study the energy loss in the system at NIR wavelength range before doing PAT studies to image the gold NPs sample.

6.3 Material and Methods

6.3.1 Effect of optical parts and water medium on laser energy at near-infrared (NIR) wavelengths

The primary purpose of measuring laser energy is to compensate the measured PA signal, which is created from the targeted cross-sectional slice that has the gold NPs, with the applied laser energy. To perform the measurement, a power meter was placed in three different locations of the laser path in the system, and then the energy (mJ/pulse) was measured. The first measurement was located before the imaging tank, which represents the original laser energy. At this location, it was decided to maintain the laser energy around 100 mJ/pulse in all selected wavelengths. The examined wavelength range in this study was between 680 nm to 980 nm with 20 nm increment. The second measurement was inside the empty imaging tank (no water) to observe the effect of the reflected mirrors and the H-K9L optical window on the laser energy. The optical mirrors in the path were the protected silver 45-degree mirror, protected aluminum cone-shaped reflector, and protected aluminum parabolic mirror. The third measurement was similar to the second one except that the imaging tank was filled with degassed distilled water to study the effect of water and optical components together on the laser energy. For the second and third measurements, the power meter was placed inside the imaging tank in a position where the ring beam ends at one point (**Figure 58**). The laser path inside the water medium was calculated and found it was about 17.7 cm.

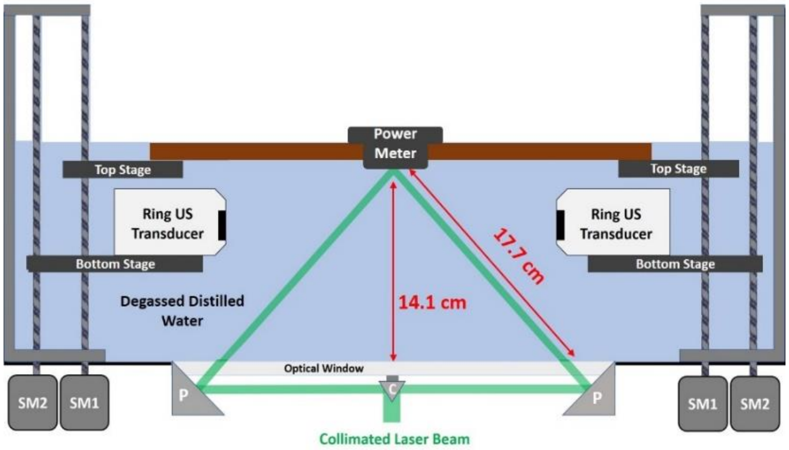

Figure 58: Experimental setup used to measure the energy loss, created from the optical components and water, inside the imaging tank.

6.3.2 Imaging gold NPs in water medium using two different imaging systems

A 3 mm diameter glass tube filled with pure Silica-coated Gold Nanorods (79327-L003M, NanoHybrids, TX, USA) with 5 OD (optical density) concentration and the peak absorption is at 808 nm wavelength (**Figure 59a**). The gold NPs and water tubes were placed inside a phantom made of a transparent cone-shaped plastic sheet filled with degassed distilled water. After that, the phantom was placed inside the imaging tank filled with the degassed distilled water. The main reason for imaging the water tube is to test if there is any signal that could be created from the tube material at the targeted wavelengths. The ring US transducer, which encircles the phantom, was used to acquire the UST and PAT data (**Figure 59b**). The phantom was illuminated with a ring beam originated from the optical parts of the proposed system. The same tunable, 10 ns pulsed laser (Phocus Core, Optotek, California, USA) was used to create a laser beam at different wavelength range. The ring laser beam was positioned 13 mm below the targeted cross-sectional slice. Because the water showed a significant effect on the laser energy after 900 nm, and because the peak absorption of the tested sample is at 808 nm, it was decided to study the sample between 680 nm and 900 nm with 20 nm increments. In each wavelength, PAT data were acquired and stored; also, the laser energy was measured at a different position in the laser path.

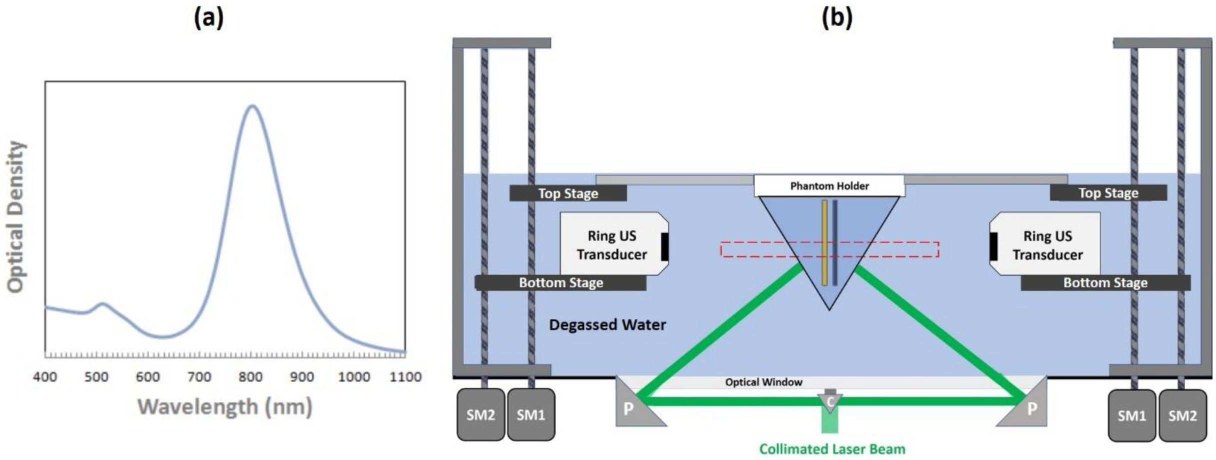

Figure 59: (a) Optical absorption of the gold nanorods that been used in the experiment. The graph was adapted from NanoHybrids Advanced Imaging Solution[5] (b) The experimental setup of the gold NP experiment illustrates the phantom embedded with gold NP and water tube.

To investigate the results created from the full-ring PAT system, it was essential to study the same sample (gold NPs in a glass tube) by using other PA imaging system. In the second experiment, the gold NPs tube was placed inside a degassed distilled water medium and then illuminated with a point beam created from the same 10 ns tunable laser source. At each wavelength used (680 nm to 900 nm), the laser energy was measured by using a power meter in the laser path. For US and PA signal acquisition, a programmable US scanner (Vantage 128, Verasonics Inc., Washington, USA), equipped with linear array transducer operating at 8.4 MHz center frequency, was used for the purpose of the study. **Figure 60a** illustrates the experimental setup of this test, while **Figure 60b** shows the US image and PA image at 800 nm.

---

[5] https://cdn.shopify.com/s/files/1/0259/2325/files/Tech_Specs_NanoHybrids_-_Silica coated_Gold_NanoRods.pdf?2247195054622194334

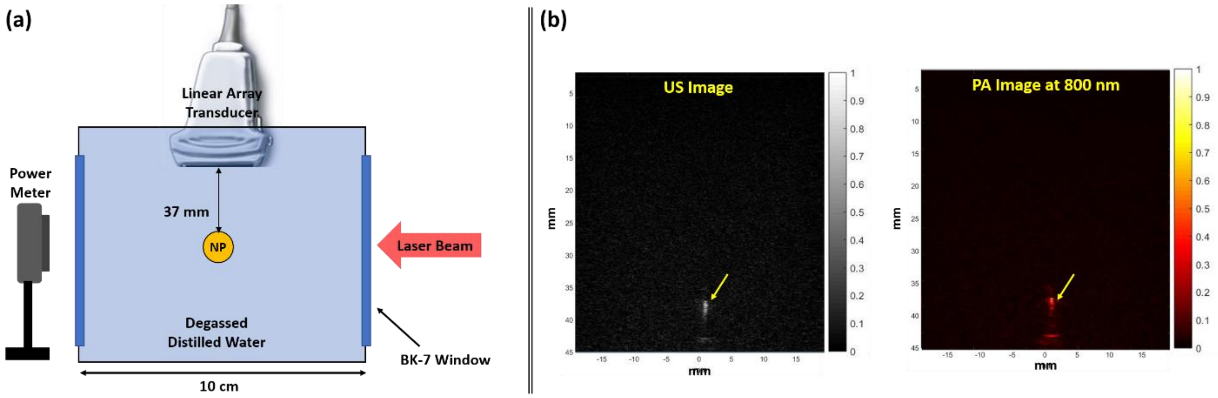

Figure 60: Experimental setup using linear array US transducer to image the gold NP tube. The power meter is used to measure the laser energy at each wavelength. (b) US and PA image results of the gold NP tube show the position of the tube, which is about 37 mm from the US transducer.

6.3.3 Imaging gold NPs embedded in breast fat by using omnidirectional full-ring US/PA tomography system

The main purpose of this study is to examine the efficiency of a full-ring illumination system for spectroscopic studies with human tissue. The glass tube, which filled with gold NPs, was placed inside the cone-shaped clear plastic sheet phantom field with centrifuged breast fat. The imaging tank was filled with the degassed distilled water, and then the phantom was positioned in the field of view of the ring US transducer (**Figure 61a**). About a 55 mm diameter oval-shaped cross-sectional slice was chosen to be scanned where the gold NP tube was minimally about 20 mm from the phantom's outer surface. At different wavelength range (680 nm to 900 nm), the phantom was illuminated with a ring laser beam that positioned 13 mm below the targeted cross-sectional slice (**Figure 61b**). In each wavelength, UST and PAT data were acquired and used to reconstruct the UST and PAT images. It is important to mention that the laser energy was measured at each wavelength to compensate the PA signal for energy loss.

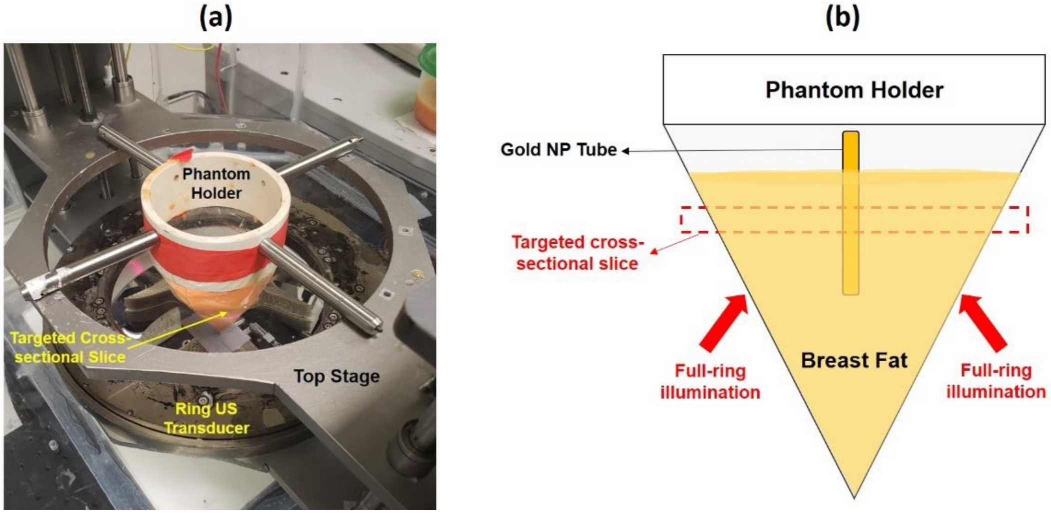

Figure 61: (a) Photograph of the breast fat phantom inside the imaging tank. The yellow arrow indicates the targeted cross-sectional slice located in front of the US elements. (b) The graph illustrates the breast fat phantom with gold NP tube.

6.4 Results and Discussion

6.4.1 Effect of optical parts and water medium on laser energy at near-infrared (NIR) wavelengths

By looking at **Figure 62a,** the measured laser energy was stable in all wavelengths at the first measuring point, where the measurement was around 100 mJ/pulse before the imaging tank. However, there was about a minimum of 65% energy loss created from the optical parts of the system. The possible reason for the massive energy loss is due to the quality of the optical components used in this prototype, especially the large parabolic reflector. Moreover, the graph illustrates a significant effect created from the water medium at certain wavelengths. From 680 nm to 720 nm, the water shows almost no effect on the laser energy. The energy starts declining with a different percentage from 740 nm to 920 nm. After 920 nm, the energy drops dramatically.

By utilizing the literature of the optical transmission in water medium at different wavelength [138], the optical transmission in water medium at wavelength range (500 to 1200 nm) in four different lengths (1, 5, 11, and 20 cm) was calculated **(Figure 62b)**. The graph shows that there is a positive relationship between the applied wavelength (> 600 nm) and the transmittance energy. In addition, there is also an inverse relationship between the length of the laser path in the water medium and the transmission energy.

For conclusion, it is essential to consider the energy loss of the laser beam created from optical components and water medium in each applied wavelength in any future studies required wavelength > 720 nm. In addition and with current tomography prototype, it is not efficient to perform studies that require wavelengths between 920 nm to 1000 nm.

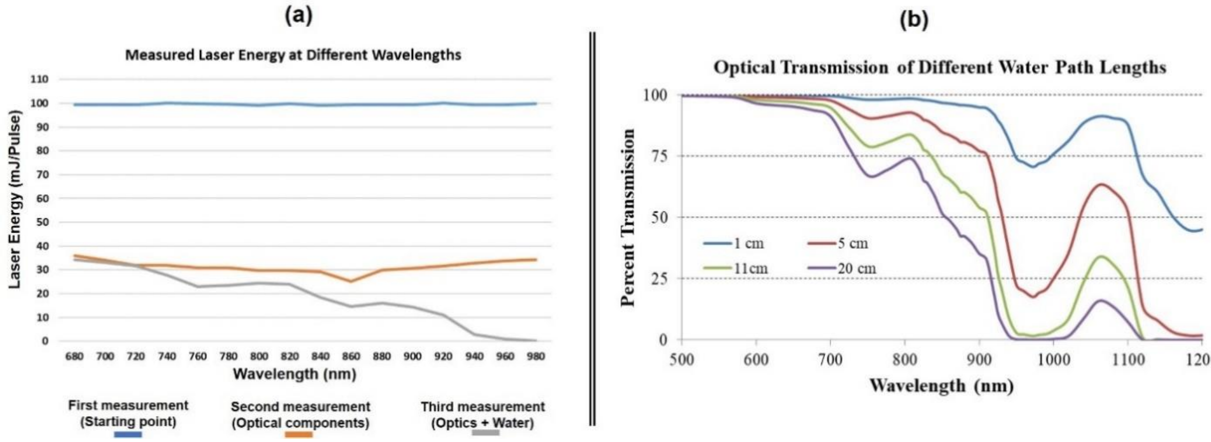

Figure 62: (a) The graph shows the three laser energy measurements used to study the effect of optical parts and water medium on energy at different wavelengths. (b) Calculated optical transmission in water as a function of wavelength at different path lengths.

6.4.2 Imaging gold nanoparticles in water medium using two different imaging systems

Figure 63 shows the UST and PAT images at three main wavelengths – 700 nm, 800 nm, and 900 nm. Each PAT image was normalized to the highest intensity value recorded in the image itself. As seen in **Figure 63**, both tubes are clearly shown in the UST image, while all PAT images show only the tube containing the gold NPs. At 800 nm PAT image, the PA signal created from the gold NP tube is stronger than signals at 700 nm and 900 nm images. The main reason for the high PA signal at 800 nm is because the peak absorption of the tested gold NP is at 808 nm (**Figure 59a**).

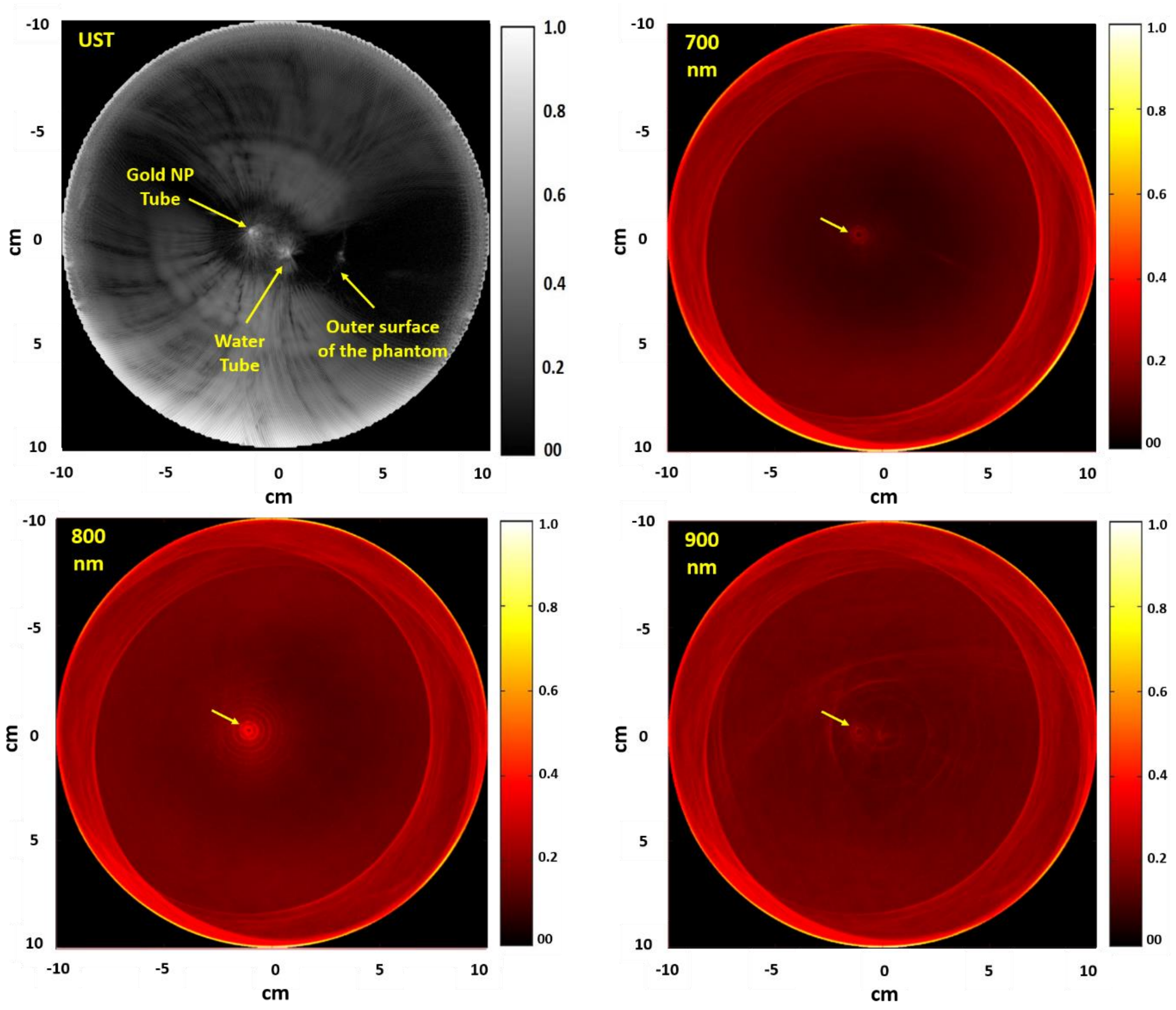

Figure 63: UST and PAT images of the phantom containing gold np and water tubes. The UST image shows both tubes while the PAT images at different wavelengths (700 nm, 800 nm, and 900 nm) display only the gold NP tube.

By using the UST image to define the ROI containing the gold NPs, the mean PA intensity of each PAT image was measured. After that, each measured intensity value was compensated by dividing the mean PA intensity value by the measured laser energy at each wavelength. Then, all mean PA intensities were normalized by dividing all intensity values by the highest PA intensity, which was at 800 nm. Finally, the graph that shows the normalized mean PA intensity to the applied wavelengths is plotted (**Figure 64**). Overall, there is an increment of the mean PA intensity from 680 nm to 800 nm. After that, the mean PA intensity curve declines from 800 nm to 900 nm.

Because the used sample has peak absorption at 808 nm wavelength, the expected peak value was shown at 800 nm wavelength. However, the shape of the curve does not exactly match the curve shown before in **Figure 59a,** especially at the edges. A possible reason of the broadening shape of the graph could be aggregation of the gold nanoparticles during the experiment, which is known to cause peak broadening. However, the results of the next experiment will help to investigate if the results was related to the sample or to the imaging system.

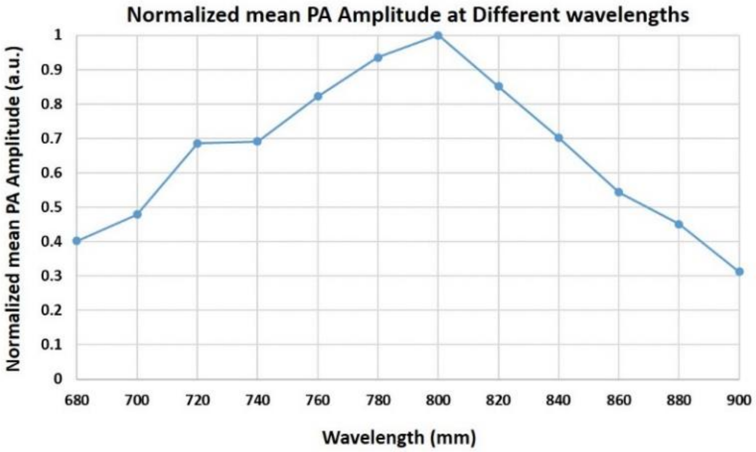

Figure 64: The normalized mean PA intensity of the gold NP tube at different wavelengths using omnidirectional full-ring US/PA tomography system. The peak intensity is shown at 800 nm wavelength.

In the second experiment that utilized a linear-array transducer, the mean PA intensity was measured at each PA image by averaging the PA intensity value at the ROI. After that, the mean intensity value for each wavelength was divided by its corresponding laser energy to compensate for energy. To normalize the results, all mean intensity values were divided by the maximum mean intensity value, which was at 800 nm. In the end, the graph that defines the relation between the applied wavelength and the mean PA intensity was drawn (**Figure 65**). In general, the chart looks similar to the chart seen earlier in **Figure 64**. The peak of the mean PA intensity is shown at the 800 nm wavelength, while the lowest intensity is observed at 900 nm. In addition, the mean PA intensity rose from 680 nm to 800 nm and then started to decline afterward to 900 nm. In conclusion, the gold NPs in the glass tube showed almost the same results in both experiments either by using omnidirectional full-ring US/PA tomography system or by utilizing US scanner equipped with a linear-array transducer.

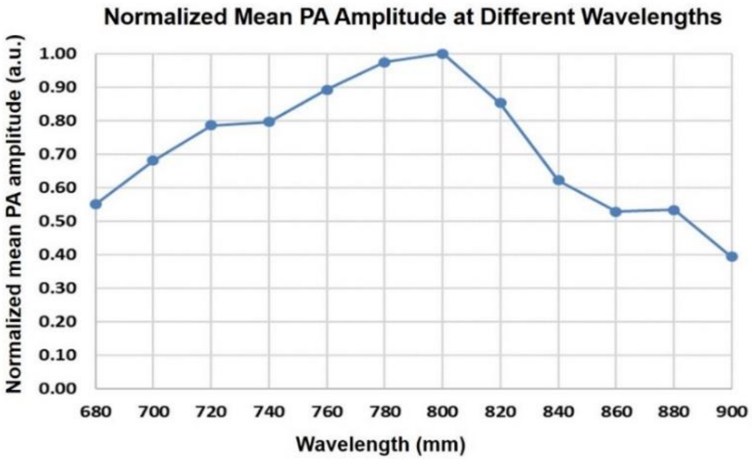

Figure 65: The normalized mean PA intensity of the gold NP tube at different wavelengths using a US engine equipped with a linear array transducer. The highest mean PA signal intensity is shown at 800 nm wavelength, while the lowest is at 900 nm.

6.4.3 Imaging gold NPs embedded in breast fat medium

Figure 66 demonstrates the UST and PAT images at three wavelengths – 720 nm, 800 nm, and 900 nm. Each image was normalized to the highest intensity value measured in the image. In the UST image, the gold NP tube is clearly shown in almost the center of the cross-section slice, which is about 20 mm from the phantom's outer surface. The results of the PAT images varied based on the wavelength used. In the PAT image acquired at 800 nm excitation wavelength, the gold NPs tube was obviously clear, while the 900 nm image showed no object. The main reason for not seeing the gold NPs tube because the fluence at 900 nm will be low due to the fact that the fat absorption at this wavelength is higher than 800 nm [67]. In addition, the peak absorption of the tested sample is low at 900 nm wavelength. Moreover, the fluence at 900 nm was low due to the energy loss created by the water medium.

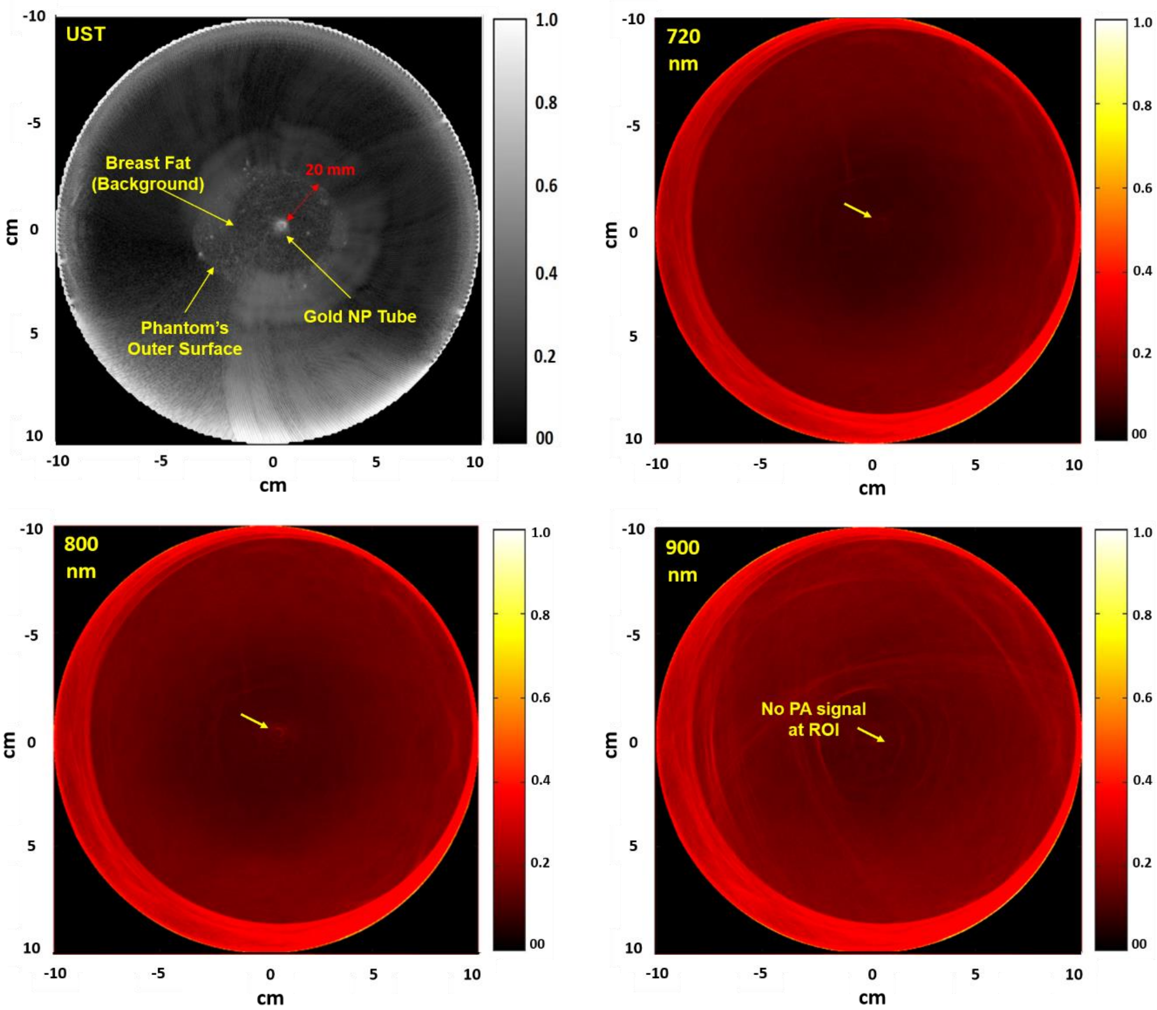

Figure 66: UST and three PAT results of the gold NP tube embedded inside breast fat tissue.

Same to previous experiments, the mean PA intensity of the ROI at each wavelength was measured and then compensated by dividing the mean PA intensity value by the measured laser energy at each wavelength. The ROI, which was expected to contain the gold NPs tube, was identified by using the UST image. All mean PA intensity was normalized by dividing all final intensities by the highest PA intensity value, which was at 800 nm wavelength.

Figure 67 shows a graph of the normalized mean PA intensity at applied wavelengths. The highest mean PA signals are shown at 800 nm and 780 nm wavelengths, respectively.

Overall, the graph shows an increment in intensity from 680 nm to 800 nm and then a decrement to 900 nm. However, many factors affect the final mean PA intensity results. First, the absorption coefficient of the background (breast fat) varies at each wavelength [67]. Variation of the absorption coefficient in different wavelengths will cause changes in laser fluence inside the scanned tissue. The second factor is the peak absorption of the targeted gold NPs, which is at 808 nm, will create different mean PA intensity.

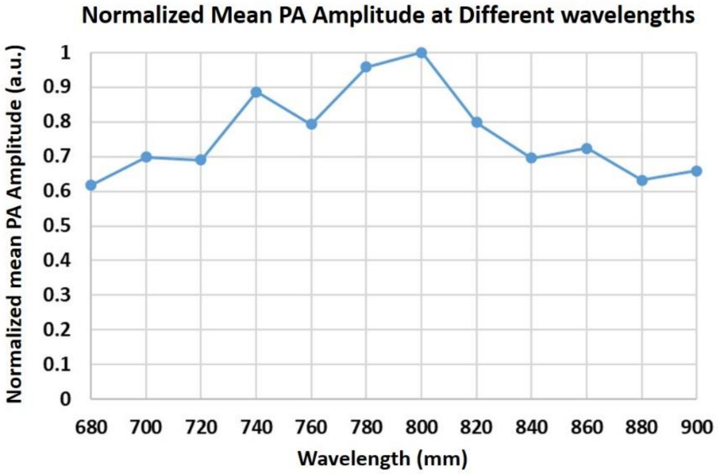

Figure 67: The normalized mean PA intensity of the gold NP tube, located inside breast fat phantom, at different wavelengths.

Because most of the PA images showed low contrast result in the gold NPs tube, it was essential to calculate the SNR and CNR of the PAT images in this experiment by using equations (4.1) and (4.2). As can be seen in **Figure 68**, the SNR and CNR showed the highest value at 800 nm wavelength. In the SNR, wavelengths below 720 nm and above 820 showed very low SNR. The same wavelengths show negative CNR values, which means the targeted object in the ROI is not detected, and the signal observed is from the background. In conclusion, the mean PA intensities of the ROI at wavelength range 720 nm to 840 nm will be considered as a result in this study because it was observed in PAT images. In addition, it was clear that targeted gold NP's shows high PA signal, SNR, and CNR at anticipated wavelength which is 800 nm.

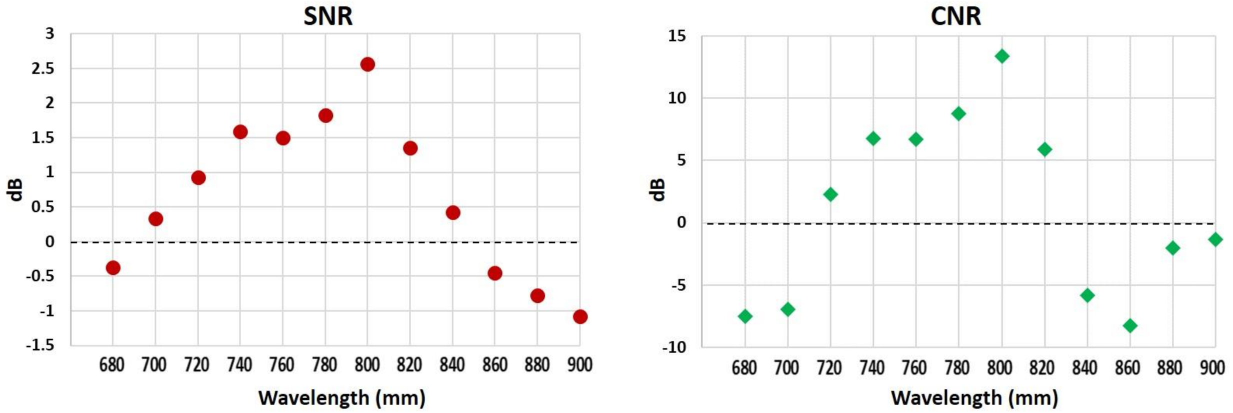

Figure 68: SNR and CNR of the mean PA amplitudes at the targeted cross-sectional slice of the breast fat phantom embedded with gold NPs inclusion.

6.5 Conclusion

Gold NPs with peak absorption coefficient at 808 nm was used as an exogenous contrast agent to evaluate the omnidirectional full-ring US/PA tomography system in using NIR wavelengths. In all studies, the mean intensity of the PA signal of the tested sample was at 800 nm wavelength, which matches the peak absorption coefficient of the sample. In addition, the mean PA amplitude graph, created by using a full-ring tomography system, was similar in shape to the other graph formed by the test using a US engine equipped with a linear array transducer. Moreover, the gold NPs was able to develop a clear PA signal at 20 mm depth of breast fat phantom. However, the quality of the optical parts in the system and the presence of water medium have shown a significant effect on laser energy during studies use wavelength range (680 nm to 980 nm). For this reason, the system requires some improvement in optics and imaging tank to minimize energy loss created by water and optics. This improvement will help to increase the fluence, which will then increase the penetration depths and the intensity of the PA signal. Also, it will give a large wavelength window to make the system able to perform future spectroscopic studies.

CHAPTER 7 - CONCLUSION AND FUTURE DIRECTION

7.1 Conclusion

The focus of this PhD thesis is to design, implement, optimize, and validate a mirror-based omnidirectional full-ring US/PA tomography system that could be used for tomographic breast screening. The main innovation of the proposed system is it uses an omnidirectional, all reflective, ring illumination method, which will help to enhance the PAT results. The unique of the proposed illumnation modality is its ability to provide flat illumination toward the center of the targeted cross-section of the breast, which will help to improve the penetration depth in the scanned slice. In addition, the full-ring beam creates a uniform distribution of the laser beam, which will result in a uniform PA signal generated from the scanned slice. Furthermore, the proposed optical design can distribute the laser energy on a large surface area which will enhance the use of higher laser energies yet remain below the maximum permissible exposure (MPE) of the ANSI limits. Additionally, full-ring illumination method shows high selectivity, so the beam energy will be directed to the targeted slice. Using optical mirrors (mirror-based system) to create a full-ring beam instead of using optical lenses will make the system suitable for spectroscopic studies and not have a chromatic aberration issue. Utilizing a ring US transducer with the proposed full-ring illumination system will improve the signal acquisition generated from the enclosed cross-sectional slice. In addition, the ability to adjust the position of the ring US transducer will help to cover most of the breast area, especially the parts close to the chest wall.

Chapter 1 in this thesis is an introductory chapter started with facts about breast cancer, the anatomy of the breast, and current imaging modalities of breast screening. Next, the principle of PA imaging was introduced, and the existing breast PAT systems were reviewed from the literature. The problem statement and proposed solution were presented at the end of the chapter. In chapter 2, preliminary studies performed by using array-based US/PA tomography system are discussed. The preliminary studies showed the great benefits of combining US and PA modalities in one imaging modality. Moreover, the studies gave a clear guideline of how to build a US/PA tomographic system and how to synchronize the US engine with a tunable laser source. After that, the first tomographic studies performed by utilizing a ring US transducer were shown. Lastly, the technical features of the first prototype (the omnidirectional full-ring US/PA tomography system) were introduced. In chapter 3, the benefits of the full-ring illumination were examined by using different mirror-based optical systems. The full-ring illumination showed a uniform PA signal and obvious penetration depth at different vertical layers of tissue-mimicking phantoms. In chapter 4, different illumination strategies (point and diffused beam illumination) were examined and compared to the full-ring illumination method. A uniform fluence, irrespective of the vertical depth of the scanned cross-section, was observed in the full-ring illumination method. Also, the preliminary studies indicate the optimal illumination position of the scanned object, which is in 10 to 15 mm below the scanned cross-section slice. In chapter 5, an introduction to the endogenous contrast agents was briefly discussed and explained. After that, a tissue-mimicking phantom was utilized to investigate the efficiency of the full-ring illumination in detecting different concentration blood samples. In addition, real human tissue (breast fat) was used as mimicked breast phantom to investigate the efficiency of the proposed US/PA tomography system in imaging light-absorbing objects such as graphite rods and human blood. In general, the proposed system, utilizing omnidirectional full-ring illumination, showed promising results in imaging angiogenesis samples such as different concentration blood, blood embedded in breast fat, and different dense objects, at remarkable depth and low fluence. Chapter 6 started with an introduction and brief literature about using exogenous contrast agents in breast cancer studies. Several preliminary experiments were performed in different phantoms containing a gold NPs tube to validate the proposed system and to define the possible limitations. The full-ring illumination showed noticeable penetration depths at the targeted wavelength of the scanned NPs sample. However, a major limitation was observed (i.e., laser energy loss) at specific wavelengths due to using a large amount of water (long laser path) in the imaging tank. This limitation should be solved in the future prototype by minimizing the path of the laser beam in the water tank.

7.2 Future Direction

The omnidirectional full-ring US/PA tomography system has been modified as a new imaging modality for breast screening. There are many possible modifications that could be done to improve the scanning procedure and full-ring illumination method to get optimum benefits. All possible future directions will be discussed in the next sections.

7.2.1 Improve the incident angle of the ring beam

In the current prototype, the ring beam is created by using a cone-shaped reflector and a parabolic reflector. As described in chapter 2, the current prototype can create a 39-degree incident angle on the scanned surface, which may limit the penetration depth. In a simulation study that was performed by using Monte Carlo simulations [139], a normal incident beam (90-degree) shows a better penetration depth than angled incident beam (45-degree). In this study, two different incident angles were simulated. The 90-degree incident angle is labeled as normal illumination, while the 45-degree incident angle is labeled the angled illumination (**Figure 69a**). The breast model used for all Monte Carlo light simulations was a 60 mm diameter cylindrical adipose tissue surrounded by 0.5 mm skin, as shown in **Figure 69b**. The illumination source had a wavelength of 740 nm, with a 3 mm beam-width. The adipose tissue and skin optical properties such as absorption (μa) scattering (μs) and anisotropy factor (g) used for the are given in **Figure 69c** [140-144].

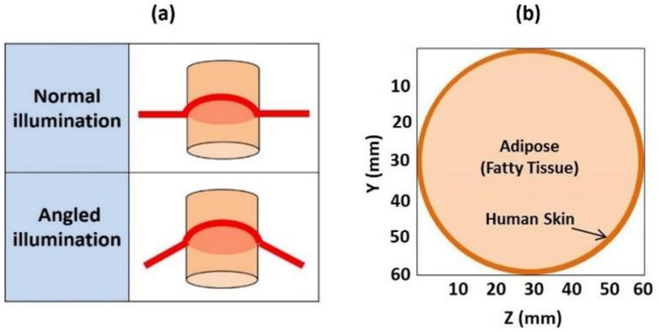

(c)

Tissue Type	Optical Properties		
	μ_a	μ_s	g
Adipose	0.2270	6.5	0.750
Skin	0.0451	20.7	0.790

Figure 69: (a) Illumination modes based on the incident angle used during the simulations. Red lines indicate the laser beam position with respect to the tissue. (b) The 60 mm horizontal cross-section of the breast tissue used for the Monte-Carlo simulations. (c) Optical properties (absorption: μa, scattering: μs, and anisotropy factor (g)) used for Monte-Carlo simulations.

Figure 70 plot the results of the Monte Carlo light simulations for energy density versus horizontal phantom depth. The normal illumination allows for greater imaging depth when compared to the angled illumination due to lower surface reflection and deeper scattering of photons. The simulation results motivate the need for improving the incident angle of the full-ring illumination for greater penetration depth in the targeted cross-sectional slice, so the more the incident angle gets close to a normal angle (90-degree), the better penetration depth happens.

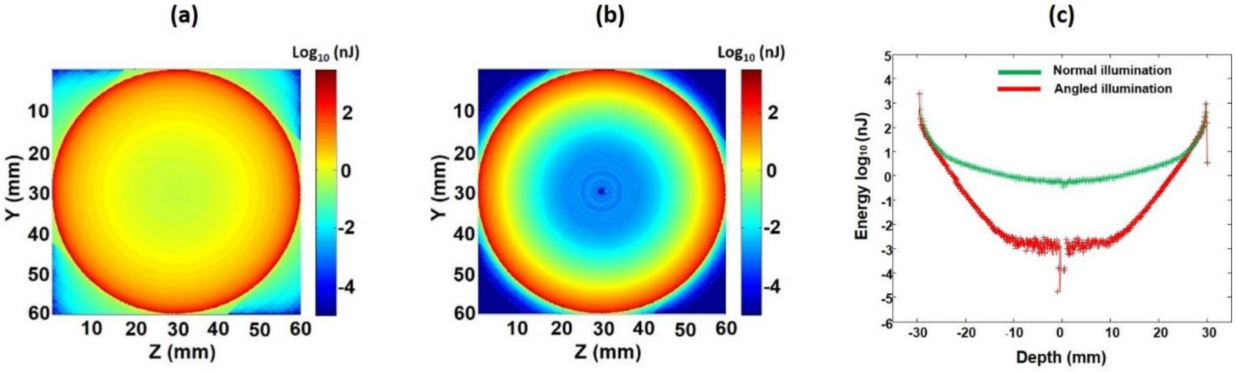

Figure 70: Cross-sectional fluence of the photons across the ZY plane in; (a) normal illumination and (b) angled illumination. (c) Plots of energy density with respect to tissue depth in normal and angled illumination.

The second prototype will consist mainly of one cone-shaped reflector, and two conical reflectors, as described earlier in **Figure 4**. The two-mirror prototype will enhance the incident angle from 39-degree in the current prototype to become 66-degree, so the efficiency of the incident-angle will be increased from 41% to 73%. This improvement is expected to show better penetration depth and raise the PA intensity. However, the two-mirror design, which introduced in chapter 1, needs modification to minimize using water medium. The modification will be discussed in the next section.

7.2.2 Minimize energy loss created by optics and water medium

As described earlier in chapter 2, the current prototype consists of a 45-degree mirror, cone-shaped reflector, parabolic reflector, and H-K9L glass. The cone-shaped reflector and parabolic reflector have a protected aluminum-coated surface, which has two major issues. The first issue is that each mirror can lose between 10% to 30% of laser energy at different NIR wavelengths. The second issue is the fact that a protected aluminum mirror has a low damage threshold, which limits the usage of high energy levels, compared to other coating materials. For example, the protected aluminum reflector has a damage threshold at around 300 mJ/cm^2 at 1064 nm wavelength (10 ns, 10 Hz pulsed laser) [6]. Using a protected silver will enhance the damage threshold number from 300 mJ/cm^2 to 3 J/cm^2 at the same wavelength and laser condition [7]. The calculated energy created from the optical components at different wavelengths was shown in **Figure 23.** There was about 25% to 51% energy loss created from optical components at different wavelengths. For the new prototype, the energy loss will be minimized by modifying the quality of the optical parts. The 45-degree mirror, cone-shaped reflector, conical reflectors are coated with protected silver material, which results in higher reflectance and damage threshold. The transmitted energy after the optical parts was calculated and showed that the average energy loss would be approximately 20% in the NIR wavelength window (**Figure 71**).

---

[6] https://www.thorlabs.com/newgrouppage9.cfm?objectgroup_id=264
[7] https://www.thorlabs.com/NewGroupPage9_PF.cfm?Guide=10&Category_ID=138&ObjectGroup_ID=903

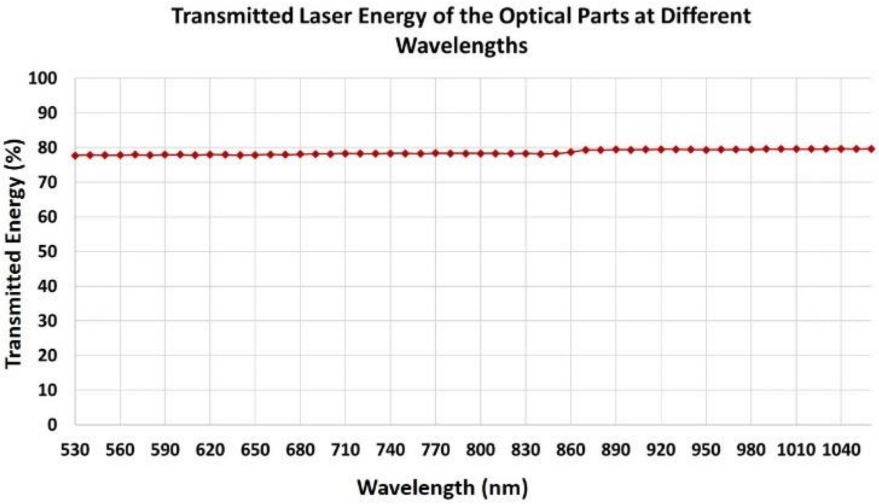

Figure 71: Transmitted laser energy at different wavelengths after modifying the optical parts of the omnidirectional US/PA tomography system.

In chapter 6, there was an observed laser energy loss at specific wavelengths caused by water in the imaging tank. In this regard, it is essential to modify the imaging tank in the next prototype by minimizing the use of water between the first and second conical reflectors. **Figure 72a** shows the new suggested design of the imaging tank and optical components. In this design, the ring US transducer will be placed inside a small cylindrical water tank made of a high-quality light transparent material such as BK-7 glass or thin layer clear plastic material. Unlike the first prototype and the first suggested two-mirror system (**Figure 4)**, the hollow cylindrical laser beam will travel in an air medium from the bottom conical reflector (R1) to the top conical reflector (R2). After that, the R2 will reflect the laser beam to the targeted cross-sectional slice in the imaging tank. The top stage will be used to vertically move the small size imaging tank, which includes the ring US transducer, to adjust the transducer position. The bottom stage will be used to adjust the optical system that includes a cone-shaped mirror, an optical window, and two ring-shaped conical reflectors. This modification will create four main advantages, which are:

1- It will minimize the use of water medium, which will prevent the laser energy loss that could be created at NIR wavelengths.

2- Having all optics in one cylindrical holder (**Figure 72b**) will make the optical system easy to assemble. In addition, it will prevent any beam deviation that could occur when beam travel between the R1 to R2 if the R1 and R2 misaligned during assembling.

3- Enhance the lifetime for the second conical reflector (R2) since it will not be used inside a water medium that may cause rust or cleanliness issues.

4- The incident angle of the ring beam will increase when the ring beam passes the outer surface of the new small tank to the targeted cross-sectional slice, which will be explained in the next paragraph.

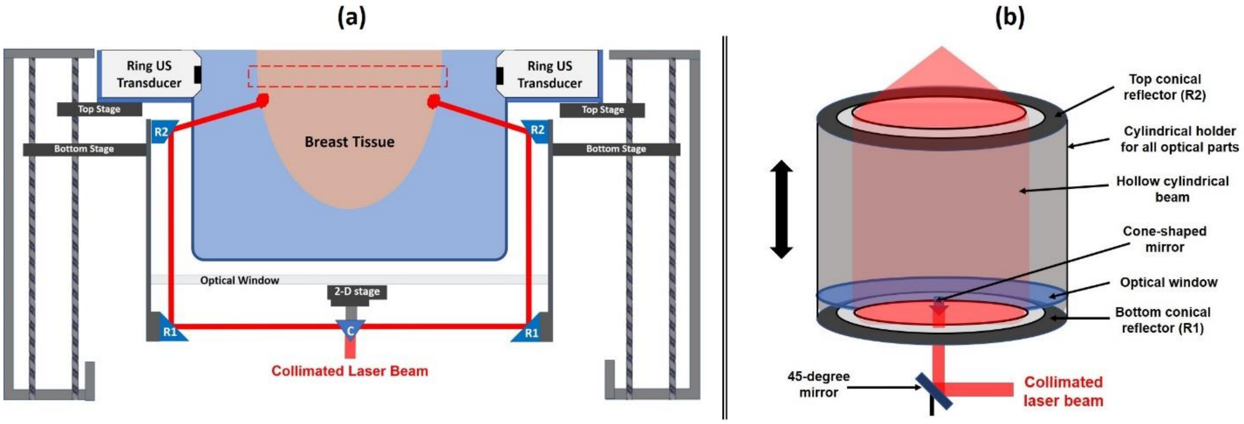

Figure 72: (a) 2-D graph of the suggested modification in the design of the omnidirectional full-ring US/PA tomography system. All optics will be mounted and aligned inside a cylindrical holder in air medium. The breast and the ring US transducer will be placed in the small water tank. (b) 3-D graph of the cylindrical holder that has all-optical parts. The holder can move up and down to adjust the position of the ring beam.

The incident angle of the laser beam will be changed once the ring beam enters the water tank due to the change in the index of refraction between air, glass, and water. In this case, the new incident angle is calculated based on Snell's law, which is:

$$n1\ sin\theta 1 = n2\ sin\theta 2 \tag{7.1}$$

where *n* represents the refractive index of the medium while θ is the angle of incidence. The new beam will pass in three different mediums, which are air, BK-7 glass, and water before it reaches the breast skin (**Figure 73**). The index of refraction at air is 1, while it is 1.52 at BK-7 glass and 1.33 for water [145, 146] at the targeted wavelength window (532 nm to 1000 nm). The final result shows that the incident angle will be increased from 66 degrees to about 72 degrees with respect to the skin surface. This enhancement will have a positive effect on PAT imaging, especially in enhancing penetration depth.

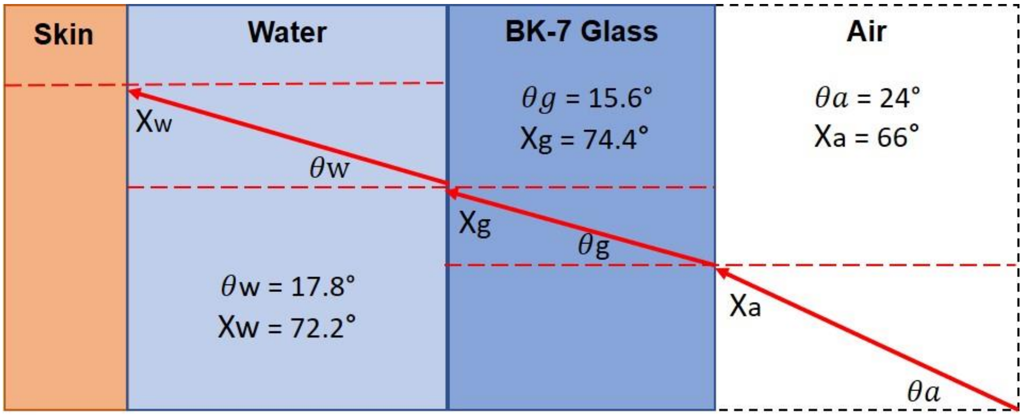

Figure 73: Diagram simulates the change in the beam incident angle at three different mediums.

7.2.3 Optimize the UST engine and the ring US transducer

The current UST engine has two main limitations that affect the imaging procedure and the quality of the UST/PAT images. The first limitation is related to the synchronization between the UST engine and the pulsed laser. As explained earlier in section 2.5.5, the current prototype is running by using a triggering signal created by the UST engine. This signal is amplified by a function generator to control the pulsed laser. This method is not practical because most of the PAT systems use the pulsed laser as a master clock to control the UST engine during PAT imaging. In addition, this method cannot perform continuous PAT imaging since the laser turns off after 0.5 seconds when the triggering signal stops during the translation movement of the ring

US transducer. For this reason, the new UST engine will have a trigger in port that allows the pulsed laser to control the UST engine during the PAT imaging.

The second limitation is related to the old ring US transducer that equipped with 256 elements. Some elements in the current ring US transducer are weak, while other elements are dead. This problem has reduced the quality of the UST and PAT images and it was clearly seen in many UST images (**Figure 74**). Enhancing the ring US transducer by increase the number of elements and the operating frequency will improve the image resolution and system operation.

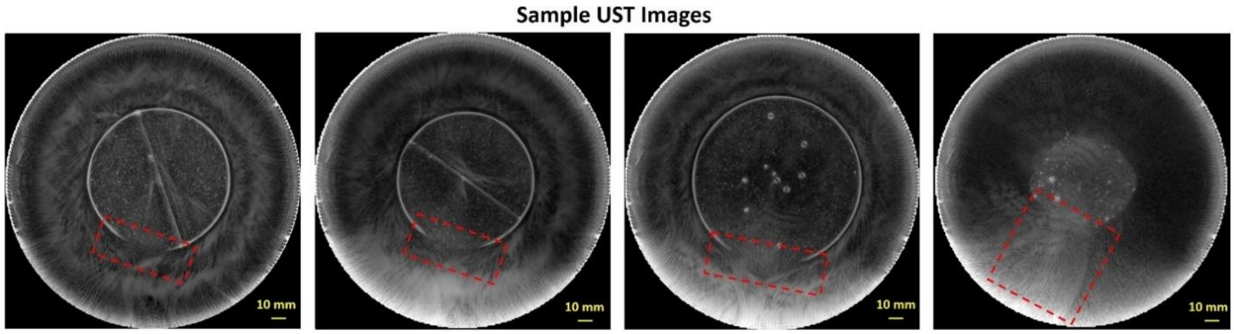

Figure 74: Sample UST images illustrate the observed problem in the ring US transducer used in the current prototype.

7.2.4 Fully compensated (optical/acoustical) quantitative PAT

A main limitation in most the PAT systems is the effect of penetration depth, which leads to the uneven distribution of light fluence. For this reason, it is not possible to equally compare the PA signals generated from various depths in breast tissue. In the current UST/PAT system, the compensation for the effects of light fluence as a function of depth and tissue heterogeneity is the main limitation and part of future developments. If the proposed system is modified and is able to compensate for fluence as a function of tissue heterogeneity and depth, then the compensated reconstructed PAT images will be able to provide more quantitative information. Using the current UST engine, which is composed of a ring US transducer, we can produce a tissue map by using acoustic information that is reconstructed, such as the acoustic attenuation (AA), speed of sound (SS), and reflection mode maps. As is known, the breast is a heterogeneous tissue that consists of fatty and fibroglandular components. The optical properties of the breast tissue are reported in literature, so by referring to the literature, it is possible to make a tissue map with the optical properties of the scanned cross-sectional slice. Having the tissue map as well as the geometry of the ring beam will help to compensate for fluence variation and for heterogeneous optical properties. By using Monte Carlo light simulations, the fluence map could be generated and then used with the uncompensated PAT image to create the fully compensated PAT image. This process will increase the accuracy of PAT imaging and will provide beneficial data about the relation between the intensity and depth of the PA signal. The process of the fully compensated quantitative PAT imaging is summarized in the block diagram shown in **Figure 75.**

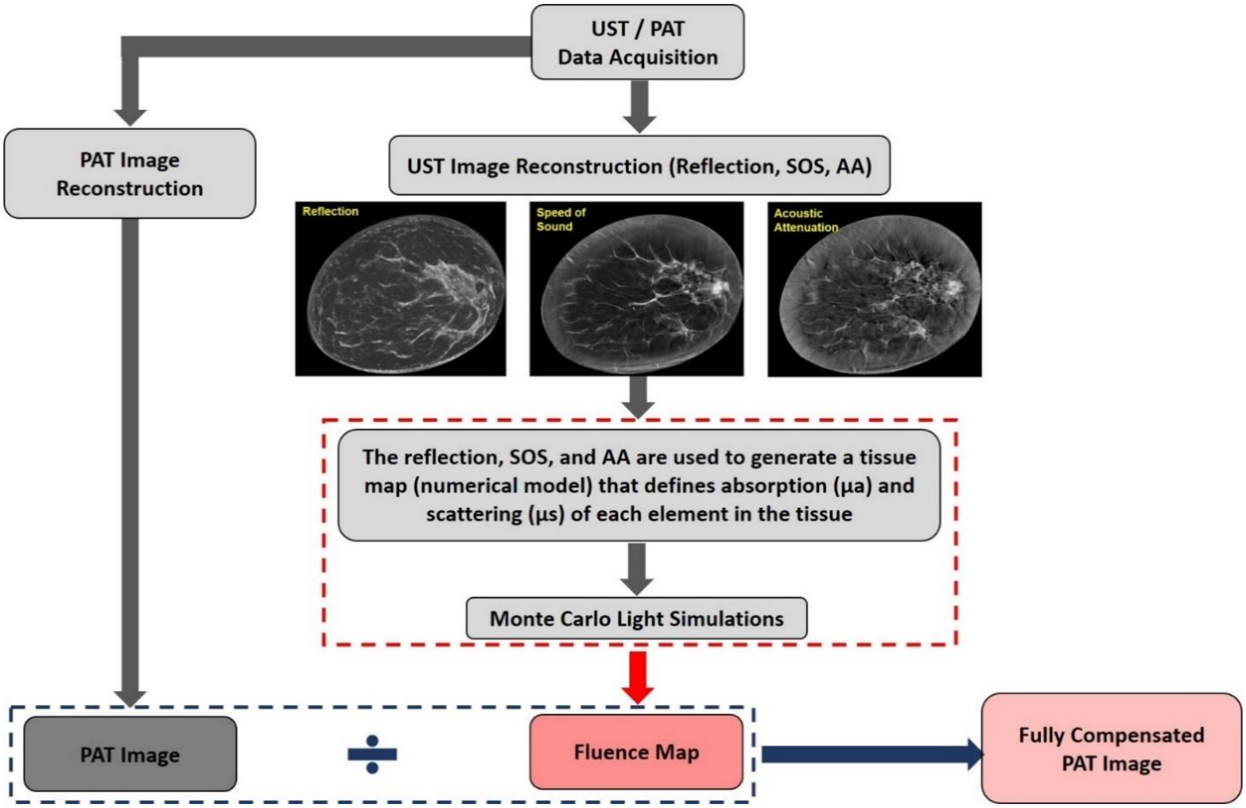

Figure 75: Block diagram of the fully compensated PAT imaging method utilizing the acoustical data generated by the UST system to make a fluence map that used with the light diffusion modeling to create the compensated PAT image which is compensated for the optical fluence. The breast UST images in the diagram are adapted and modified from [147].

APPENDIX A – PUBLICATION 1

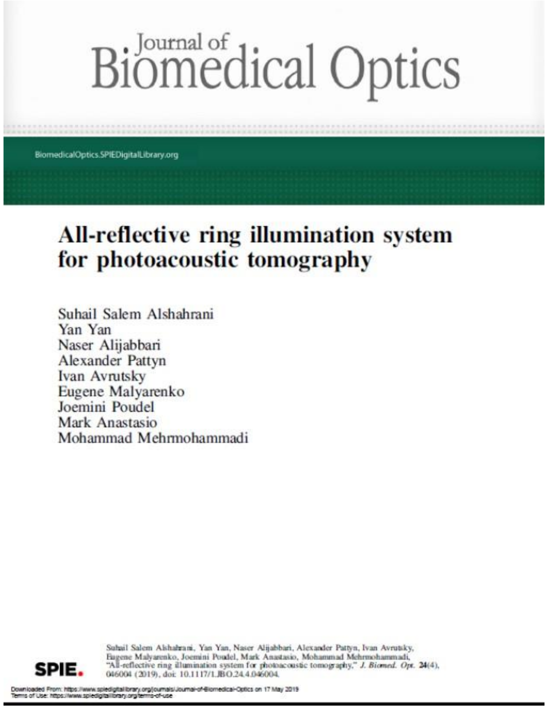

Journal of
Biomedical Optics

BiomedicalOptics.SPIEDigitalLibrary.org

All-reflective ring illumination system for photoacoustic tomography

Suhail Salem Alshahrani
Yan Yan
Naser Alijabbari
Alexander Pattyn
Ivan Avrutsky
Eugene Malyarenko
Joemini Poudel
Mark Anastasio
Mohammad Mehrmohammadi

SPIE.

Suhail Salem Alshahrani, Yan Yan, Naser Alijabbari, Alexander Pattyn, Ivan Avrutsky,
Eugene Malyarenko, Joemini Poudel, Mark Anastasio, Mohammad Mehrmohammadi,
"All-reflective ring illumination system for photoacoustic tomography," *J. Biomed. Opt.* **24**(4),
046004 (2019), doi: 10.1117/1.JBO.24.4.046004.

Downloaded From: https://www.spiedigitallibrary.org/journals/Journal-of-Biomedical-Optics on 17 May 2019
Terms of Use: https://www.spiedigitallibrary.org/terms-of-use

Journal of Biomedical Optics 24(4), 046004 (April 2019)

All-reflective ring illumination system for photoacoustic tomography

Suhail Salem Alshahrani,[a] Yan Yan,[a] Naser Alijabbari,[a] Alexander Pattyn,[a] Ivan Avrutsky,[b] Eugene Malyarenko,[c] Joemini Poudel,[d] Mark Anastasio,[d] and Mohammad Mehrmohammadi[a,b,c,*]
[a]Wayne State University, Department of Biomedical Engineering, Detroit, Michigan, United States
[b]Wayne State University, Department of Electrical and Computer Engineering, Detroit, Michigan, United States
[c]Barbara Ann Karmanos Cancer Institute, Detroit, Michigan, United States
[d]Washington University in St. Louis, Biomedical Engineering Department, St. Louis, Washington, United States

Abstract. Given that breast cancer is the second leading cause of cancer-related deaths among women in the United States, it is necessary to continue improving the sensitivity and specificity of breast imaging systems that diagnose breast lesions. Photoacoustic (PA) imaging can provide functional information during *in vivo* studies and can augment the structural information provided by ultrasound (US) imaging. A full-ring, all-reflective, illumination system for photoacoustic tomography (PAT) coupled to a full-ring US receiver is developed and tested. The US/PA tomography system utilizes a cone mirror and conical reflectors to optimize light delivery for PAT imaging and has the potential to image objects that are placed within the ring US transducer. The conical reflector used in this system distributes the laser energy over a circular cross-sectional area, thereby reducing the overall fluence. This, in turn, allows the operator to increase the laser energy achieving better cross-sectional penetration depth. A proof-of-concept design utilizing a single cone mirror and a parabolic reflector is used for imaging cylindrical phantoms with light-absorbing objects. For the given phantoms, it has been shown that there was no restriction in imaging a given targeted cross-sectional area irrespective of vertical depth, demonstrating the potential of mirror-based, ring-illuminated PAT system. In addition, the all-reflective ring illumination method shows a uniform PA signal across the scanned cross-sectional area. *© The Authors. Published by SPIE under a Creative Commons Attribution 4.0 Unported License. Distribution or reproduction of this work in whole or in part requires full attribution of the original publication, including its DOI.* [DOI: 10.1117/1.JBO.24.4.046004]

Keywords: full-ring illumination; omnidirectional; conical mirror; ultrasound tomography; photoacoustic tomography; ring ultrasound transducer.

Paper 190017R received Jan. 18, 2019; accepted for publication Apr. 8, 2019; published online Apr. 26, 2019.

1 Introduction

The combined ultrasound (US) and photoacoustic (PA) tomographic imaging system described in this paper has broad imaging applicability. With its full-ring US receiver and illumination source, one potential application could be breast imaging. Breast cancer is a common cancer type among women and is a major health concern affecting many lives worldwide. In 2018, it was estimated that the number of newly diagnosed breast cancer cases around the world will be above 2 million.[1] Mammography, magnetic resonance imaging (MRI), and B-mode US are three of the most common imaging modalities used for breast cancer screening,[2,3] and each has its unique shortcomings. Mammography has low sensitivity in detecting breast lesions in women with high-density breast tissue, which is critical since this population is considered to be at a higher risk of developing breast cancer.[3,4] MRI can be used in conjunction with mammography to detect breast tumors in dense breasts.[5,6] However, the availability and cost of MRI imaging restrict the accessibility of this modality. Conventional B-mode US is one of the most widely used medical imaging techniques for screening various types of human tissues, and it is a high-sensitivity, non-ionizing, and low-cost tool that can produce images in real time.[7,8] Yet its low specificity in breast screening can lead to unnecessary biopsies.[9,10] Therefore, it is essential to develop new or complementary breast cancer imaging modalities that minimize or eliminate the existing limitations.

Ultrasound tomography (UST), employing a ring-shaped US transducer, has shown promise for breast cancer screening.[11–15] Moreover, PA imaging has demonstrated potential in detecting carcinomas[16,17] and angiogenesis due to tumor growth.[18,19] The addition of photoacoustic tomography (PAT) to the UST imaging can enhance a physician's diagnostic capability by providing functional information about the tissue of interest. Moreover, PA imaging can be easily integrated with UST since the two modalities share the same acquisition hardware. Previous PA/PAT visualization tools[20–24] either suffer from the use of inefficient illumination methodologies or distort the breast tissue, reducing tissue circulation which may affect the PA results.

A significant challenge for PAT breast imaging is providing sufficient fluence for the desired cross section, while avoiding the maximum permissible exposure (MPE) limit for the tissue. For a full-ring illumination system, expanding the illumination area will help deliver a higher laser energy per pulse to the targeted cross-sectional slice, while keeping fluences below the American National Standards Institute limits.[25] For example, a 10-mm diameter laser beam, with 200-mJ/pulse energy will result in fluence of 253 $\mathrm{mJ/cm^2}$. However, using the cone-shaped reflector and the parabolic reflector to create the omnidirectional ring illumination pattern, with a 5-mm thickness and a 10-cm diameter cross-sectional area, will result in a fluence of 12.7 $\mathrm{mJ/cm^2}$. In this example, the fluence of the full-ring illumination system is about 20 times lower than that of direct

---

*Address all correspondence to Mohammad Mehrmohammadi, E-mail: mehr@wayne.edu

Downloaded From: https://www.spiedigitallibrary.org/journals/Journal-of-Biomedical-Optics on 17 May 2019
Terms of Use: https://www.spiedigitallibrary.org/terms-of-use

APPENDIX B – PUBLICATION 2

applied sciences

MDPI

Article

Photoacoustic Tomography with a Ring Ultrasound Transducer: A Comparison of Different Illumination Strategies

Naser Alijabbari [1,†], Suhail S. Alshahrani [1,†], Alexander Pattyn [1] and Mohammad Mehrmohammadi [1,2,3,*]

[1] Department of Biomedical Engineering, Wayne State University, Detroit, MI 48201, USA
[2] Department of Electrical and Computer Engineering, Wayne State University, Detroit, MI 48201, USA
[3] Barbara Ann Karmanos Cancer Institute, Detroit, MI 48201, USA
* Correspondence: mehr@wayne.edu
† Those authors are contributed equally to this work.

Received: 3 June 2019; Accepted: 27 July 2019; Published: 31 July 2019

check for updates

Featured Application: Biological diagnostic applications based on endogenous or exogenous chromophores and early breast cancer detection in dense tissue.

Abstract: Photoacoustic (PA) imaging is a methodology that uses the absorption of short laser pulses by endogenous or exogenous chromophores within human tissue, and the subsequent generation of acoustic waves acquired by an ultrasound (US) transducer, to form an image that can provide functional and molecular information. Amongst the various types of PA imaging, PA tomography (PAT) has been proposed for imaging pathologies such as breast cancer. However, the main challenge for PAT imaging is the deliverance of sufficient light energy horizontally through an imaging cross-section as well as vertically. In this study, three different illumination methods are compared for a full-ring ultrasound (US) PAT system. The three distinct illumination setups are full-ring, diffused-beam, and point source illumination. The full-ring system utilizes a cone mirror and parabolic reflector to create the ringed-shaped beam for PAT, while the diffuse scheme uses a light diffuser to expand the beam, which illuminates tissue-mimicking phantoms. The results indicate that the full-ring illumination is capable of providing a more uniform fluence irrespective of the vertical depth of the imaged cross-section, while the point source and diffused illumination methods provide a higher fluence at regions closer to the point of entry, which diminishes with depth. In addition, a set of experiments was conducted to determine the optimum position of ring-illumination with respect to the position of the acoustic detectors to achieve the highest signal-to-noise ratio.

Keywords: full-ring illumination; diffused-beam illumination; point source illumination; ultrasound tomography (UST); photoacoustic tomography (PAT)

---

1. Introduction

Breast cancer is a significant health problem not only in the United States but globally and was the second leading cause of cancer-related death in the United States in 2018 [1]. Mammography, MRI (Magnetic Resonance Imaging), and B-mode ultrasound are the three most common imaging modalities used for breast cancer screening [2,3]. However, each of these modalities has its own unique shortcomings. The sensitivity of mammography in detecting breast lesions decreases in women with high-density breast tissue, and high-density breasts are considered to be more at risk for developing breast cancer [3,4]. In dense breasts, MRI can be used in conjunction with breast mammography to detect breast tumors [5,6]. Nevertheless, the operational cost and availability of MRI imaging limit the

REFERENCES

1. Siegel, R.L., K.D. Miller, and A. Jemal, *Cancer statistics, 2019.* CA: a cancer journal for clinicians, 2019. **69**(1): p. 7-34.
2. World Health Organization. *Breast cancer*. 2018,May,09; Available from: https://www.who.int/cancer/prevention/diagnosis-screening/breast-cancer/en/.
3. American Cancer Society. *Cancer Facts & Figures 2019*. 2019; Available from: https://www.cancer.org/content/dam/cancer-org/research/cancer-facts-and-statistics/annual-cancer-facts-and-figures/2019/cancer-facts-and-figures-2019.pdf.
4. Boyd, N.F., et al., *Mammographic density and the risk and detection of breast cancer.* New England Journal of Medicine, 2007. **356**(3): p. 227-236.
5. Tamimi, R.M., et al., *Endogenous hormone levels, mammographic density, and subsequent risk of breast cancer in postmenopausal women.* Journal of the National Cancer Institute, 2007. **99**(15): p. 1178-1187.
6. DeSantis, C.E., et al., *Breast cancer statistics, 2017, racial disparity in mortality by state.* CA: a cancer journal for clinicians, 2017. **67**(6): p. 439-448.
7. Hendrick, R.E., J.A. Baker, and M.A. Helvie, *Breast cancer deaths averted over 3 decades.* Cancer, 2019.
8. McGuire, K.P., *Breast anatomy and physiology*, in *Breast Disease*. 2016, Springer. p. 1-14.
9. Pandya, S. and R.G. Moore, *Breast development and anatomy.* Clinical obstetrics and gynecology, 2011. **54**(1): p. 91-95.
10. Jesinger, R.A., *Breast anatomy for the interventionalist.* Techniques in vascular and interventional radiology, 2014. **17**(1): p. 3-9.

11. Santen, R.J. and R. Mansel, *Benign breast disorders.* New England Journal of Medicine, 2005. **353**(3): p. 275-285.

12. Galea, M., *Benign breast disorders.* Surgery (Oxford), 2019.

13. BREASTCANCER.ORG. *What Is Breast Cancer?* 2018; Available from: https://www.breastcancer.org/symptoms/understand_bc/what_is_bc.

14. Britta Weigelt, F.C.G., Jorge S. Reis-Filho, *Histological types of breast cancer: How special are they?* Molecular Oncology, 2010 Pages **4**(3): p. 192–208.

15. Harmer, V., *Breast cancer nursing care and management*. 2011: Wiley Online Library.

16. Shusma C. Doebar, E.C.v.d.B., Linetta B. Koppert, Agnes Jager, Margreet. H. A. Baaijens, Inge-Marie A. M. Obdeijn, Carolien H. M. van Deurzen, *Extent of ductal carcinoma in situ according to breast cancer subtypes: a population-based cohort study.* 2016. **158**(1): p. 179-187.

17. Li, C., D. Uribe, and J. Daling, *Clinical characteristics of different histologic types of breast cancer.* British journal of cancer, 2005. **93**(9): p. 1046.

18. Li, L., et al., *Attributable causes of breast cancer and ovarian cancer in china: reproductive factors, oral contraceptives and hormone replacement therapy.* Chinese Journal of Cancer Research, 2012. **24**(1): p. 9-17.

19. Rodrigo Arrangoiz, P.P., Holly Dushkin, Jeffrey M. Farma, *Case report and literature review: Metastatic lobular carcinoma of the breast an unusual presentation.* International Journal of Surgery Case Reports, 2011 **2**(8): p. 301–305.

20. Kuhl, C.K., et al., *Mammography, breast ultrasound, and magnetic resonance imaging for surveillance of women at high familial risk for breast cancer.* Journal of clinical oncology, 2005. **23**(33): p. 8469-8476.

21. Elmore, J.G., et al., *Screening for breast cancer.* Jama, 2005. **293**(10): p. 1245-1256.

22. Amano, S., et al., *In vivo comparison of PET and SPECT radiopharmaceuticals in detecting breast cancer.* The Journal of Nuclear Medicine, 1998. **39**(8): p. 1424.

23. Yutani, K., et al., *Comparison of FDG-PET with MIBI-SPECT in the detection of breast cancer and axillary lymph node metastasis.* Journal of computer assisted tomography, 2000. **24**(2): p. 274-280.

24. Shiraishi, A., *Current state of digital mammography.* Breast Cancer, 2008. **15**(3): p. 194-199.

25. Calonge, N., et al., *Screening for breast cancer.* Annals of internal medicine, 2009. **151**(10): p. 716-726.

26. Huzarski, T., et al., *Screening with magnetic resonance imaging, mammography and ultrasound in women at average and intermediate risk of breast cancer.* Hereditary cancer in clinical practice, 2017. **15**(1): p. 4.

27. Radiology, A.C.o., *ACR breast imaging reporting and data system.* Breast Imaging Atlas, 4th edn., Reston, VA, USA, 2003.

28. Sprague, B.L., et al., *Prevalence of mammographically dense breasts in the United States.* JNCI: Journal of the National Cancer Institute, 2014. **106**(10).

29. Adler, D.D., et al., *Doppler ultrasound color flow imaging in the study of breast cancer: preliminary findings.* Ultrasound in medicine & biology, 1990. **16**(6): p. 553-559.

30. Berg, W.A., et al., *Diagnostic accuracy of mammography, clinical examination, US, and MR imaging in preoperative assessment of breast cancer.* Radiology, 2004. **233**(3): p. 830-849.

31. Lehman, C.D., et al., *Screening women at high risk for breast cancer with mammography and magnetic resonance imaging.* Cancer, 2005. **103**(9): p. 1898-1905.

32. Kriege, M., et al., *Efficacy of MRI and mammography for breast-cancer screening in women with a familial or genetic predisposition.* New England Journal of Medicine, 2004. **351**(5): p. 427-437.

33. Kuhl, C.K. and H.H. Schild, *Dynamic image interpretation of MRI of the breast.* Journal of Magnetic Resonance Imaging, 2000. **12**(6): p. 965-974.

34. Jensen, J.A., *Medical ultrasound imaging.* Progress in biophysics and molecular biology, 2007. **93**(1): p. 153-165.

35. Gordon, P.B. and S.L. Goldenberg, *Malignant breast masses detected only by ultrasound. A retrospective review.* Cancer, 1995. **76**(4): p. 626-630.

36. Soo, M.S., J.A. Baker, and E.L. Rosen, *Sonographic detection and sonographically guided biopsy of breast microcalcifications.* American Journal of Roentgenology, 2003. **180**(4): p. 941-948.

37. Bassett, L. and C. Kimme-Smith. *Breast sonography: technique, equipment, and normal anatomy*. in *Seminars in ultrasound, CT, and MR*. 1989.

38. Kremkau, F.W., *Diagnostic ultrasound: principles and instruments*. 2001: WB Saunders Company.

39. Nothacker, M., et al., *Early detection of breast cancer: benefits and risks of supplemental breast ultrasound in asymptomatic women with mammographically dense breast tissue. A systematic review.* BMC cancer, 2009. **9**(1): p. 335.

40. Denis, M., et al., *Comb-push ultrasound shear elastography of breast masses: Initial results show promise.* PloS one, 2015. **10**(3): p. e0119398.

41. Madjar, H., *Role of breast ultrasound for the detection and differentiation of breast lesions.* Breast Care, 2010. **5**(2): p. 109-114.

42. Corsetti, V., et al., *Breast screening with ultrasound in women with mammography-negative dense breasts: evidence on incremental cancer detection and false positives, and associated cost.* European journal of cancer, 2008. **44**(4): p. 539-544.
43. Garra, B.S., et al., *Elastography of breast lesions: initial clinical results.* Radiology, 1997. **202**(1): p. 79-86.
44. Mehrmohammadi, M., et al., *Preliminary in vivo breast vibro-acoustography results with a quasi-2-D array transducer: a step forward toward clinical applications.* Ultrasound in Medicine and Biology, 2014. **40**(12): p. 2819-2829.
45. Duric, N., et al. *Breast imaging with the SoftVue imaging system: First results*. in *SPIE Medical Imaging*. 2013. International Society for Optics and Photonics.
46. Duric, N., et al., *Detection of breast cancer with ultrasound tomography: First results with the Computed Ultrasound Risk Evaluation (CURE) prototype.* Medical physics, 2007. **34**(2): p. 773-785.
47. Duric, N., et al., *Development of ultrasound tomography for breast imaging: Technical assessment.* Medical Physics, 2005. **32**(5): p. 1375-1386.
48. Ranger, B., et al., *Breast ultrasound tomography versus MRI for clinical display of anatomy and tumor rendering: preliminary results.* American Journal of Roentgenology, 2012. **198**(1): p. 233-239.
49. Duric, N., et al. *Breast imaging with SoftVue: initial clinical evaluation*. in *Proc. SPIE*. 2014.
50. O'Flynn, E.A., et al., *Ultrasound Tomography Evaluation of Breast Density: A Comparison With Noncontrast Magnetic Resonance Imaging.* Investigative radiology, 2017. **52**(6): p. 343.

51. Pratt, R.G., et al. *Sound-speed and attenuation imaging of breast tissue using waveform tomography of transmission ultrasound data*. in *Medical Imaging 2007: Physics of Medical Imaging*. 2007. International Society for Optics and Photonics.

52. Li, C., N. Duric, and L. Huang. *Clinical breast imaging using sound-speed reconstructions of ultrasound tomography data*. in *Medical Imaging 2008: Ultrasonic Imaging and Signal Processing*. 2008. International Society for Optics and Photonics.

53. Evans, A., et al., *Differentiating benign from malignant solid breast masses: value of shear wave elastography according to lesion stiffness combined with greyscale ultrasound according to BI-RADS classification.* British journal of cancer, 2012. **107**(2): p. 224.

54. Beard, P., *Biomedical photoacoustic imaging.* Interface focus, 2011: p. rsfs20110028.

55. Mallidi, S., G.P. Luke, and S. Emelianov, *Photoacoustic imaging in cancer detection, diagnosis, and treatment guidance.* Trends in biotechnology, 2011. **29**(5): p. 213-221.

56. Mehrmohammadi, M., et al., *Photoacoustic imaging for cancer detection and staging.* Current molecular imaging, 2013. **2**(1): p. 89-105.

57. Kruger, R.A., et al., *Photoacoustic angiography of the breast.* Medical physics, 2010. **37**(11): p. 6096-6100.

58. Menke, J., *Photoacoustic breast tomography prototypes with reported human applications.* European radiology, 2015. **25**(8): p. 2205-2213.

59. Luke, G.P., D. Yeager, and S.Y. Emelianov, *Biomedical applications of photoacoustic imaging with exogenous contrast agents.* Annals of biomedical engineering, 2012. **40**(2): p. 422-437.

60. Wang, L.V., *Prospects of photoacoustic tomography.* Medical physics, 2008. **35**(12): p. 5758-5767.

61. Karpiouk, A.B., B. Wang, and S.Y. Emelianov, *Development of a catheter for combined intravascular ultrasound and photoacoustic imaging.* Review of Scientific Instruments, 2010. **81**(1): p. 014901.

62. Karpiouk, A.B., et al., *Combined ultrasound and photoacoustic imaging to detect and stage deep vein thrombosis: phantom and ex vivo studies.* Journal of biomedical optics, 2008. **13**(5): p. 054061-054061-8.

63. Homan, K., et al. *Combined ultrasound and photoacoustic imaging of pancreatic cancer using nanocage contrast agents*. in *Proc. SPIE*. 2009.

64. Valluru, K.S. and J.K. Willmann, *Clinical photoacoustic imaging of cancer.* Ultrasonography, 2016. **35**(4): p. 267.

65. Rundqvist, H. and R. Johnson, *Tumour oxygenation: implications for breast cancer prognosis.* Journal of internal medicine, 2013. **274**(2): p. 105-112.

66. Zhong, H., et al., *Overexpression of hypoxia-inducible factor 1α in common human cancers and their metastases.* Cancer research, 1999. **59**(22): p. 5830-5835.

67. Wang, B., et al., *Detection of lipid in atherosclerotic vessels using ultrasound-guided spectroscopic intravascular photoacoustic imaging.* Optics express, 2010. **18**(5): p. 4889-4897.

68. Laufer, J., et al., *Quantitative spatially resolved measurement of tissue chromophore concentrations using photoacoustic spectroscopy: application to the measurement of blood oxygenation and haemoglobin concentration.* Physics in medicine and biology, 2006. **52**(1): p. 141.

69. Wang, L.V. and S. Hu, *Photoacoustic tomography: in vivo imaging from organelles to organs.* Science, 2012. **335**(6075): p. 1458-1462.

70. Zhang, H.F., et al., *Functional photoacoustic microscopy for high-resolution and noninvasive in vivo imaging.* Nature biotechnology, 2006. **24**(7): p. 848.

71. Taroni, P., et al., *Non-invasive optical estimate of tissue composition to differentiate malignant from benign breast lesions: A pilot study.* Scientific reports, 2017. **7**: p. 40683.

72. Siphanto, R., et al., *Serial noninvasive photoacoustic imaging of neovascularization in tumor angiogenesis.* Optics express, 2005. **13**(1): p. 89-95.

73. Wilson, K.E., et al., *Multiparametric spectroscopic photoacoustic imaging of breast cancer development in a transgenic mouse model.* Theranostics, 2014. **4**(11): p. 1062.

74. Brahimi-Horn, M.C., J. Chiche, and J. Pouysségur, *Hypoxia and cancer.* Journal of molecular medicine, 2007. **85**(12): p. 1301-1307.

75. Zhang, H.F., et al., *Imaging of hemoglobin oxygen saturation variations in single vessels in vivo using photoacoustic microscopy.* Applied physics letters, 2007. **90**(5): p. 053901.

76. Karakashev, S.V. and M.J. Reginato, *Progress toward overcoming hypoxia-induced resistance to solid tumor therapy.* Cancer management and research, 2015. **7**: p. 253.

77. Oraevsky, A.A., et al. *Laser optoacoustic imaging of breast cancer in vivo*. in *Proc. SPIE*. 2001.

78. Xu, R.X., et al., *A prospective pilot clinical trial evaluating the utility of a dynamic near-infrared imaging device for characterizing suspicious breast lesions.* Breast Cancer Research, 2007. **9**(6): p. R88.

79. Xu, M. and L.V. Wang, *Photoacoustic imaging in biomedicine.* Review of scientific instruments, 2006. **77**(4): p. 041101.

80. Nie, L. and X. Chen, *Structural and functional photoacoustic molecular tomography aided by emerging contrast agents.* Chemical Society Reviews, 2014. **43**(20): p. 7132-7170.

81. Galanzha, E.I., et al., *In vivo fiber-based multicolor photoacoustic detection and photothermal purging of metastasis in sentinel lymph nodes targeted by nanoparticles.* Journal of biophotonics, 2009. **2**(8-9): p. 528-539.

82. Xie, Z., et al., *Combined photoacoustic and acoustic imaging of human breast specimens in the mammographic geometry.* Ultrasound in medicine & biology, 2013. **39**(11): p. 2176-2184.

83. Piras, D., et al., *Photoacoustic imaging of the breast using the twente photoacoustic mammoscope: present status and future perspectives.* IEEE Journal of Selected Topics in Quantum Electronics, 2009. **16**(4): p. 730-739.

84. Heijblom, M., et al. *Imaging breast lesions using the Twente Photoacoustic Mammoscope: Ongoing clinical experience*. in *Photons Plus Ultrasound: Imaging and Sensing 2012*. 2012. International Society for Optics and Photonics.

85. Manohar, S., et al. *Region-of-interest breast images with the Twente Photoacoustic Mammoscope (PAM)*. in *Photons Plus Ultrasound: Imaging and Sensing 2007: The Eighth Conference on Biomedical Thermoacoustics, Optoacoustics, and Acousto-optics*. 2007. International Society for Optics and Photonics.

86. Manohar, S., et al., *The Twente Photoacoustic Mammoscope: system overview and performance.* Physics in Medicine & Biology, 2005. **50**(11): p. 2543.

87. Ermilov, S.A., et al., *Laser optoacoustic imaging system for detection of breast cancer.* Journal of biomedical optics, 2009. **14**(2): p. 024007-024007-14.

88. Kruger, R.A., et al., *Dedicated 3D photoacoustic breast imaging.* Medical physics, 2013. **40**(11): p. 113301.

89. Lin, L., et al., *Single-breath-hold photoacoustic computed tomography of the breast.* Nature communications, 2018. **9**(1): p. 2352.

90. Lin, L., et al. *Clinical photoacoustic computed tomography of the human breast in vivo within a single breath hold*. in *Photons Plus Ultrasound: Imaging and Sensing 2018*. 2018. International Society for Optics and Photonics.

91. Standard, A., *Z136. 1. American national standard for the safe use of lasers. American National Standards Institute.* Inc., New York, 1993.

92. Deng, Z., et al., *Acoustically penetrable optical reflector for photoacoustic tomography.* Journal of Biomedical Optics, 2013. **18**(7): p. 070503.

93. Deng, Z., W. Li, and C. Li, *Slip-ring-based multi-transducer photoacoustic tomography system.* Optics letters, 2016. **41**(12): p. 2859-2862.

94. Xia, J., et al., *Whole-body ring-shaped confocal photoacoustic computed tomography of small animals in vivo.* Journal of biomedical optics, 2012. **17**(5): p. 050506.

95. Li, L., et al., *Single-impulse panoramic photoacoustic computed tomography of small-animal whole-body dynamics at high spatiotemporal resolution.* Nature biomedical engineering, 2017. **1**(5): p. 0071.

96. Righetti, R., J. Ophir, and P. Ktonas, *Axial resolution in elastography.* Ultrasound in medicine & biology, 2002. **28**(1): p. 101-113.

97. Righetti, R., S. Srinivasan, and J. Ophir, *Lateral resolution in elastography.* Ultrasound in medicine & biology, 2003. **29**(5): p. 695-704.

98. Wang, K. and M.A. Anastasio, *Photoacoustic and thermoacoustic tomography: image formation principles*, in *Handbook of Mathematical Methods in Imaging*. 2011, Springer. p. 781-815.

99. Sidky, E.Y. and X. Pan, *Image reconstruction in circular cone-beam computed tomography by constrained, total-variation minimization.* Physics in medicine and biology, 2008. **53**(17): p. 4777.

100. Alshahrani, S.S., et al., *All-reflective ring illumination system for photoacoustic tomography.* Journal of biomedical optics, 2019. **24**(4): p. 046004.

101. Li, C., et al. *Breast imaging using waveform attenuation tomography*. in *Medical Imaging 2017: Ultrasonic Imaging and Tomography*. 2017. International Society for Optics and Photonics.

102. Xu, M. and L.V. Wang, *Universal back-projection algorithm for photoacoustic computed tomography.* Physical Review E, 2005. **71**(1): p. 016706.

103. Alijabbari, N., et al., *Photoacoustic Tomography with a Ring Ultrasound Transducer: A Comparison of Different Illumination Strategies.* Applied Sciences, 2019. **9**(15): p. 3094.

104. Maggi, L., et al. *Ultrasonic Attenuation and Speed in phantoms made of PVCP and Evaluation of acoustic and thermal properties of ultrasonic phantoms made of polyvinyl chloride-plastisol (PVCP)*. in *IWBBIO*. 2013.

105. Brown, J.Q., et al., *Quantitative optical spectroscopy: a robust tool for direct measurement of breast cancer vascular oxygenation and total hemoglobin content in vivo.* Cancer research, 2009. **69**(7): p. 2919-2926.

106. Brown, J.M. and W.R. Wilson, *Exploiting tumour hypoxia in cancer treatment.* Nature reviews. Cancer, 2004. **4**(6): p. 437.

107. Lao, Y., et al., *Noninvasive photoacoustic imaging of the developing vasculature during early tumor growth.* Physics in medicine and biology, 2008. **53**(15): p. 4203.

108. Zijlstra, W., A. Buursma, and W. Meeuwsen-Van der Roest, *Absorption spectra of human fetal and adult oxyhemoglobin, de-oxyhemoglobin, carboxyhemoglobin, and methemoglobin.* Clinical chemistry, 1991. **37**(9): p. 1633-1638.

109. Zijlstra, W. and A. Buursma, *Spectrophotometry of hemoglobin: absorption spectra of bovine oxyhemoglobin, deoxyhemoglobin, carboxyhemoglobin, and methemoglobin.*

Comparative Biochemistry and Physiology Part B: Biochemistry and Molecular Biology, 1997. **118**(4): p. 743-749.

110. Heijblom, M., et al., *Imaging tumor vascularization for detection and diagnosis of breast cancer.* Technology in cancer research & treatment, 2011. **10**(6): p. 607-623.

111. Heijblom, M., et al. *Photoacoustic imaging of breast tumor vascularization: a comparison with MRI and histopathology*. in *European Conference on Biomedical Optics*. 2013. Optical Society of America.

112. Heijblom, M., et al., *Photoacoustic image patterns of breast carcinoma and comparisons with Magnetic Resonance Imaging and vascular stained histopathology.* Scientific reports, 2015. **5**: p. srep11778.

113. Lungu, G.F., et al., *In vivo imaging and characterization of hypoxia-induced neovascularization and tumor invasion.* International journal of oncology, 2007. **30**(1): p. 45-54.

114. Jacques, S.L., *Optical properties of biological tissues: a review.* Physics in Medicine & Biology, 2013. **58**(11): p. R37.

115. Alcantara, D., et al., *Molecular imaging of breast cancer: present and future directions.* Frontiers in chemistry, 2014. **2**.

116. Giuliano, M., M.V. Trivedi, and R. Schiff, *Bidirectional crosstalk between the estrogen receptor and human epidermal growth factor receptor 2 signaling pathways in breast cancer: molecular basis and clinical implications.* Breast Care, 2013. **8**(4): p. 256-262.

117. Zhang, T., et al., *Targeted nanodiamonds as phenotype-specific photoacoustic contrast agents for breast cancer.* Nanomedicine, 2015. **10**(4): p. 573-587.

118. Saha Roy, S. and R.K. Vadlamudi, *Role of estrogen receptor signaling in breast cancer metastasis.* International journal of breast cancer, 2011. **2012**.

119. Zhang, M.H., et al., *Estrogen receptor-positive breast cancer molecular signatures and therapeutic potentials.* Biomedical reports, 2014. **2**(1): p. 41-52.

120. Nakamura, Y., et al., *Nanodrug delivery: is the enhanced permeability and retention effect sufficient for curing cancer?* Bioconjugate chemistry, 2016. **27**(10): p. 2225-2238.

121. Kobayashi, H., R. Watanabe, and P.L. Choyke, *Improving conventional enhanced permeability and retention (EPR) effects; what is the appropriate target?* Theranostics, 2014. **4**(1): p. 81.

122. Wilson, K.E., T.Y. Wang, and J.K. Willmann, *Acoustic and photoacoustic molecular imaging of cancer.* Journal of Nuclear Medicine, 2013. **54**(11): p. 1851-1854.

123. Nakai, K., M.-C. Hung, and H. Yamaguchi, *A perspective on anti-EGFR therapies targeting triple-negative breast cancer.* American journal of cancer research, 2016. **6**(8): p. 1609.

124. Hahn, M.A., et al., *Nanoparticles as contrast agents for in-vivo bioimaging: current status and future perspectives.* Analytical and bioanalytical chemistry, 2011. **399**(1): p. 3-27.

125. Zhang, M., et al., *Ultrasound-guided photoacoustic imaging for the selective detection of EGFR-expressing breast cancer and lymph node metastases.* Biomedical optics express, 2016. **7**(5): p. 1920-1931.

126. Bharathiraja, S., et al., *Cytotoxic Induction and Photoacoustic Imaging of Breast Cancer Cells Using Astaxanthin-Reduced Gold Nanoparticles.* Nanomaterials, 2016. **6**(4): p. 78.

127. Kennedy, L.C., et al., *A New Era for Cancer Treatment: Gold‐Nanoparticle‐Mediated Thermal Therapies.* Small, 2011. **7**(2): p. 169-183.

128. Bayer, C.L., et al., *Multiplex photoacoustic molecular imaging using targeted silica-coated gold nanorods.* Biomedical optics express, 2011. **2**(7): p. 1828-1835.

129. Kanazaki, K., et al., *Development of anti-HER2 fragment antibody conjugated to iron oxide nanoparticles for in vivo HER2-targeted photoacoustic tumor imaging.* Nanomedicine: Nanotechnology, Biology and Medicine, 2015. **11**(8): p. 2051-2060.
130. Homan, K., et al., *Silver nanosystems for photoacoustic imaging and image-guided therapy.* Journal of biomedical optics, 2010. **15**(2): p. 021316-021316-9.
131. Zhang, T., et al. *In vivo photoacoustic imaging of breast cancer tumor with HER2-targeted nanodiamonds*. in *Proceedings of SPIE--the International Society for Optical Engineering*. 2013. NIH Public Access.
132. Balasundaram, G., et al., *Molecular photoacoustic imaging of breast cancer using an actively targeted conjugated polymer.* International journal of nanomedicine, 2015. **10**: p. 387.
133. Pan, D., et al., *Photoacoustic sentinel lymph node imaging with self-assembled copper neodecanoate nanoparticles.* Acs Nano, 2012. **6**(2): p. 1260-1267.
134. Wang, B., et al., *Photoacoustic tomography and fluorescence molecular tomography: A comparative study based on indocyanine green.* Medical physics, 2012. **39**(5): p. 2512-2517.
135. Kim, G., et al., *Indocyanine-green-embedded PEBBLEs as a contrast agent for photoacoustic imaging.* Journal of biomedical optics, 2007. **12**(4): p. 044020-044020-8.
136. Ma, R., et al., *Estrogen Receptor β as a Therapeutic Target in Breast Cancer Stem Cells.* Journal Of The National Cancer Institute, 2017. **109**(3): p. djw236.
137. Erpelding, T.N., et al., *Sentinel lymph nodes in the rat: noninvasive photoacoustic and US imaging with a clinical US system.* Radiology, 2010. **256**(1): p. 102-110.
138. Hale, G.M. and M.R. Querry, *Optical constants of water in the 200-nm to 200-μm wavelength region.* Applied optics, 1973. **12**(3): p. 555-563.

139. Wang, L., S.L. Jacques, and L. Zheng, *MCML—Monte Carlo modeling of light transport in multi-layered tissues.* Computer methods and programs in biomedicine, 1995. **47**(2): p. 131-146.

140. Anderson, R.R. and J.A. Parrish, *The optics of human skin.* Journal of investigative dermatology, 1981. **77**(1): p. 13-19.

141. Van der Zee, P., *Measurement and modelling of the optical properties of human tissue in the near infrared.* 1992.

142. Marchesini, R., et al., *Extinction and absorption coefficients and scattering phase functions of human tissues in vitro.* Applied Optics, 1989. **28**(12): p. 2318-2324.

143. Van Veen, R., et al., *Determination of visible near-IR absorption coefficients of mammalian fat using time-and spatially resolved diffuse reflectance and transmission spectroscopy.* Journal of biomedical optics, 2005. **10**(5): p. 054004.

144. Bashkatov, A., et al., *Optical properties of human skin, subcutaneous and mucous tissues in the wavelength range from 400 to 2000 nm.* Journal of Physics D: Applied Physics, 2005. **38**(15): p. 2543.

145. Huibers, P.D., *Models for the wavelength dependence of the index of refraction of water.* Applied Optics, 1997. **36**(16): p. 3785-3787.

146. Index, R. *Refractive Index Database*. 2017, Septemper; Available from: https://refractiveindex.info/?shelf=glass&book=BK7&page=CDGM.

147. Duric, N., et al. *Ultrasound tomography for breast cancer screening (Conference Presentation)*. in *Medical Imaging 2018: Ultrasonic Imaging and Tomography*. 2018. International Society for Optics and Photonics.

ABSTRACT

DEVELOPMENT OF A NOVEL ULTRASOUND/PHOTOACOUSTIC TOMOGRAPHY SYSTEM FOR BREAST CANCER IMAGING USING FULL-RING ILLUMINATION MODE

by

SUHAIL SALEM ALSHAHRANI

December 2019

Advisor: Dr. Mohammad Mehrmohammadi

Major: Biomedical Engineering

Degree: Doctor of Philosophy

Breast cancer is a significant health problem, not only in the United States but globally. In the last year, breast cancer was the second leading cause of cancer deaths between women in the United States. In addition, the incidence rates of invasive and in situ female breast cancer increased in all age classes between 1975 and 2014. Early detection is a critical component in effectively managing this disease. One of the challenges of early detection of breast cancer lies in the availability and accuracy of diagnostic imaging. Several modalities for early detection are currently available and in use. One of the most widely used is the mammogram. However, this x-ray based diagnostic tool has several limitations, including low sensitivity to dense breast tissue, so there is a need for additional diagnostic tools, such as ultrasound (US) imaging or biopsies to complement the mammogram.

The photoacoustic (PA) imaging modality has proven to be a reliable imaging technique that shares acquisition tools with the US modality. When used together, these modalities can provide molecular- and cellular-particular imaging of tumors. In addition, ultrasound tomography

(UST) equipped with a ring US transducer has been shown in recent years to produce reliable results in imaging breast cancer. Significant advantages will be achieved by combining UST and PA tomography (PAT) into one complete and seamless US/PA tomography imaging modality, which will provide a valuable set of morphological and molecular data about the breast. However, the main challenge with any breast PAT lies in the accuracy of the acoustical receiver (transducer) and the effectiveness of the tissue (breast) illumination.

In this Ph.D. thesis, I will explore a novel, omnidirectional full-ring illumination method designed to illuminate a specific cross-sectional slice of breast tissue using a combination of a ring US transducer and PAT, which is referred to US/PA tomography. Preliminary results, created from multiple studies on different tissue-mimicking phantoms by utilizing full-ring illumination, have shown a significant penetration depth in a targeted cross-sectional area irrespective of vertical depth. In addition, the full-ring illumination has shown a uniform PA signal in the targeted cross-sectional slice.

AUTOBIOGRAPHICAL STATEMENT

Suhail Salem Alshahrani was born in Riyadh, Saudi Arabia in the year 1985. He completed his B.Sc in Biomedical Technology from King Saud University (Riyadh, Saudi Arabia) in 2008. Then he holds a MSc degree in Biomedical Engineering from Wayne State University in May 2014 (Detroit, MI, USA). His doctoral research was to develop a novel ultrasound/photoacoustic tomography system for breast cancer imaging using full-ring illumination mode. His doctoral work was presented in several conferences such as IEEE-IUS (2017 and 2018), SPIE Photonic West (2017), SPIE Medical Imaging (2018). He presents his work also in local scientific meetings at Wayne State University and Barbara Ann Karmanos Cancer Institute between 2015 and 2019. During his PhD studies, he authored two journal papers. In addition, Suhail has authored three conference proceedings papers.

After PhD, Suhail will go back to Saudi Arabia to start his job as an assistant professor in the College of Applied Medical Sciences (Department of Biomedical Technology) at King Saud University (Riyadh).

The permanent emails (ep7200@wayne.edu) & (suhalshahrani@ksu.edu.sa)
This dissertation was written by Suhail Salem Alshahrani